

**DOE/ER-0313/76
ORNL/TM-2024/3694**

**FUSION MATERIALS
SEMIANNUAL PROGRESS REPORT
FOR THE PERIOD ENDING**

June 30, 2024

**Prepared for
DOE Office of Fusion Energy Sciences
(AT 60 20 10 0)**

DATE PUBLISHED: November 2024

**Prepared by
OAK RIDGE NATIONAL LABORATORY
Oak Ridge, Tennessee 37831
Managed by
UT-Battelle, LLC
For the
U.S. DEPARTMENT OF ENERGY**

FOREWORD

This is the seventy-sixth in a series of semiannual technical progress reports on fusion materials science activity supported by the Fusion Energy Sciences Program of the U.S. Department of Energy. It covers the period ending June 30, 2024. This report focuses on research addressing the effects on materials properties and performance of exposure to the neutronic, thermal and chemical environments anticipated in the chambers of fusion experiments and energy systems. This research is a major element of the national effort to establish the materials knowledge base for an economically and environmentally attractive fusion energy source. Research activities on issues related to the interaction of materials with plasmas are reported separately.

The results reported are the products of a national effort involving a number of national laboratories and universities. A large fraction of this work, particularly in relation to fission reactor irradiations, is carried out collaboratively with partners in Japan, Russia, and the European Union. The purpose of this series of reports is to provide a working technical record for the use of program participants, and to provide a means of communicating the efforts of fusion materials scientists to the broader fusion community, both nationally and worldwide.

This report has been compiled by Stephanie Melton, Oak Ridge National Laboratory. Her efforts, and the efforts of the many persons who made technical contributions, are gratefully acknowledged.

John Echols
Research Division
Office of Fusion Energy Sciences

TABLE OF CONTENTS

1	FERRITIC/MARTENSITIC STEEL DEVELOPMENT	
1.1	PROPERTY EVALUATION OF NEWLY PROPOSED PWHT-FREE BAINITIC STEELS—Y. Yamamoto, T. Graening Seibert (Oak Ridge National Laboratory)	1
1.2	INVESTIGATION OF HIGH TEMPERATURE HE EMBRITTLEMENT (HTHE) EFFECTS IN Fe-9%Cr AND AUSTENITIC STAINLESS STEEL—Z. Qi, S. Zinkle (The University of Tennessee)	5
1.3	IRRADIATION EFFECT ON THE STABILITY OF MX PRECIPITATE IN FERRITIC MODEL ALLOYS—W. Zhong, Y. Yang (Oak Ridge National Laboratory), E. Proehl (University of Tennessee)	13
1.4	MICROSTRUCTURE EVOLUTION IN PROTON IRRADIATED ULTRA-HIGH PURITY Fe-Cr ALLOYS—S. Chen, S. Zinkle (The University of Tennessee)	15
1.5	MICROSTRUCTURE EVOLUTION IN BCC PURE Fe AT DIFFERENT TEMPERATURES AFTER ENERGETIC SELF-ION IRRADIATION—Y. Li, Z. Qi, S. Zinkle (University of Tennessee)	21
2	ODS AND NANOCOMPOSITED ALLOY DEVELOPMENT	
2.1	COLD SPRAY AND FRICTION STIR PROCESSING OF ODS ALLOYS ON A FERRITIC MARTENSITIC STEEL SUBSTRATE—D. Zhang, X. Wang, J. Darsell, K. Ross, L. Li, W. Setyawan (Pacific Northwest National Laboratory)	26
2.2	COST-EFFECTIVE THERMOMECHANICAL PROCESSING OF NANOSTRUC-TURED FERRITIC ALLOYS: MICROSTRUCTURE AND MECHANICAL PROPERTIES INVESTIGATION—Y. Lin, T.S. Byun (Oak Ridge National Laboratory)	35
3	CERAMIC COMPOSITE STRUCTURAL MATERIAL DEVELOPMENT	
3.1	EMERGING CONTINUOUS SiC FIBERS FOR HIGH-TEMPERATURE APPLICATIONS—H. Gietl (Idaho National Laboratory), O. Karakoc, S. Harrison (Free Form Fibers), T. Koyanagi, Y. Katoh (Oak Ridge National Laboratory)	37
4	PLASMA-FACING AND HIGH HEAT FLUX MATERIALS AND COMPONENT TESTING	
4.1	MICROSTRUCTURAL FEATURES IN DUCTILE-PHASE-TOUGHENED TUNGSTEN IRRADIATED INDIVIDUALLY WITH Ni²⁺ AND He⁺ IONS AT 1,000°C—W. Jiang, J. V. Haag IV, L. Kovarik, B. Matthews, W. Setyawan (Pacific Northwest National Laboratory), D. Chen (University of Houston)	38
4.2	SIMULTANEOUS EXPOSURE OF FUSION MATERIALS TO NEUTRON IRRADIATION AND HYDROGEN ENVIRONMENT—W. Zhong, T. Koyanagi, Y. Katoh (Oak Ridge National Laboratory), Y. Hatano (University of Toyama)	42

TABLE OF CONTENTS

4.3	ANNEALING AND ELEVATED TEMPERATURE TENSILE STUDIES ON W/NiFe DUCTILE-PHASE TOUGHENED W COMPOSITES —R. Prabhakaran, W. Setyawan (Pacific Northwest National Laboratory)	44
4.4	MECHANICAL RESPONSES OF TUNGSTEN IN A DUCTILE-PHASE-TOUGHENED TUNGSTEN HEAVY ALLOY TO ION IRRADIATION SIMULATING FUSION REACTOR ENVIRONMENTS —A. Garcia-Caraveo, S. Doran, T. Rohwer, T. Chen (Oregon State University), L. Shao (Texas A&M University), W. Jiang, J. V. Haag IV, R. Prabhakaran, W. Setyawan (Pacific Northwest National Laboratory)	58
4.5	SECONDARY ION MASS SPECTROMETRY ANALYSIS OF SINGLE CRYSTAL AND IRRADIATED TUNGSTEN SAMPLES —G. Parker (University of Illinois Chicago), T. Misicko (Louisiana Tech University), X-Y. Yu (Oak Ridge National Laboratory)	69
4.6	QUANTITATIVE ASSESSMENT OF Ni⁺ AND He⁺ ION IRRADIATION DAMAGE IN A TUNGSTEN HEAVY ALLOY UNDER THE SIMULATED NUCLEAR FUSION ENVIRONMENT —J. V. Haag IV, B. Matthews, M. Olszta, W. Jiang, D. Edwards, Y. Fu, W. Setyawan (Pacific Northwest National Laboratory)	72
4.7	FLASH POLISHING TECHNIQUES ON TUNGSTEN FOR TRANSMISSION ELECTRON MICROSCOPY OBSERVATION —W. Zhong, Y. Lin, S. Calzada (Oak Ridge National Laboratory)	75
5.0	HYDROGEN AND HELIUM EFFECTS <i>No contributions this reporting period.</i>	
6.0	FUSION CORROSION AND COMPATIBILITY SCIENCE	
6.1	COMPATIBILITY of WELDED CNA in EUTECTIC PbLi and DEVELOPMENT SLURRY ALUMINIDE COATINGS on FERRITIC and AUSTENITIC STEELS —M. Romedenne, C. De Lamater-Brotherton, W. Tang, B. Armstrong, Y. Zhang, B. Pint (Oak Ridge National Laboratory)	77
7.0	ADVANCED MANUFACTURING <i>No contributions this reporting period.</i>	
8.0	MECHANISMS AND ANALYSIS	
8.1	DETERMINATION OF FLUORINE DISTRIBUTION IN CrFe ALLOY —G. Parker (University of Illinois Chicago), Y. Li, S. Zinkle (University of Tennessee), Oak Ridge National Laboratory), X-Y. Yu (Oak Ridge National Laboratory)	83
8.2	THE ROLE OF STACKING FAULT TETRAHEDRA ON VOID SWELLING IN IRRADIATED COPPER —Y. Lin, M. Zachman, (Oak Ridge National Laboratory), S. Zinkle, Z. Yu, H. Xu (University of Tennessee)	86

TABLE OF CONTENTS

9.0	MODELING AND COMPUTATIONAL STUDIES	
9.1	MECHANISMS OF MOBILITY OF GRAIN BOUNDARIES IN TUNGSTEN —R. Moore (Lehigh University), T. Frolov, R. Rudd (Lawrence Livermore National Laboratory)	88
9.2	PROGRESS IN PREDICTIVE MODELING OF HE BUBBLE ACCUMULATION IN NANOSTRUCTURED FERRITIC ALLOYS —K. Pitike, J. Spencer, W. Setyawan (Pacific Northwest National Laboratory)	94
9.3	FIRST PRINCIPLES STUDY OF BULK AND RADIATION INDUCED DEFECTS PROPERTIES OF TiB₂ —Y. Osetskiy, G. Samolyuk (Oak Ridge National Laboratory)	101
9.4	PROGRESS IN PREDICTIVE MODELING OF HE BUBBLE ACCUMULATION IN NANOSTRUCTURED FERRITIC ALLOYS —K. Pitike, J. Spencer, W. Setyawan (Pacific Northwest National Laboratory)	105
10	FUSION SYSTEM DESIGN	
	<i>No contributions this reporting period.</i>	
11	IRRADIATION & TESTING METHODS, EXPERIMENTS AND SCHEDULES	
11.1	SPECIMEN SIZE AND GEOMETRY EFFECTS ON THE MASTER CURVE FRACTURE TOUGHNESS MEASUREMENT OF EUROFER97 AND F82H STEELS —X. Chen, M. Sokolov, Y. Katoh (Oak Ridge National Laboratory), John Echols (U.S. Department of Energy)	112
11.2	IRRADIATION OF JK2LB ALLOYS FOR ADDITIVE MANUFACTURING OF FUSION COMPONENTS FOR THE INFUSE PROJECT WITH TYPE ONE ENERGY —N. Russell, X. Chen, W. Zhong, Y. Yang (Oak Ridge National Laboratory), B. Goh (Type One Energy), L. Chen (University of Wisconsin, Madison)	115

1. FERRITIC/MARTENSITIC STEEL DEVELOPMENT

1.1 PROPERTY EVALUATION OF NEWLY PROPOSED PWHT-FREE BAINITIC STEELS—Y. Yamamoto, T. Graening Seibert (Oak Ridge National Laboratory)

OBJECTIVE

This work aims to evaluate the advantages in the mechanical performance of newly proposed, modified 3Cr-3WVTa bainitic steels developed at Oak Ridge National Laboratory. The proposed steel was designed to eliminate the need for post-weld heat treatment (PWHT), as well as providing improved mechanical properties of both base metal and weldments compared to those of existing commercial bainitic steels or ferritic-martensitic (F-M) steels. The target applications are high-temperature structural components in fusion reactors, such as helium-cooled vacuum vessels operating up to 450°C and blanket support structures operating up to 550°C. The first-generation steel containing an increased Mn and reduced C contents showed significant improvement in high-temperature mechanical properties but suffered from embrittlement after thermal exposure, which could be exacerbated by irradiation embrittlement. The present target is to seek new composition ranges of the steels with the same PWHT-free design concept without embrittlement after a thermal treatment at operating temperature or irradiation.

SUMMARY

A new alloy modification of the reduced-activation bainitic ferritic steel was proposed with PWHT-free design. The target is to avoid the significant drop of the impact toughness observed in the previously proposed MLC02T steel after a short-term thermal exposure at 500°C. A new series of alloy compositions with 5 wt.% of Cr, instead of the increased Mn addition in the MLC02T, were selected with expectation of improved hardenability by stabilizing austenite phase at elevated temperature. The alloy also incorporated the lowered C content to maintain relatively low hardness in the as-welded or as-normalized conditions, together with a small addition of Ni instead of Mn to compensate the loss of the hardenability in the steel. The alloy with 5Cr-0.014C-0.9Ni (5Cr-LCN2) successfully met with the proposed PWHT-free alloy design with respect to the microstructure control (fully bainitic ferritic structure), hardness response, and a significant reduction of the embrittlement issue by minimizing the Mn addition. Unintentional low carbon content in the 5Cr-LCN2 than the target (0.014 vs. 0.03 wt.%) might lead to relatively low high-temperature tensile strengths in the present study, suggesting that a precise control of the alloy composition would be the key to enable steels with balanced properties.

PROGRESS AND STATUS

A compositionally modified 3Cr-3WVTa bainitic ferritic steel (Mod. 3Cr-3WVTa steel, ID: MLC02T) was proposed with an advanced alloy design to achieve a reduced property inhomogeneity across the weldment in as-welded condition, targeting a PWHT-free bainitic ferritic steel for fusion structural applications. The design strategy included to maintain or improve the hardenability of the steel and lower the hardness in the as-normalized or as-welded condition. The target characteristics was achieved by the increased addition of manganese together with the lowered carbon content. The modified steel, MLC02T, also revealed the improved high-temperature creep properties in the base metal and the cross-weld specimens and lower the ductile-brittle transition temperature in the as-normalized and as-welded condition than those of the original 3Cr-3WVTa steel. The experimental results suggested that the modified steel met with the expected characteristics for PWHT-free design. However, it was also found that a short-term exposure at the potential service temperature (for 1,000 h at 500°C) of the modified steel resulted in a significant drop of the impact toughness, which could be attributed to high Mn content of the steel similar to the irradiation embrittlement promoted by manganese.

Based on the background described above, a new alloy modification of the 3Cr-3WVTa bainitic steel with the same PWHT-free design concept was proposed with no intentional addition of Mn. Since the Cr addition up to 7 wt.% is also known to increase the stability of austenite phase at elevated temperature and retard the ferrite transformation, the addition of 5 wt.% of Cr, instead of the increased Mn addition, was selected with expectation of improved hardenability. However, the steel with a solo Cr addition to the original steel

(ID: 5Cr) showed formation of ferrite grains inside the bainite ferrite matrix, suggesting that the increased Cr addition was not enough to improve the austenite phase stability as expected, resulting in a failure to suppress the ferrite formation. On the other hand, the 5Cr steel with a lowered C content combining with a small addition of Ni (ID: 5Cr-LCN2) resulted in forming a full bainitic microstructure after normalization. Despite a full bainitic microstructure, the hardness of the as-normalized 5Cr-LCN2 (272 ± 7 HV) was significantly lower than that of the 5Cr steel (367 ± 6 HV), which also met with the expectation from the PWHT-free design. Therefore, the 5Cr-LCN2 was selected for further property evaluation and compared with those of the original, MLC02T, and 5Cr steels. Table 1 summarizes the nominal and analyzed compositions of the materials evaluated in the present study.

Table 1. Nominal and analyzed compositions of bainitic steels studied (balanced Fe)

Name	Alloy composition, wt.%									Remarks
	Fe	Cr	W	V	Si	Mn	Ta	C	Ni	
Original	Nominal	Bal.	3	3	0.2	0.16	0.4	0.1	0.1	Requires PWHT, proposed in 1990's [ref.]
	Analyzed	Bal.	3.0	3.0	0.20	0.14	0.40	0.10	0.10	
MLC02T	Nominal	Bal.	3	3	0.2	0.16	2	0.1	0.03	Modified 3Cr-3WVTa, PWHT-free design
	Analyzed	Bal.	3.0	3.0	0.20	0.14	2.0	0.08	0.04	
5Cr	Nominal	Bal.	5	3	0.2	0.16	0.2	0.1	0.1	Based on original with additional Cr
	Analyzed	Bal.	5.0	3.0	0.21	0.17	0.20	0.11	0.083	
5Cr-LCN2	Nominal	Bal.	5	3	0.2	0.16	0.2	0.1	0.03	Low carbon with 1 wt.% Ni addition
	Analyzed	Bal.	5.1	2.9	0.20	0.11	0.20	0.11	0.014	

[ref.] R.L. Klueh et al., Int. J. Pressure Vessels and Piping, 84 (2007) 29-36.

Figure 1 represents the Vickers hardness (1a) and Charpy impact absorbed energy (1b) at room temperature of four different steels in Table 1, comparing those properties in the as-normalized condition (at 1,100 or 1,000°C for 30min, followed by air-cooling) and the normalized-and-tempered condition (+ 700°C for 1h, followed by air-cooling). The hardness of the “5Cr” steel dropped significantly after tempering, whereas that of the 5Cr-LCN2 steel did not change much, which was similar to the responses of the 3Cr-containing steels after tempering. This was one of the expected characteristics of PWHT-free design in which the hardness variation is sufficiently small between the welded (similar to an as-normalized condition) and the heat affected zone (similar to a tempered condition) regions. The changes in the Charpy impact absorbed energy of the 5Cr-containing steels before and after tempering also showed a trend similar to those of the 3Cr-containing steels. The as-normalized absorbed energy of the 5Cr-LCN2 steel was higher than that of the 5Cr steel, which was attributed to lower carbon content in the 5Cr-LCN2 than the 5Cr. After tempering, the absorbed energy of the 5Cr-LCN2 decreased as opposed to the response in the 5Cr, although the reduction of the absorbed energy was not so significant like those in the MLC02T. These results suggest that the alloy modification in the 5Cr-LCN2 with low C + 1 wt.% Ni addition could successfully meet with the proposed PWHT-free alloy design with respect to the microstructure control (fully bainitic ferritic structure, as previously reported), hardness response, and a significant reduction of the embrittlement issue by minimizing the Mn addition. The absolute hardness in the 5Cr-LCN2 before and after tempering was lower than those of the MLC02T, which could be due to lower C content (0.014 wt.%) in the 5Cr-LCN2 than MLC02T (0.04 wt.%). The lower C content in the 5Cr-LCN2 than the target (nominally 0.03 wt.%) was unintentional, so that another set of the ingot preparation with variation of C contents is currently in progress to evaluate the effect of the C content on the properties of the 5Cr-LCN type steels.

Temperature dependence of the tensile properties in the proposed steels were evaluated, as shown in Figure 2. They were evaluated in the as-normalized conditions (at 1100°C for the original steel, and at 1000°C for the other steels) tested at RT, 500 through 600°C, and then compared with those of Grade 91 steel from NIMS creep data sheet (<https://doi.org/10.1080/14686996.2019.1697616>). Comparing with the original, the 5Cr resulted in a significant drop of high-temperature tensile strengths, which was due to weak ferrite formation inside bainitic microstructure. The 5Cr-LCN2 also showed similar HT strengths to the 5Cr, although the low strength was not directly from the ferrite observed in the starting microstructure but

extremely low carbon content (0.014 wt.%) in the steel. The results also suggested a requirement of the C content optimization.

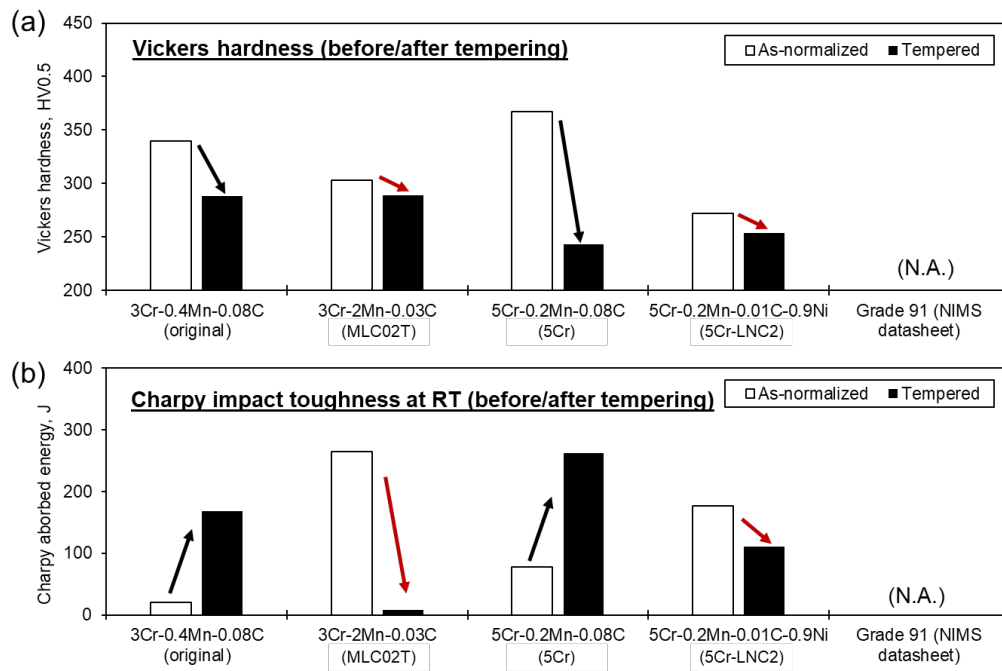


Figure 1. Comparison of micro-Vickers hardness (a) and Charpy impact absorbed energy (b) of the bainitic steels before and after tempering, tested at room temperature.

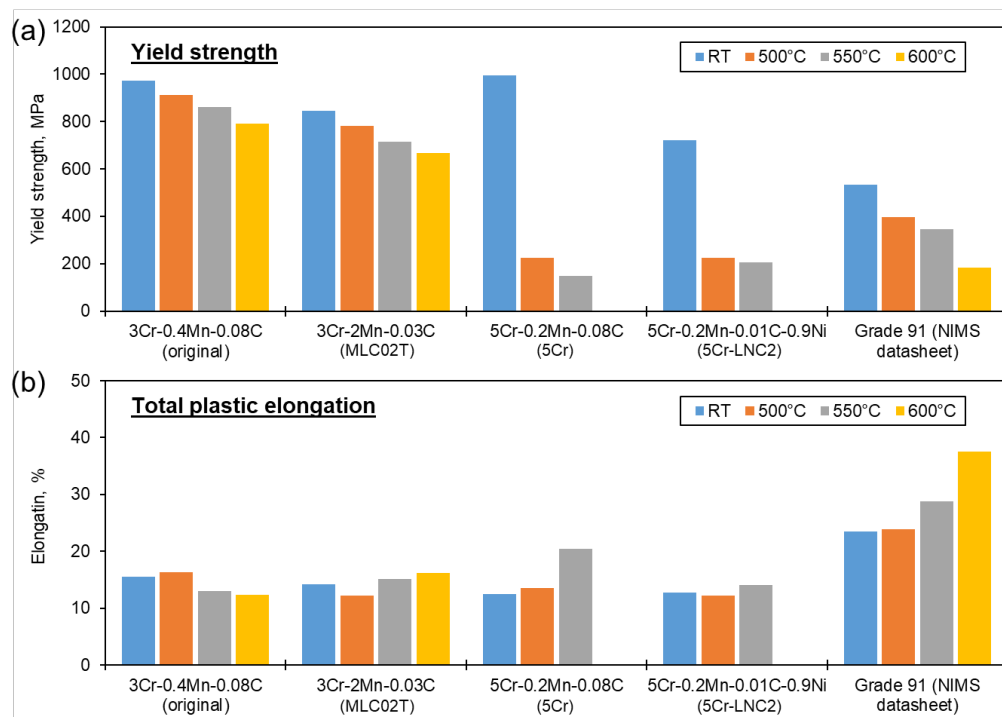


Figure 2. Tensile properties of a series of bainitic steels evaluated in the present study, together with those of Gr. 91 steel: (a) yield strength, and (b) total plastic elongation.

Based on the present test results, it is concluded that the alloy modification of “Mn-free” 3Cr-3WVTa steel with “only” the increased Cr addition would not reproduce the microstructural characteristics or the hardness observed in the MLC02T. The addition of Ni instead of Mn compensates the loss of the hardenability for the “Mn-free + low C” alloy design. More Ni addition could promote further hardenability improvement, although it would be prohibitive due to the tradeoff of irradiation penalty from high Ni contents. The newly proposed 5Cr-LCN2 steel met with the expected PWHT-free design including a formation of full bainitic structure and no significant hardness drop after tempering. However, the observed hardness and the high-temperature tensile strengths were lower than those of the MLC02T steel, possibly due to the lower carbon content than the target (0.014 vs. 0.03 wt.%). Another set of the ingot preparation with variation of C contents is currently in progress to evaluate the effect of the C content on the properties of the 5Cr-LCN type steels.

Results

The alloys with 5 wt.% Cr, low C, combining with the Ni addition are selected to be the basis for next-generation PWHT-free reduced-activation bainitic ferritic steels. Further compositional tuning with the property screening will be continued to narrow down the composition range which can satisfy the PWHT-free design and exhibit the mechanical properties similar to the high Mn containing MLC02T steel.

1.2 INVESTIGATION OF HIGH TEMPERATURE HE EMBRITTLEMENT (HTHE) EFFECTS IN Fe-9%Cr AND AUSTENITIC STAINLESS STEEL—Z. Qi, S. Zinkle (The University of Tennessee)

OBJECTIVE

The objective of this project is to study how tensile stress, dislocation line density and crystal structure affect high temperature helium embrittlement (HTHE) behavior by characterizing cavity size and number density in the matrix and at grain boundaries (GBs) in 316L stainless steel (SS) and Fe-9%Cr after different He implantation conditions.

SUMMARY

A 316L SS and Fe-9%Cr were pre-deformed to introduce additional dislocation lines. Transmission Electron Microscopy/Scanning transmission electron microscopy (TEM/STEM) images were obtained to characterize cavity size and density in the matrix and at GBs as well as dislocation line density after 4.5 MeV He²⁺ irradiations to 1800 appm peak implanted He concentrations at 750°C with and without stress in 316L SS, 316L SS (pre-deformed), Fe-9%Cr and Fe-9%Cr (pre-deformed). The combined presence of higher initial dislocation line density and elastic stress during He implantation led to enhanced growth of matrix cavities and the enhanced nucleation of matrix and GB cavities, which might be due to enhanced diffusivity of He-vacancy clusters in the presence of dislocations and stress. A large void was observed at a GB for pre-deformed Fe-9%Cr after irradiation, indicating less HTHE resistance for Fe-9%Cr than 316L SS, possibly due to the higher diffusivity in BCC materials than in FCC materials.

PROGRESS AND STATUS

An innovative specimen fixture was designed to passively provide tensile stress from zero to ~200 MPa during 4.5 MeV He irradiations at 750°C. Detailed information on the specimen fixture is given in [1]. The four He implantation conditions examined in the most recent portion of our investigations are shown in Table 1. The dose and He concentration profile calculated by SRIM full cascades (damage energy method) are shown in Figure 1. The detailed information about 316L SS and Fe-9%Cr used is shown in Table 2.

Table 1. Irradiation matrix of the alloys

	Materials	Ion Species	Initial stress (MPa)	Fluence (ions/cm ²)	Flux (ions/cm ² s)	Temp. (°C)
#4	Fe-9%Cr, and 316L SS	4.5 MeV He	0	6.12x10 ¹⁵ (1800 appm)	9.44x10 ¹⁰ (100 appm/h)	750
#5			100			
#6	Fe-9%Cr (pre-deformed), and 316L SS		> 0			
#7	Fe-9%Cr (pre-deformed), and 316L SS (pre-deformed)		>100			

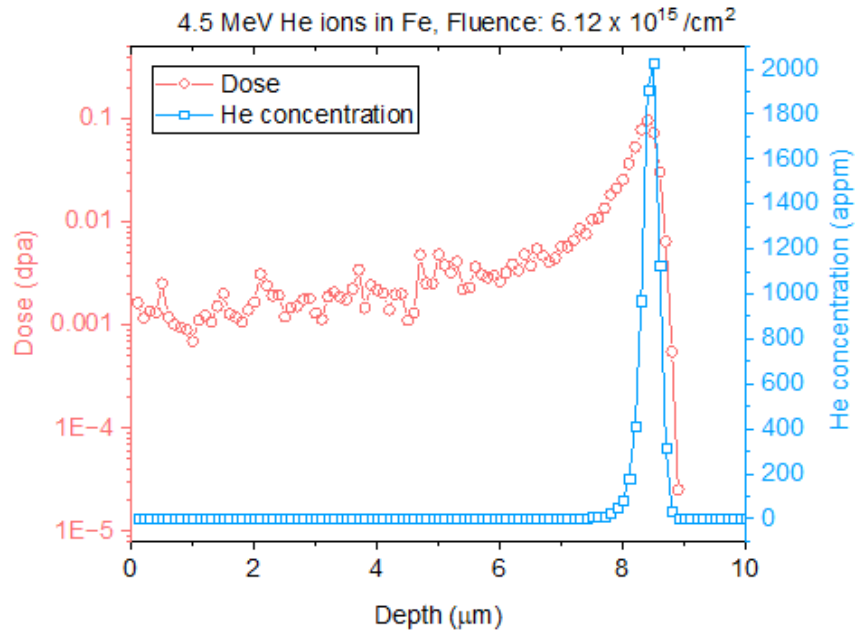


Figure 1. Dose and He concentration profile calculated by Stopping and Range of Ions in Matter (SRIM) for 4.5 MeV He ions in Fe with the fluence of $6.12 \times 10^{15} / \text{cm}^2$.

Table 2. Detailed information about the alloys

Material	Crystal structure	Grain size (μm)	Main chemical composition	Matrix			GB ppts
				Dislocations	Precipitates	Sink strength	
316L SS	FCC	~40	Fe-17% Cr, 10% Ni, 2% Mo	Low density ($\sim 1 \times 10^9 / \text{cm}^2$)	Low density ppts ($\sim 2 \times 10^{13} / \text{cm}^3$, ~ 60 nm)	$\sim 2 \times 10^{13} / \text{m}^2$	/
Fe-9%Cr	BCC	~40	Fe-9% Cr, 0.1% Mn	Low density ($\sim 2 \times 10^9 / \text{cm}^2$)	Low density ppts ($\sim 4 \times 10^{13} / \text{cm}^3$, ~ 40 nm)	$\sim 3 \times 10^{13} / \text{m}^2$	/

The initial stress of 100 MPa in irradiation #5 was applied on a curved plate with $R_0 \sim 400$ mm. For irradiations #6 and #7, two 316LSS were pre-deformed concavely on a surface with a radius of curvature $R_1 \sim 20$ mm, leading to a surface strain of $\sim 1.4\%$. Two Fe-9%Cr samples were pre-deformed concavely on a surface with a radius of curvature $R_2 \sim 34$ mm, leading to a surface strain of $\sim 0.8\%$. After that, all four samples were deformed back convexly on a surface with a radius of curvature $R_0 \sim 400$ mm. The curvatures of the sample surfaces due to residual stresses were observed by SEM and the dislocation line densities were measured by STEM before irradiation, as shown in Table 3. One 316LSS and one Fe-9%Cr were irradiated without applied stress, and the other two samples were irradiated with applied stress on a curved plate with $R_0 \sim 400$ mm. According to the curvature of the sample surfaces of ~ 200 mm and the curvature of the curved plate, the initial stresses of these two samples were $\Delta\sigma > E \left(\frac{t}{2R_{400}} + \frac{t}{2R_{200}} \right) \sim 300$ MPa at room temperature, where t is the sample thickness. However, the yield stresses of 316LSS and Fe-9%Cr are both ~ 120 MPa at 750°C . Therefore, additional dislocation lines were created by this pre-irradiation deformation, and the initial stresses were relaxed to ~ 120 MPa when the samples were heated to 750°C before irradiation, which

explains the higher dislocation densities after irradiation #7. Since the irradiation conditions of #6 and #7 are almost the same as #4 and #5, direct comparisons can be made.

Table 3. Surface curvature and dislocation line density of samples

Material	Irradiation condition	Surface curvature - pristine R/mm	Dislocation line density - pristine (cm^{-2})	Dislocation line density - irradiated (cm^{-2})
316LSS	#4	-	1.2×10^9	6×10^7
	#5	-	1.2×10^9	1×10^8
	#6	190	3.3×10^9	1.1×10^9
	#7	150	1.4×10^9	5.6×10^9
Fe-9%Cr	#4	-	2×10^9	2.2×10^9
	#5	-	2×10^9	1.8×10^9
	#6	140	9.2×10^9	1.7×10^9
	#7	170	3.4×10^9	4.4×10^9

During He implantation, stress relaxation from thermal creep ($\dot{\epsilon}_{th}$) and irradiation creep ($\dot{\epsilon}_{irr}$) can take place: $\frac{d\sigma}{dt} = -E(\dot{\epsilon}_{irr} + \dot{\epsilon}_{th})$, where E is the elastic modulus. Since irradiation creep is negligible compared to thermal creep, Figure 2 can represent the stress relaxation process for irradiations #4 - #7 despite different dose rates for different irradiation conditions. The initial 100 MPa tensile stress is predicted to relax to ~ 49 MPa for irradiations #4 - #7 over the course of the implantations. The average stresses were calculated to be 59 MPa for irradiations #4 - #7.

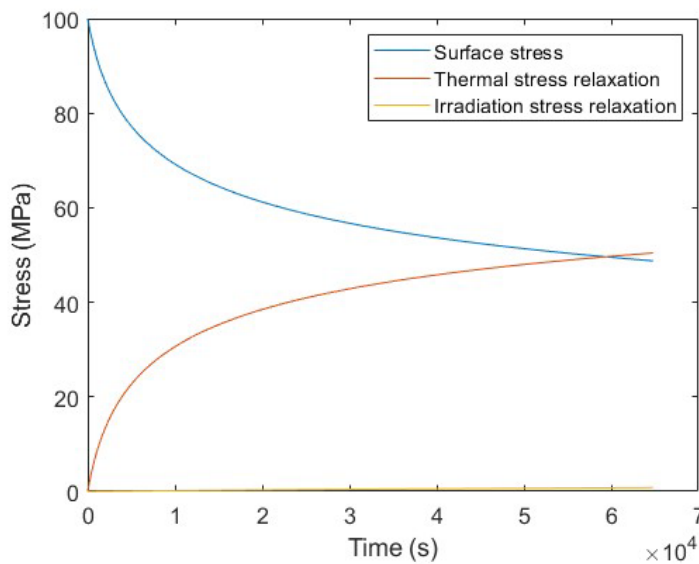


Figure 2. Residual surface stress and stress relaxation by thermal and irradiation creep versus time at 750°C.

The TEM images for cavities in the matrix and at grain boundaries in 316L SS and Fe-9%Cr in the He-implanted region for four different He implantation conditions are shown in Figure 3. Most matrix cavities were observed to be located at matrix-defect interfaces, such as at dislocation lines and precipitates. The corresponding average cavity size and number density values are shown in Figure 4 and Figure 5. Also, the calculated matrix cavity volume percent (fraction of matrix volume occupied by cavities) and GB cavity area percent (fraction of GB area occupied by cavities) are shown in Figure 6.

For 316LSS, the sample after irradiation #7 has ~2 times higher cavity number densities both in the matrix and at GBs than irradiations #4-#6. The samples after irradiations #6 and #7 have larger matrix cavity sizes; the average matrix cavity size is ~2 times larger after irradiation #6 and ~1.5 times larger after irradiation #7 compared to irradiations #4-#5. The average GB cavity sizes are comparable among irradiations #4-#6, with slightly smaller GB cavities (~25%) for irradiation #7. The calculated matrix cavity volume percent is ~3 times larger after irradiation #6 and ~5 times larger after irradiation #7 than irradiations #4-#5. However, the GB cavity area percent values exhibit almost no change among irradiations #4-#7, where the value for irradiation #7 is slightly higher (~20%). Therefore, the significant combined effect of higher dislocation line density and stress for 316L SS is the enhanced growth of matrix cavities, which might be due to the enhanced diffusivity of He-vacancy clusters. When the dislocation line density and stress are large enough (#7), there should be enhanced nucleation of matrix cavities due to increased defect sink strength, and enhanced nucleation of GB cavities due to enhanced diffusion of He-vacancy clusters from matrix to GB. Note that the dislocation line densities were different in pre-deformed 316L SS samples #6 and #7 and there was residual stress in sample #6. Therefore, it is not possible to separate the effect of dislocation line density and stress, which is also the case for Fe-9%Cr.

For Fe-9%Cr, no obvious change was observed for matrix cavity number densities among irradiations #4-#7, while at GBs there was a slight increase in #6-#7 compared to #4-#5. The samples after irradiations #6 and #7 have ~2 times larger average cavity sizes both in the matrix and at GBs than irradiations #4-#5, especially at GBs where a very large cavity with diameter >170nm was observed for irradiations #6-#7. The calculated matrix cavity volume percent and GB cavity area percent are ~4-5 times larger after irradiations #6-#7 than irradiations #4-#5, where the very large cavity at GB contributes ~50% of the GB cavity area percent for irradiations #6-#7. Therefore, the combined effect of higher dislocation line density and stress for Fe-9%Cr is slightly enhanced growth of matrix cavities and GB cavities, and enhanced nucleation of GB cavities, which might be due to enhanced diffusivity of He-vacancy clusters. Note that the GB cavity density values for #6 and #7 did not count the large void at the He implantation peak position since the large void occupied ~300 nm of the GB length and would greatly reduce the density values if counted. Since the cavity density at the He implantation peak position should be the largest when nucleated, we expect the nucleated GB density to be larger before cavity coalescence occurred by the void. There was no enhanced nucleation of matrix cavities in Fe-9%Cr, which might be because the dislocation line density was not increased enough by pre-bending. In Table 3, for 316L SS the dislocation line density after irradiation #7 was ~50 times larger than irradiations #4-#5 and ~5 times larger than irradiation #6, while for Fe-9%Cr the dislocation line density after irradiation #7 was only ~2 times larger than irradiations #4-#6.

Comparing 316L SS and Fe-9%Cr after irradiations #6-#7, 316L SS seems to be more resistant to HTHE effect than Fe-9%Cr for the examined test conditions, while an opposite conclusion would be obtained if only comparing the results of #4-#5. When there were no additional He-vacancy clusters diffusing from matrix to GBs in #4-#5, Fe-9%Cr seems to be more resistant to HTHE due to its higher density and lower size of matrix and GB cavities. However, when there were ~20% more He-vacancy clusters diffusing from matrix to GB due to the combined effect of higher dislocation line density and stress after irradiation #7 for 316L SS, it nucleated ~2 times higher GB cavity density. The higher GB density can partition the He-vacancy clusters diffusing from the matrix, resulting in a slightly lower GB cavity size for irradiation #7. In contrast, for Fe-9%Cr, when there were additional He-vacancy clusters diffusing from matrix to GBs in #6-#7 due to the combined effect of higher dislocation line density and stress, a large void was created at GB. This might be due to the higher diffusivity of dislocation lines under stress in BCC Fe-9%Cr that enables higher cooperative diffusion of He-vacancy clusters to GB by dislocation lines. In Table 3, the dislocation line density values between Fe-9%Cr and 316L SS are comparable after irradiation #6 or #7, while the dislocation line density is ~2-3 times larger in Fe-9%Cr than in 316L SS before the irradiations. Therefore, the higher diffusivity in BCC materials than in FCC materials is an adverse factor for HTHE resistance under creep conditions where significant network dislocations would be created.

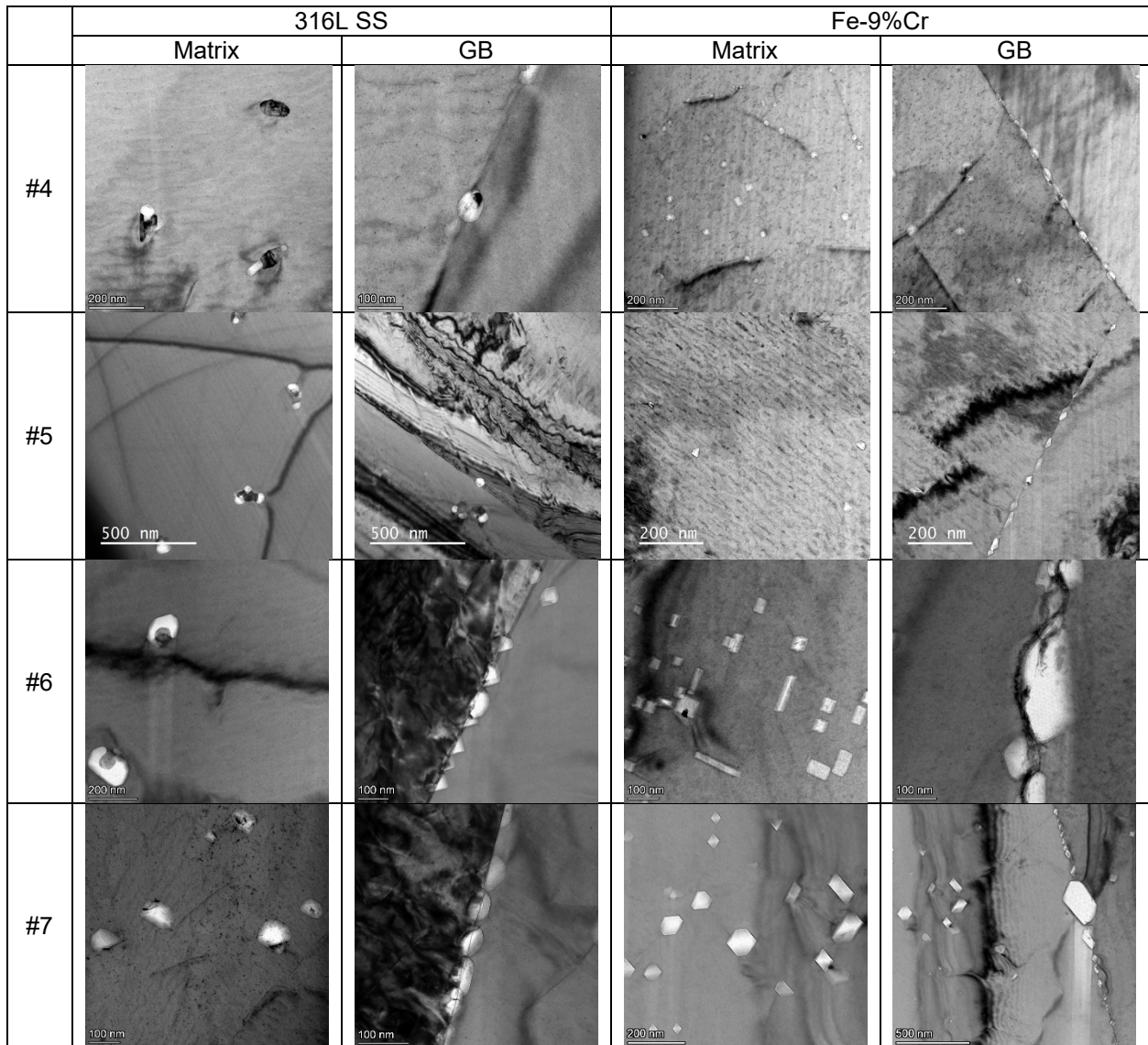


Figure 3. The TEM images of cavities in the matrix and at GB in 316L SS and Fe-9%Cr for four different implantation conditions.

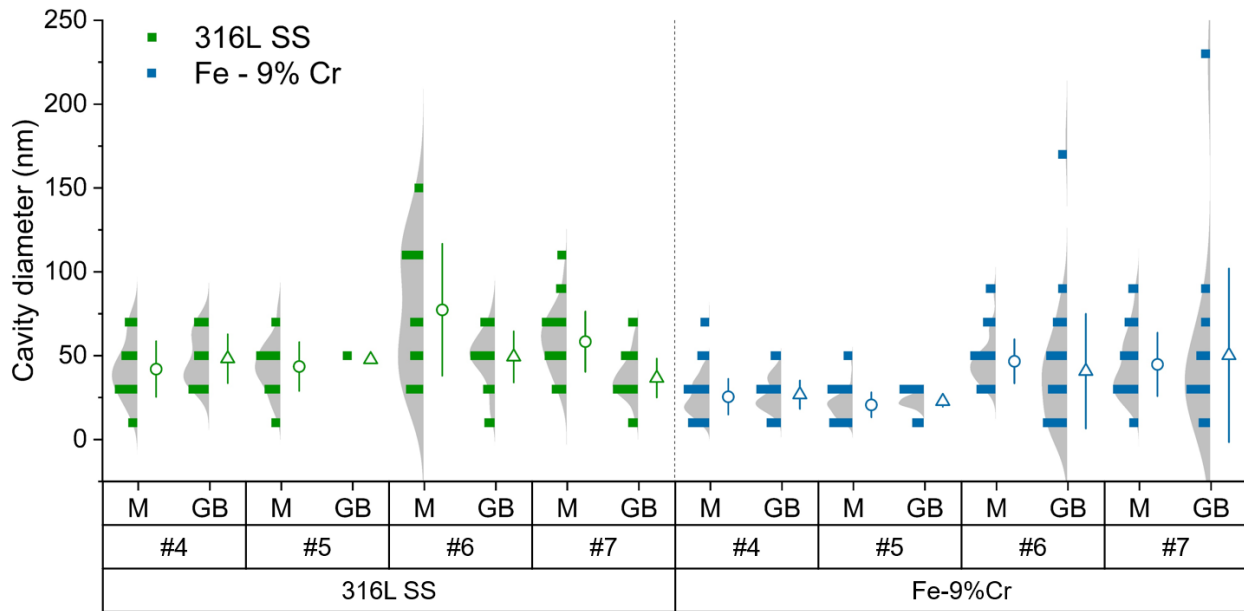


Figure 4. Matrix and GB cavity sizes for 316LSS and Fe-9%Cr after irradiations #4-#7.

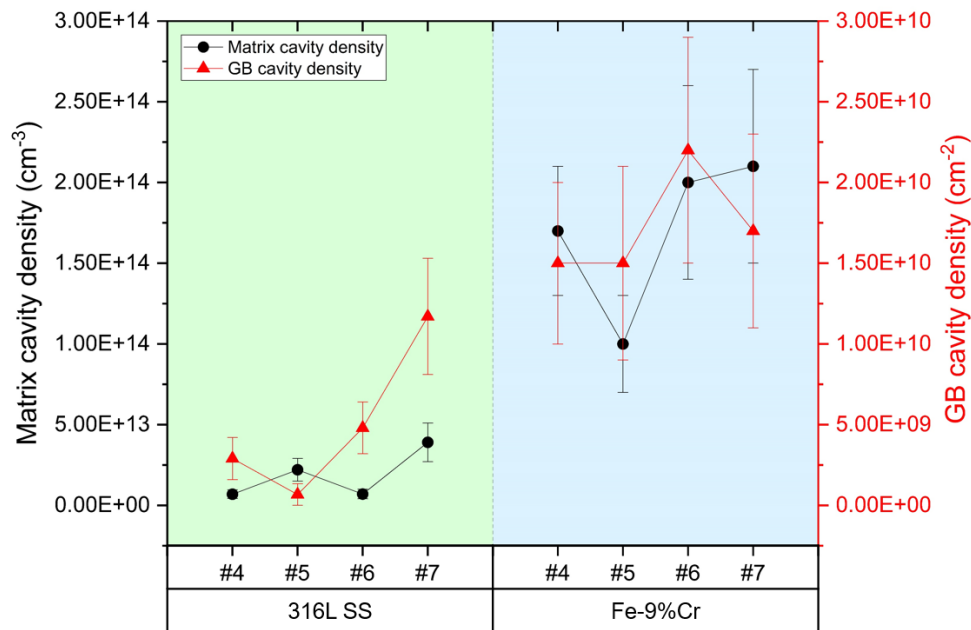


Figure 5. Matrix and GB cavity number densities for 316LSS and Fe-9%Cr after irradiations #4-#7.

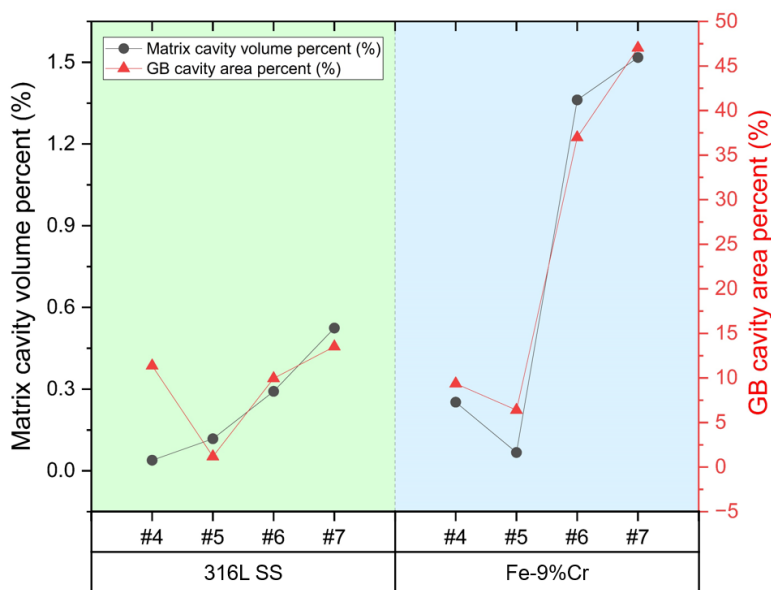


Figure 6. Matrix cavity volume percent and GB cavity area percent for 316LSS and Fe-9%Cr after irradiations #4-#7.

In Figure 7, the average size and number density of matrix cavities in 316L SS and Fe-9%Cr at 750°C are plotted along with the calculated equilibrium cavity curves for 0 and 49 MPa stresses by using 900 appm average He concentration. The calculated equilibrium cavity curves for 0 and 49 MPa stresses by using 50 appm average He concentration are also plotted in Figure 7 for reference. For this calculation, the Mills–Liebenberg–Bronson (MLB) equation [2] was used as the equation of state for He, and 1J/m² surface energy was assumed for both materials. Except for the cavity data for Fe-9%Cr after irradiations #6 and #7, all the other experimental data are below the equilibrium cavity curves of 900 appm, indicating that not all implanted He atoms were contained in the matrix cavities (the He concentrations contained in matrix cavities are about 50-150 appm). There could be He atoms diffusing to GB and surface sinks or diffusing to deeper depths due to the He concentration gradient at the high temperature of 750°C as some visible small cavities (~2 nm) were observed at depths < ~ 4 μm and at depths > ~12 μm. For Fe-9%Cr after irradiations #6 and #7, the data are almost at the equilibrium cavity curves of 900 appm, revealing that the matrix cavities contained a higher fraction of the implanted He atoms (~500 appm) than other samples, which might be due to higher dislocation line density with stress. However, although a higher fraction of the implanted He was retained in the matrix for Fe-9%Cr for irradiations #6 and #7, a large cavity still formed at a GB. This might be due to the higher diffusivity of He-vacancy clusters in the presence of dislocation lines (pipe diffusion or another mechanism) that carried more He-vacancy clusters to GB.

According to the calculation based on the MLB equation of state or the simplified equation based on ideal gas law for the critical cavity size: $r^* = \frac{4\gamma}{3\sigma}$, the calculated critical matrix cavity diameter $2r_m^*$ is ~160nm for irradiation #5 and #7. For GB cavities, using a GB inclination angle of ~45°, the critical GB cavity diameter $2r_{gb}^*$ is ~80nm for irradiation #5 and #7. For Fe-9%Cr after irradiation #7, the largest GB cavity size is much larger than the critical value and therefore can be considered as a void. A similar large void also existed in Fe-9%Cr after irradiation #6, which might be because large residual stress existed in the sample.

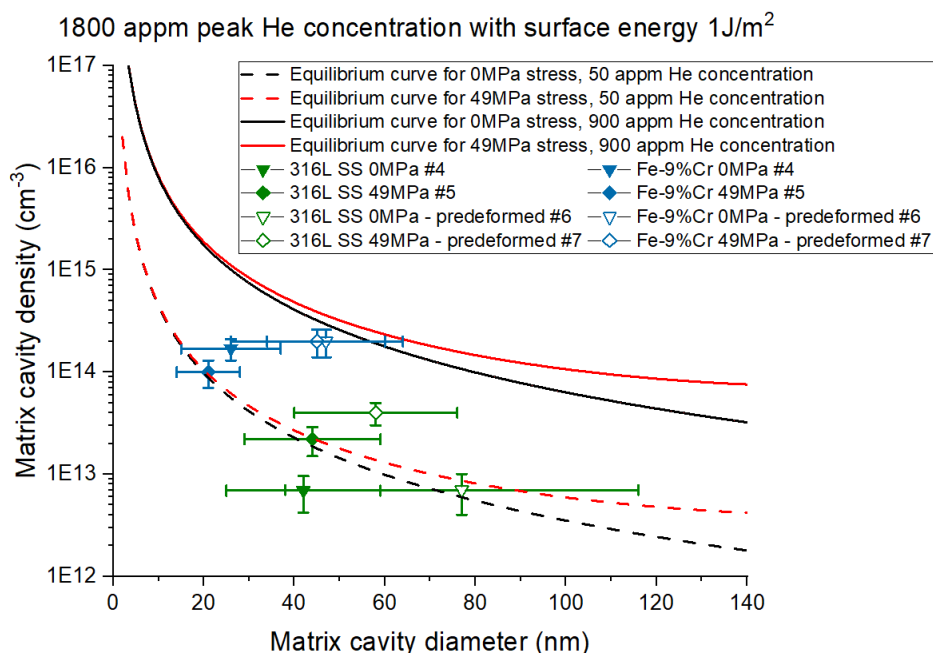


Figure 7. Comparison of the measured average size and number density of matrix cavities in 316LSS and Fe-9%Cr after irradiations #4-#7 with the equilibrium cavity curves calculated for 0 and 49MPa stresses by using 50 and 900 appm He concentrations and 1J/m^2 surface energy.

Results

Based on the current results, the cavity percentages or He atoms contained in cavities were low for both matrix and GB in 316L SS. Therefore, it is considered likely that most of the implanted He atoms diffused to the surface. Since the He implantation peak depth of 8-9 μm is much smaller than the average grain diameter of 40 μm in 316L SS, random walk diffusion of the He-vacancy clusters would result in most of the implanted He diffusing to the surface rather than diffusing to GBs. Therefore, we will perform grain recrystallization by cold working followed by annealing to obtain smaller grain sizes in 316L SS for a future set of He implantations.

Moreover, the effect of dislocation line density and stress cannot be separated due to different initial dislocation line densities and sample surface curvatures induced by pre-bending. To distinguish the effect of dislocation line density and stress, slight cold-working on Fe-9% Cr and 316LSS after grain recrystallization will be conducted to introduce different dislocation line densities homogeneously without causing the sample surface curvature. These samples will be irradiated under the same He implantation conditions as #4-#7. The results of 316L SS and Fe-9%Cr will also be compared to examine any differences between face-centered cubic (FCC) and body-centered cubic (BCC) structures on HTHE resistance.

References

- [1] Z. Qi, S.J. Zinkle, Investigation of High Temperature He Embrittlement Effects in Nickel-based and Iron-based alloys, Fusion Materials Semiannual Progress Report for the Period Ending December 31, 2022, Oak Ridge National Laboratory, pp. 85-92.
- [2] R. Mills, D. Liebenberg, J. Bronson, Equation of state and melting properties of He 4 from measurements to 20 kbar, *Physical Review B* 21(11) (1980) 5137.

1.3 IRRADIATION EFFECT ON THE STABILITY OF MX PRECIPITATE IN FERRITIC MODEL ALLOYS—W. Zhong, Y. Yang (Oak Ridge National Laboratory), E. Proehl (University of Tennessee)

OBJECTIVE

Model alloys with different MX precipitates (tantalum carbide, tantalum nitride) were irradiated in the High Flux Isotope Reactor (HFIR) at approximately 490°C to a dose of 7.4 displacements per atom (dpa). Transmission electron microscopy (TEM) was performed to characterize the precipitates before and after irradiation. The goal of this work is to evaluate the stability of different precipitate under the same irradiation conditions.

SUMMARY

Two different MX precipitates, irradiated at approximately 490°C to a dose of 7.4 dpa, exhibit varying stability. The TaC precipitates demonstrate higher stability under neutron irradiation, with only minor changes to their morphology and size. In contrast, TaN precipitates become longer and thinner after irradiation, with their planes oriented parallel to the {110} planes of the ferritic matrix.

PROGRESS AND STATUS

Focused ion beam (FIB) was performed to prepare TEM samples. Figure 1 shows the bright field (BF), dark field (DF) and the Energy-Dispersive Spectroscopy (EDS) maps (Ta) for the as-received materials. All samples exhibit high densities of nanoscale precipitates, with shapes that are either spherical or oval.

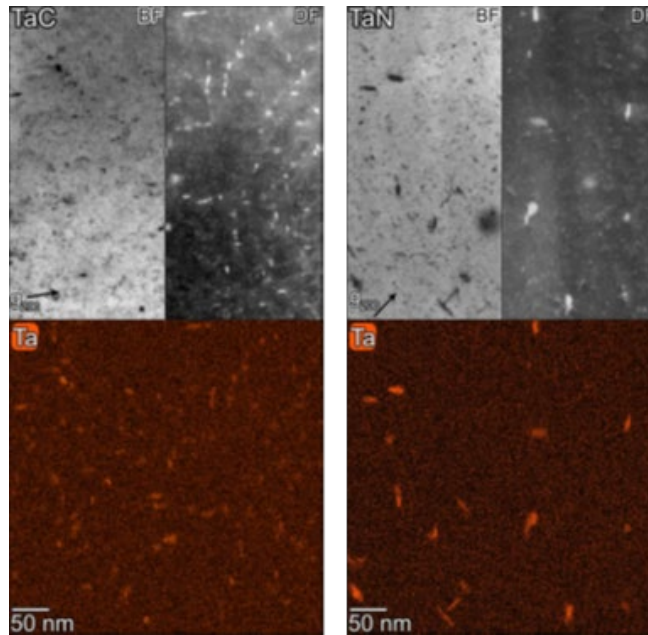


Figure 1. The BF, DF, and EDS maps for (left) TaC, and (right) TaN precipitates in unirradiated ferritic model alloys.

After neutron irradiation, different MX precipitates exhibit different levels of stability. The TaC precipitates appear to be more stable under neutron irradiation, maintaining a similar size compared to before irradiation. In contrast, TaN precipitates become longer and thinner after irradiation, with their planes oriented parallel to the {110} planes of the ferritic matrix. The composition of the precipitates also change after the irradiation, with more tungsten content in TaC precipitates, whereas more Cr content in the TaN precipitates.

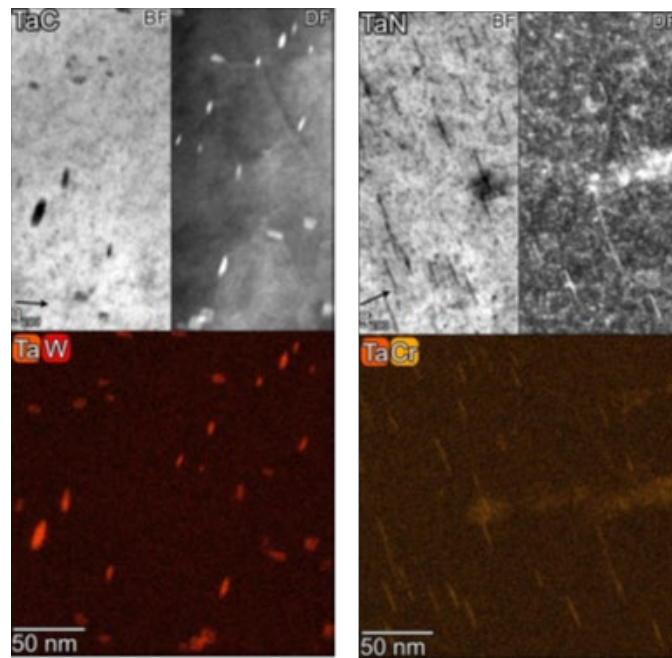


Figure 2. The BF, DF, and EDS maps for (left) TaC, (right) TaN precipitates in irradiated ferritic model alloys.

Results

Atom probe tomography will be used to characterize the composition of MX precipitates before and after neutron irradiation.

1.4 MICROSTRUCTURE EVOLUTION IN PROTON IRRADIATED ULTRA-HIGH PURITY Fe-Cr ALLOYS—S. Chen, S. Zinkle (The University of Tennessee)

OBJECTIVE

Low temperature hardening and embrittlement is a major disadvantage of Fe-Cr ferritic steels for their application in nuclear reactors. The degradations of mechanical property under irradiation are results of microstructure evolution, such as the formation of dislocation loops and redistribution of Cr solute. The objective of this project is to study how dislocation loops and Cr distribution change with irradiation temperature or initial Cr concentration in ultra-high purity Fe-Cr alloys under low-PKA-energy proton irradiation.

SUMMARY

Ultra-high purity Fe-Cr alloys, containing 7.88, 10.10, and 17.97 wt.% Cr, were irradiated by 800 KeV protons with 2×10^{-5} dpa/s dose rate up to 2 dpa in mid-range depth (3 μm) at 250-450 °C. Scanning transmission electron microscopy (STEM) combined with energy dispersive X-ray spectroscopy (EDS) were conducted to investigate the distributions of dislocation loops and Cr. The size of dislocation loops increased, and the number density decreased at higher irradiation temperature or lower Cr content. Dislocation loops with Burgers vectors $a\langle 100 \rangle$ are formed preferentially at higher irradiation temperature, while the ratio between dislocation loops with Burgers vectors $a/2\langle 111 \rangle$ and $a\langle 100 \rangle$ is independent with Cr concentration. We observed the formation of large dislocation loops with size around 100 nm, and number density 2-4 orders of magnitude lower than the “regular-sized” dislocation loops. Cr segregation around dislocation loops in alloys with lower Cr, and Cr rich α' precipitates in matrix in alloys with higher Cr, are observed at lower irradiation temperature.

PROGRESS AND STATUS

The ultra-high purity Fe-Cr alloys, containing 7.88, 10.10, and 17.97 wt.% Cr, namely Fe8Cr, Fe10Cr and Fe18Cr alloys, were manufactured within the framework of the EUROfusion Consortium under contract EFDA-06-1901[1]. The alloys were received as pure ferrite with large grain size (>100 μm) and low dislocation density ($< 10^{12} \text{ m}^{-2}$). The chemical composition of the as-received materials was measured by glow discharge mass spectrometry and is given in Table 1. The alloys were irradiated by 800 keV protons with 2×10^{-5} dpa/s dose rate up to 2 dpa in mid-range depth (3 μm) at 250-450°C. The irradiation matrix is shown in Table 2. The dose and H concentration profile calculated by Stopping and Range of Ions in Matter (SRIM) Full-Cascade option combining damage energy method [2-4] and a displacement energy of 40 eV are shown in Figure 1.

Table 1. Chemical composition of Fe-Cr alloys

	Cr (wt.%)	C (ppm)	S (ppm)	O (ppm)	N (ppm)	P (ppm)
Fe8Cr	7.88	<6	<1	<6	<2	-
Fe10Cr	10.10	4	4	4	3	<5
Fe18Cr	17.97	7	2	6	5	-

Table 2. Irradiation matrix of 800 keV proton to Fe-Cr alloys

	Irradiation Temperature (°C)	Flux (ions/cm ² ×s)	Fluence (ions/cm ²)
Fe-8Cr	250	1.75×10 ¹⁴	1.75×10 ¹⁹
Fe-10Cr	250		
	350		
	450		
Fe-18Cr	250		

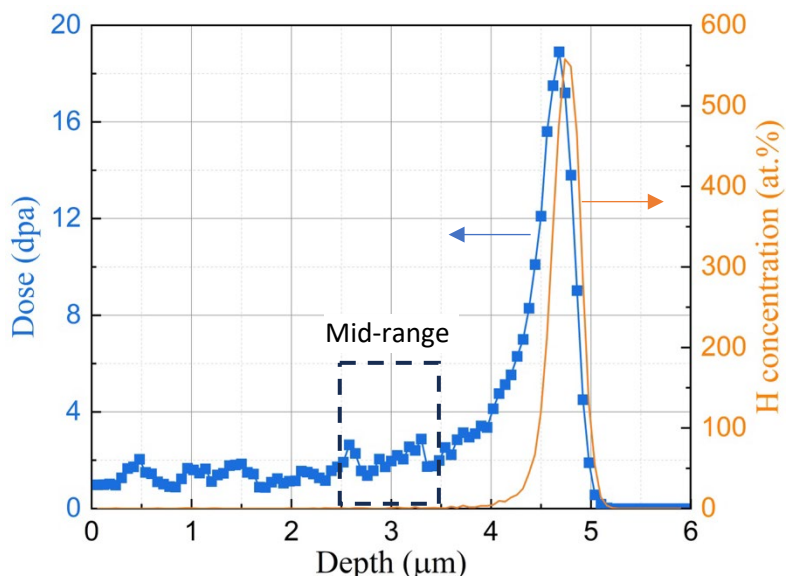


Figure 1. Dose and H concentration profile calculated by SRIM for 800 keV proton ions in Fe with the fluence of $1.75 \times 10^{19}/\text{cm}^2$ at 3 μm depth.

After irradiation, cross-sectional TEM samples were prepared by an FEI Helios 5 Hydra CX plasma focused ion beam (FIB). The lamellae were thinned down to 150-250 nm with Xe ions at 30kV, followed by flash electropolishing to remove the FIB damage on the surfaces. The flash electropolishing was conducted in 3% HClO_4 -ethanol electrolyte with 65-120V at -65°C for 60 ms. The structure of dislocation loops and the redistribution of Cr were characterized using a Thermo Fisher Spectra 300 microscope operated at 200 kV in STEM mode.

Figure 2 shows cross-sectional STEM-bright field (BF) images in $[001]$ zone axis for the proton irradiated Fe-8Cr, Fe-10Cr, and Fe-18 Cr alloys at 250-450 $^\circ\text{C}$. For all the irradiated samples, the penetration depth of dislocation loop is $\sim 1 \mu\text{m}$ deeper than that predicted by SRIM calculation. The discrepancy can be attributed to slight errors in the SRIM stopping power database calculation. The penetration depth appeared increase with decreasing irradiation temperature. Three variants of $a\langle 100 \rangle$ loop rafts are formed beyond the damage peak at 350 $^\circ\text{C}$. The formation of loop rafts may be due to high implanted H concentration and/or irradiation temperature. The calculated depth region of interest for quantitative analysis. The dislocation loops are divided into 'regular dislocation loop' and 'large dislocation loop' according to their dramatic difference in size. With a low magnification, the regular dislocation loops are shown as dots dispersing in samples at 250 and 350 $^\circ\text{C}$. The large dislocation loops are shown in a darker contrast with size more than 3-4 times larger than the mean diameter of the regular dislocation loops. Examples of some large dislocation loops are indicated with arrows in the figure. At 450 $^\circ\text{C}$, the size of the regular dislocation loops reach $\sim 100 \text{ nm}$, whereas we don't observe 'large dislocation loops' whose size should be 3 times of that of the regular dislocation loops. The formation of large dislocation loops is suppressed around the damage peak at 250 $^\circ\text{C}$, where a high implanted H concentration exists. The suppression might be attributable to that the injected protons stabilizing the radiation induced defects.

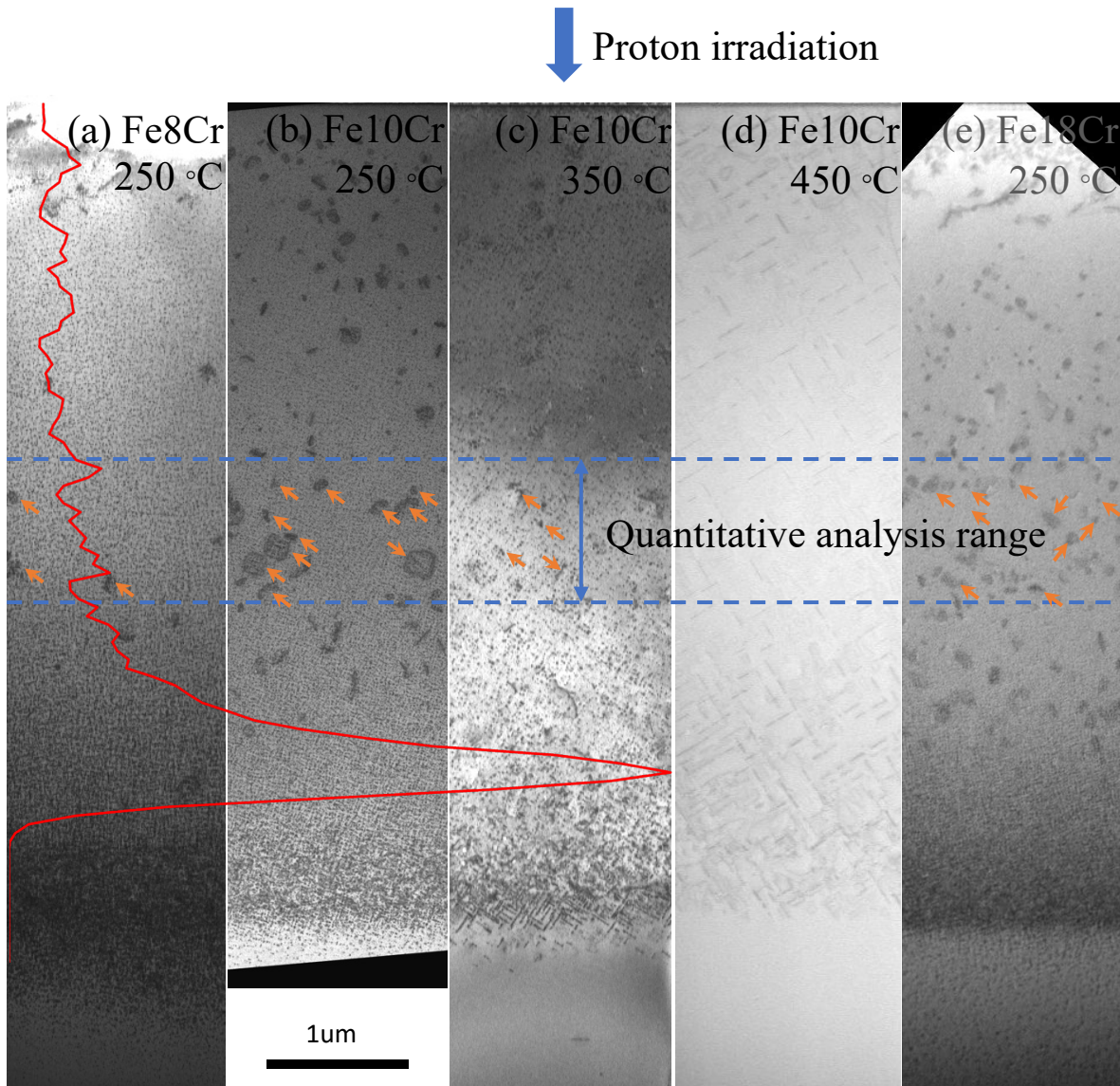


Figure 2. Cross-sectional STEM-BF images in $\langle 001 \rangle$ zone axis show dislocation loops for (a) Fe8Cr (b) Fe10Cr irradiated at 250°C, (c) Fe10Cr irradiated at 350 °C, (d) Fe10Cr irradiated at 450°C, and (e) Fe18Cr irradiated at 250°C. The direction of proton irradiation and the displacement profile are indicated in the image. The arrows indicate some examples of large dislocation loops. Dashed lines indicate midrange for quantitative analysis.

The size and the number density of the regular dislocation loops and the large dislocation loops as a function of Cr content and irradiation temperature are summarized in Table 3 and Table 4. Higher Cr content resulted in smaller regular dislocation loops with a higher number density. The mean diameter and the number density of the regular dislocation loops increases and decreases respectively with irradiation temperature increasing. We noticed that the size of the regular dislocation loops increased by one order of magnitude at 450°C for the Fe10Cr alloy. The rapid growth of the regular dislocation loops may suggest the coalescence of the dislocation loops. For the large dislocation loops, the diameter of the dislocation loops is on the same order as or even exceeding the TEM lamellar thickness. A substantial fraction of large dislocation loops would be truncated by the TEM lamellae; thus, the actual loop size is underestimated, and

the number density is overestimated. Since the size of the large dislocation loops is highly dependent on the thickness of the TEM sample at 250°C, we cannot conclude the evolution trend in size with Cr content at 250°C. The number density of the large dislocation loops increases with Cr content. Both the size and the number density of the large dislocation loops appeared to decrease with irradiation temperature increasing. The reason could be the shrinkage of the large dislocation loops, or the interaction of dislocation loops therefore lose the loop morphology at higher irradiation temperature. A mixed population of regular dislocation loops with Burgers vectors $a/2\langle 111 \rangle$ and $a\langle 100 \rangle$ were observed at 250 and 350°C. At 450°C, we only observed regular dislocation loops with Burgers vectors $a\langle 100 \rangle$. The number ratio between regular dislocation loops with Burgers vectors of $a/2\langle 111 \rangle$ and $a\langle 100 \rangle$ seems independent on Cr content, while the ratio decreases with increasing irradiation temperature. Only regular dislocation loops with Burgers vectors of $a\langle 100 \rangle$ remain at 450°C.

Table 3. Dislocation loop evolution as a function of Cr content at irradiation temperature of 250°C

Material	Regular loop					Large loop			
	Diameter (nm)			Number density (10^{22} m^{-3})		Diameter (nm)			Number density (10^{22} m^{-3})
	Mean	Min.	Max.	111 loop	100 loop	Mean	Min.	Max.	
Fe-8Cr	4.8	1.4	13.9	2.19	0.156	95.9	32.3	152.3	9.3E-4
Fe-10Cr	3.9	1.2	14.6	3.25	0.212	103.6	17.8	204.7	0.0065
Fe-18Cr	3.2	1.1	7.7	7.36	0.481	72.9	27.8	209.6	0.022

Table 3. Dislocation loop evolution as a function of irradiation temperature in irradiated Fe-10Cr alloy

Temperature (°C)	Regular loop					Large loop			
	Diameter (nm)			Number density (10^{22} m^{-3})		Diameter (nm)			Number density (10^{22} m^{-3})
	Mean	Min.	Max.	111 loop	100 loop	Mean	Min.	Max.	
250	3.9	1.2	14.6	3.25	0.212	103.6	17.8	204.7	0.0065
350	7.4	1.7	16.1	0.273	0.174	79.9	21.9	150.4	0.0057
450	84.3	13.9	203.4	0	0.039	-	-	-	0

Figure 3 shows STEM images of dislocation loops and corresponding EDS elemental mapping of Cr in the midrange depth at 250-450°C in Fe (8-18)Cr alloys. The lateral axis represents Cr content. The vertical axis represents irradiation temperature. The STEM images in the same field of view are coupled to show the distribution of dislocation loops (left) and Cr mapping (right). In Figure 9 (a), Cr is enriched around dislocation loops in Fe8Cr at 250°C. With increasing Cr content, dislocation loops become smaller in size, and Cr enrichment transfers from segregation at dislocation loops to fine-scale clustering in the matrix. A mixed population of Cr-rich dislocation loops and α' precipitates is found at 250°C in the Fe10Cr alloy, while only α' precipitates are finely dispersed in the matrix in the Fe18Cr alloy. The Cr segregation around dislocation loops decreases with increasing Cr concentration. The bright tiny particles in the Cr map reveals the formation of irradiation enhanced α' precipitates. The heterogeneous Cr segregation around dislocation loops show a larger characteristic size than α' precipitates. The Cr segregation or α' phase decreases at higher irradiation temperature in Fe10Cr alloy.

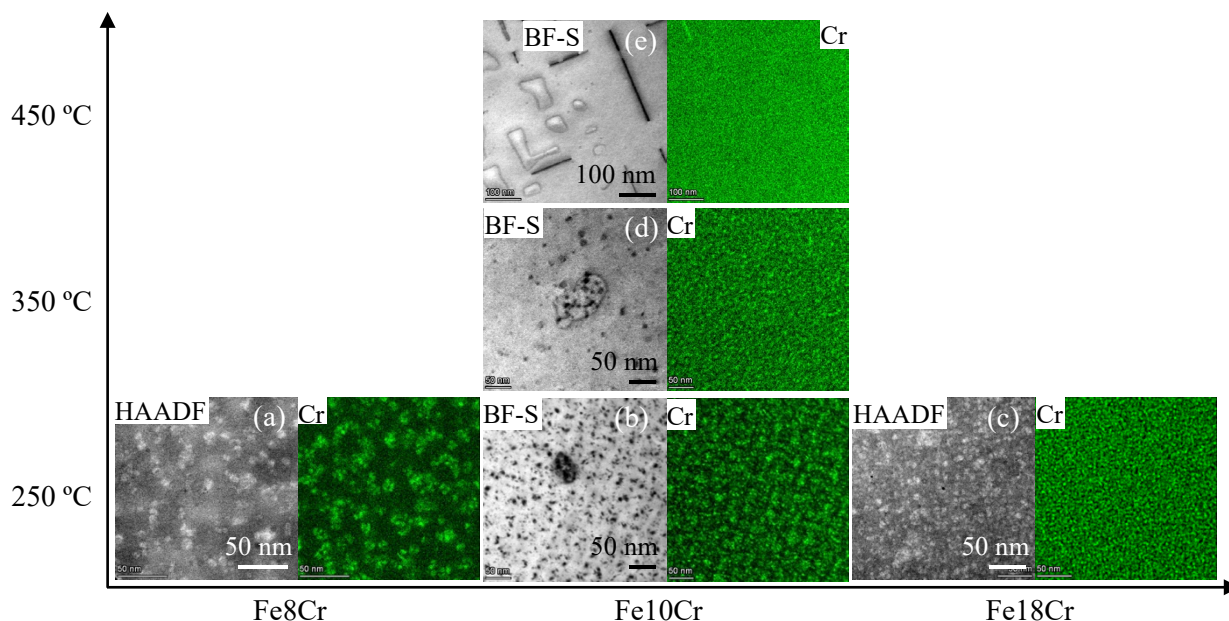


Figure 3. The STEM-BF or High-angle annular dark-field (HAADF) image coupled to Cr elemental mapping in mid-range depth for (a) Fe8Cr (b) Fe10Cr (c) Fe18Cr irradiated at 250°C, (d) Fe10Cr irradiated at 350°C, and (e) Fe10Cr irradiated at 450°C. The dark contrast in STEM-BF image or the bright contrast in HAADF image shows dislocation loops. The STEM-EDS image on right shows the distribution of Cr in the same field of view.

Results

We have investigated the evolution of dislocation loops and redistribution of Cr as a function of Cr content and irradiation temperature. We observed the formation of the “large dislocation loop” and “regular dislocation loop”. However, there are no known previous reports of such a bimodal loop size distribution with large dislocation loops under irradiations. The formation mechanism for the large dislocation loops needs further investigation. On the other hand, the rapid growth of regular dislocation loops at 450°C can be related to the coalescence of dislocation loops. More details about the evolution of regular dislocation loops with irradiation temperature will be discussed.

The Cr redistribution has been studied qualitatively. The formation of heterogeneous Cr segregation around dislocation loops for alloys with lower Cr content, and homogeneous Cr-rich α' precipitates for higher Cr alloys have been revealed by STEM-EDS mapping. The addition of Cr has been considered to trap the fast-diffusing Fe self-interstitial atoms (SIA), resulting in Fe interstitial-initiated mixed dumbbells. Another interesting mechanism is Cr-initiated mixed dumbbells [5], in which Cr interstitials form directly in cascades, and then Cr interstitials displace the nearby Fe lattice atoms. Moreover, we observed that Cr segregation happens on some dislocation loops but is less pronounced on other loops. A possible reason is the fluctuation of local small Cr clusters assists Cr interstitial initiated dislocation loops. The interaction between solute and defect (including dislocation loop, grain boundary) will be investigated quantitatively in future work.

References

- [1] J.L. Coze, Procurement of Pure Fe Metal and Fe-Based Alloys with Controlled Chemical Alloying Element Contents and Microstructure: Final Report on Model Alloy Preparation.
- [2] R.E. Stoller, M.B. Toloczko, G.S. Was, A.G. Certain, S. Dwaraknath, F.A. Garner, On the Use of SRIM for Computing Radiation Damage Exposure, Nucl. Inst. Methods Phys. Res. B. 310 (2013) 75–80.

- [3] S. Agarwal, Y. Lin, C. Li, R.E. Stoller, S.J. Zinkle, On the Use of SRIM for Calculating Vacancy Production: Quick Calculation and Full-Cascade Options. *Nucl. Inst. Methods Phys. Res. B.* 503 (2021) 11–29. <https://doi.org/10.1016/j.nimb.2021.06.018>.
- [4] Y. Lin, S.J. Zinkle, C.J. Ortiz, J.P. Crocombette, R. Webb, R.E. Stoller, Predicting Displacement Damage for Ion Irradiation: Origin of the Overestimation of Vacancy Production in SRIM Full-Cascade Calculations. *Curr. Opin. Solid State Mater. Sci.* 27 (2023) 101120. <https://doi.org/10.1016/j.cossms.2023.101120>.
- [5] Y. Zhang, D. Schwen, X. Bai, Molecular Dynamics Simulations of Concentration-Dependent Defect Production in Fe-Cr and Fe-Cu Alloys. *J. Appl. Phys.* 122 (2017) 225902. <https://doi.org/10.1063/1.5008757>.

1.5 MICROSTRUCTURE EVOLUTION IN BCC PURE Fe AT DIFFERENT TEMPERATURES AFTER ENERGETIC SELF-ION IRRADIATION—Y. Li, Z. Qi, S. Zinkle (University of Tennessee)

OBJECTIVE

The objective of this task is to study the temperature, dose rate, and dose effects on dislocation loop size and type in high-purity Fe after self-ion irradiation.

SUMMARY

Dislocation loops are examined in Ultra-high purity (UHP) iron irradiated by 6.7 and 8 MeV Fe²⁺ ions to midrange doses of 3.5 dpa at 250-500°C. Scanning transmission electron microscopy (STEM) was used to characterize the size, density, and type of loops. We examine the effect of temperature, dose rate and dose on the formation of dislocation loops using detailed Burgers vector analysis **g·b** method combined with weak-beam-dark-field (WBDF) STEM.

PROGRESS AND STATUS

This report summarizes recent work on dislocation loop characterization in ion irradiated high-purity Fe; The irradiations were performed at The Michigan Ion Beam Laboratory (MIBL). Defocused beam mode was employed in irradiations. The irradiations temperature monitoring system includes four thermocouples and a thermal imaging system. The thermocouples were welded on guide bars next to samples and the thermal imaging system was calibrated prior to each irradiation. The irradiation conditions are listed in Table 1. The TEM foils were prepared by focused ion beam (FIB) techniques. Each foil was intentionally lifted out from the interior of large grains and situated several tens of micrometers from any grain boundaries. This placement was designed to mitigate potential confounding influences associated with these structural features. Furthermore, to remove defects induced by FIB, flash electropolishing technique was employed on the foils.

Table 1. Irradiation conditions for pure Fe samples

Ion energy (MeV)	Midrange dose (dpa)	Fluence (ions/cm ²)	Midrange dpa rate (dpa/s)	Temp. (°C)	Irradiation time (hour)
8	3.5	8.83×10 ¹⁵	10 ⁻⁴	250 ± 7	11.2
8	3.5	8.83×10 ¹⁵	10 ⁻⁴	350 ± 8	10
6.7	3.5	8.83×10 ¹⁵	10 ⁻⁴	450 ± 3	10
8	3.5	8.83×10 ¹⁵	10 ⁻⁴	500 ± 6	9.9

The influence of temperature on loop formation was investigated at a dose rate of 10⁻⁴ dpa/s and a total midrange dose of 3.5 dpa from 250°C to 500°C. Figures 1a-1d illustrate the general cross-sectional microstructures from the irradiated surface to the ion-implanted region, while Figures 1e-1h present these structures at higher magnification within the designated 'safe analysis regions', which was recommended by Zinkle et al [1]. In the sample irradiated at 250°C (Figure 1a), large loops were not observable in the safe analysis region. Instead, the predominant features are tiny dots, about 3 nm in diameter (Figure 1e), and highly decorated dislocations in the ion-implanted region (approximately 2 μm depth). At 350°C, loops are distributed somewhat heterogeneously across the safe analysis and ion-implanted regions (Figures 1b and 1f). For the samples irradiated at 450 and 500°C (Figures 1c and 1d), extended dislocation segments were imaged throughout the entire damaged area, from the surface down to 2.5 μm depth. Higher magnification reveals, in addition to the long dislocation segments, a moderate density of tiny dots (Figures 1g and 1h),

These fine-scale features are not damages induced by FIB which were eliminated during the flash electropolishing process. As a reference, Figure 2 displays an unirradiated Fe FIB foil cleaned by flash electropolishing technique. No tiny dots were observable in this foil.

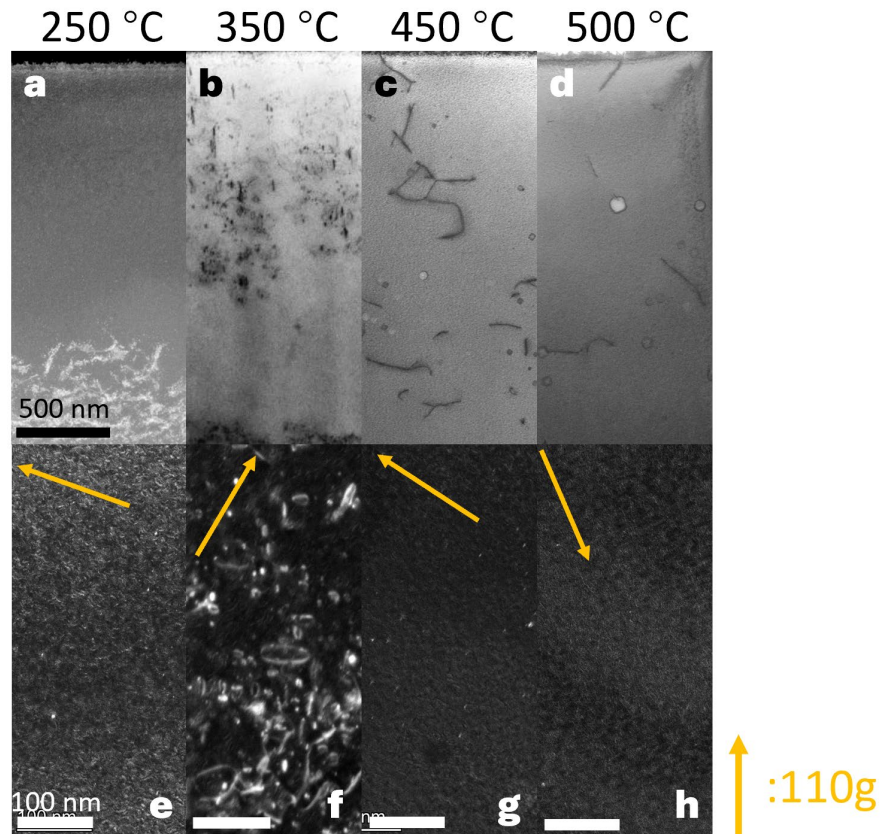


Figure 1. The STEM micrographs of Fe samples irradiated to a dose of 3.5 dpa at a rate of 10^{-4} dpa/s and temperatures ranging from 250°C to 500°C are presented. The top micrographs (a-d) illustrate the general cross-sectional microstructural features observed in the damaged regions under STEM on-zone imaging conditions. A 500-nm scale bar, applicable to all top micrographs, is included in the top panel. The bottom micrographs (e-h) depict the midrange safe analysis region for each Fe sample, imaged under (g,3g) STEM WBDF. A 100-nm scale bar, relevant for all bottom micrographs, is shown in the bottom panel. Pink arrows indicate the $g=110$ diffraction vector direction, with B approximately aligned with 100.

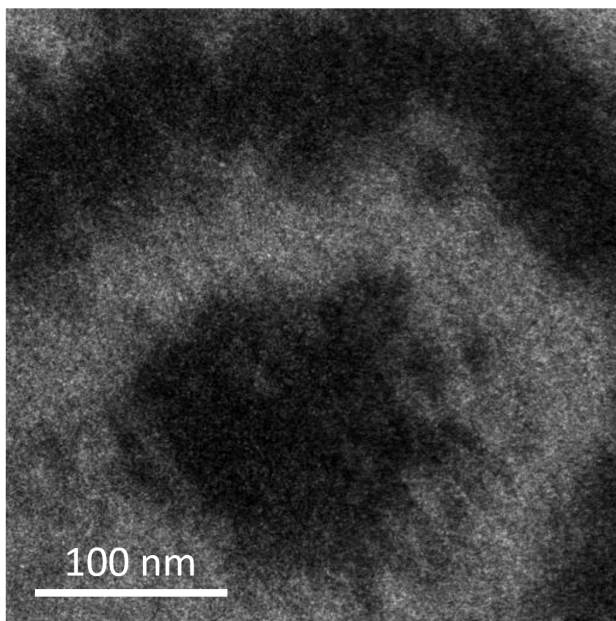


Figure 2. The WADF-TEM micrograph of an unirradiated Fe foil cleaned by flash electropolishing method. The flash electropolishing parameter applied to this foil is identical to those applied to samples in Figure 1.

Some $\langle 100 \rangle$ and $\frac{1}{2} \langle 111 \rangle$ loops were observed in the irradiated Fe samples at all temperatures. Since the samples studied here are all high-purity Fe, it is not possible that the tiny dots were another phase. It is reasonable to believe they are all dislocation loops. The statistical data regarding dislocation loops are shown in Figure 3. The $g \cdot b$ analysis was carried out on all samples. Unfortunately, the $\langle 100 \rangle$ fraction could not be determined in Fe irradiated at 250°C, since the dimension of the sample surface texture was similar to the dimension of tiny dislocation loops, shown in Figure 1e. The $\langle 100 \rangle$ loop fraction vs temperature did not exhibit a monotonic dependence on irradiation temperature between 350 and 500°C: the $\langle 100 \rangle$ fraction was lowest at 450°C, with 20% of all the analyzed loops identified as $\langle 100 \rangle$ loops. The loop number densities, mean diameter, and distributions were categorized into all loops, $\langle 100 \rangle$ loops, and $\frac{1}{2} \langle 111 \rangle$ loops in Figure 3c-f. The overall loop density decreased with increasing irradiation temperature (Figure 3b) but the $\frac{1}{2} \langle 111 \rangle$ loop density peaked at 450°C. This was due to the increased fraction of $\frac{1}{2} \langle 111 \rangle$ loops at 450°C. The $\frac{1}{2} \langle 111 \rangle$ loop mean diameter was much larger than the mean diameter of $\langle 100 \rangle$ loops (26 nm vs 15 nm) in the Fe sample irradiated at 350°C. In contrast, once the irradiation temperatures were above 350°C, the mean visible loop diameter dropped to ~ 4 nm for all three different loop categories (all, $\frac{1}{2} \langle 111 \rangle$, and $\langle 100 \rangle$). The loop diameter distributions are shown in Figures 3d-f. The loop distributions observed in Fe irradiated at 350°C were much wider than the distributions observed in Fe at 450°C and 500°C, leading to large standard deviation in Figure 3c at 350°C. Regarding dislocation line segment in pristine sample and samples irradiated at 350-500°C, the $g \cdot b$ analysis was carried out as well. Compared with a pristine sample, observable dislocation line segment density in midrange safe analysis regions increased in Fe after irradiation. The dislocation line density increased from $1 \times 10^{12} \text{ m}^{-2}$ (pristine Fe sample) up to $1.4 \times 10^{13} \text{ m}^{-2}$ in irradiated Fe. Amongst identified dislocation line segments in samples irradiated from 350-500°C, the fractions of $\langle 100 \rangle$ dislocation line segment were 9% at 350°C, 14% at 450°C, and 20% at 500°C, respectively.

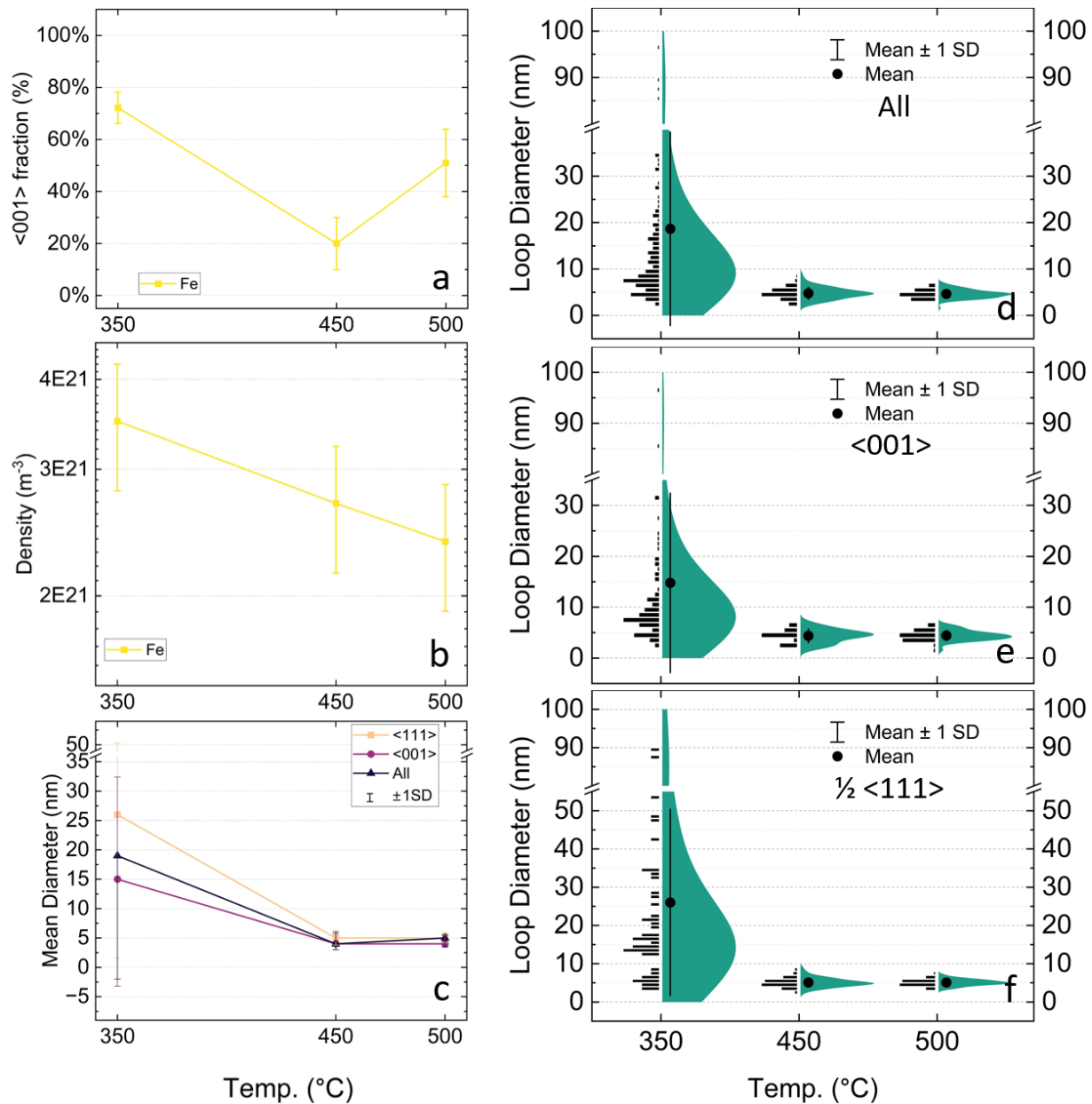


Figure 3. The statistical data regarding dislocation loops in this study. (a) <100> loop fraction.

Results

It is widely accepted that radiation-induced <100> loops fraction monotonically increases in Fe with increasing irradiation temperatures. In the in-situ experiments by Yao et al. [24], the microstructural evolution at 400-500°C with increasing doses was recorded. When the damage level was below 1.3 dpa, the major defects reported were highly mobile defects along <111> directions, indicating the observed defects at this stage were mainly <111> loops. When the damage level was > 1.3 dpa, the elastic interaction between defects started to be noticeable and the <100> loop population grew and took dominance at 13 dpa. In our irradiations, the doses were 0.35 and 3.5 dpa. Despite the apparent divergence in nominal dpa values compared to Yao's experiments, the fluences measured by the number ions per unit area were actually very close ($2 \times 10^{15} \text{ cm}^{-2}$ in Yao's experiment vs $8.83 \times 10^{15} \text{ cm}^{-2}$ in this study). The dpa dissimilarity

was mainly induced by the choice of displacement energy, with a secondary effect associated with difference in ion energies (~5 MeV in the midrange region for our study, vs. <400 keV for Yao's study). In Yao's experiments, the displacement energy (E_d) was set as 24 eV in SRIM [2]. In contrast, in accordance with ASTM E521, $E_d = 40$ eV was applied in this study. Therefore, to make a better comparison between our observation and Yao's observation at 13 dpa, based on the fluence (2×10^{15} ions/cm²) and ions with 150 keV, we reevaluated the damage profile for his study using 40 eV E_d in Stopping and Range of Ions in Matter (SRIM)-2013. Yao et al.'s experiment was performed at the Argonne-IVEM Tandem Facility. The angle between the ion beam and the electron beam of TEM was 30° [3]. Two setups were simulated: ion beam is 0° and 30° from TEM foil normal. With 40 eV E_d , the calculated peak damage levels are 4 dpa (0°) and 4.5 dpa (30°) rather than the peak value of 13 dpa reported by Yao et al. This damage level is very close to the 3.5 dpa midrange dose in our study. The implanted ion concentration is ~0.4 at% (close to 0.2 at% peak implanted ions in our study). By applying anisotropic elasticity, Dudarev et al. [4] and Gao et al. [5] predicted that the free energy ratio between $\frac{1}{2} \langle 111 \rangle$ and $\langle 100 \rangle$ loop would gradually increase with increasing temperature, and above ~ 400°C $\langle 100 \rangle$ loops would be more energetically favorable per unit length. However, our results did not keep in line with these calculated predictions. Similarly, a positive relationship between $\langle 100 \rangle$ fraction and irradiation temperature was not observed in other ion irradiations on bulk samples [6-8]. Thus, the dominance of irradiation-induced $\langle 100 \rangle$ loop in pure Fe is supposed to be controlled by other mechanism(s), which will be explored in our future studies.

References

- [1] S.J. Zinkle, L.L. Snead, Opportunities and limitations for ion beams in radiation effects studies: Bridging critical gaps between charged particle and neutron irradiations, *Scripta Materialia* 143 (2018) 154-160.
- [2] Z. Yao, M. Hernández-Mayoral, M.L. Jenkins, M.A. Kirk, Heavy-ion irradiations of Fe and Fe–Cr model alloys Part 1: Damage evolution in thin-foils at lower doses, *Philosophical Magazine* 88(21) (2008) 2851-2880.
- [3] M. Li, M.A. Kirk, P.M. Baldo, D. Xu, B.D. Wirth, Study of defect evolution by TEM with in situ ion irradiation and coordinated modeling, *Philosophical Magazine* 92(16) (2012) 2048-2078.
- [4] S.L. Dudarev, R. Bullough, P.M. Derlet, Effect of the α - γ Phase Transition on the Stability of Dislocation Loops in bcc Iron, *Physical Review Letters* 100(13) (2008) 135503.
- [5] J. Gao, E. Gaganidze, J. Aktaa, Parameterization on formation free energy of dislocation loops up to 1100 K in bcc iron, *Journal of Nuclear Materials* 559 (2022) 153409.
- [6] J. Chen, F. Duval, P. Jung, R. Schäublin, N. Gao, M.F. Barthe, Dislocation loops in ultra-high purity Fe(Cr) alloys after 7.2 MeV proton irradiation, *Journal of Nuclear Materials* 503 (2018) 81-90.
- [7] S. Xu, Z. Yao, M.L. Jenkins, TEM characterisation of heavy-ion irradiation damage in FeCr alloys, *Journal of Nuclear Materials* 386-388 (2009) 161-164.
- [8] A. Prokhodtseva, B. Décamps, R. Schäublin, Comparison between bulk and thin foil ion irradiation of ultra high purity Fe, *Journal of Nuclear Materials* 442(1, Supplement 1) (2013) S786-S789.

2. ODS AND NANOCOMPOSITED ALLOY DEVELOPMENT

2.1 COLD SPRAY AND FRICTION STIR PROCESSING OF ODS ALLOYS ON A FERRITIC MARTENSITIC STEEL SUBSTRATE—D. Zhang, X. Wang, J. Darsell, K. Ross, L. Li, W. Setyawan (Pacific Northwest National Laboratory)

OBJECTIVE

The objective of this work is to explore alternative route of fabricating oxide dispersion strengthened (ODS) alloys, including the potential of plating such ODS plate onto a substrate of reduced activation ferritic martensitic (RAFM) steel. We have demonstrated successful cold spray of ODS steel powder onto ferritic martensitic steel (P92) plates. Two large plates, i.e., #1 and #2, were prepared for subsequent development of friction stir processing (FSP) to (a) eliminate pores and defects in cold sprayed deposit and fully densify ODS steel; (b) further disperse Y-(Ti)-O particles with severe plastic deformation in FSP; (c) maintain and possibly improve bonding between ODS steel deposit and the substrate. In addition, the cold spray + FSP workflow is also being used to incorporate a thin “interlayer” material between ODS plate and the substrate, with the goal of using an interlayer to enhance the bonding between ODS steel and tungsten or tungsten heavy alloys.

SUMMARY

Cold spray was used to successfully deposit ODS steel powder onto ferritic martensitic steel (P92) plate. The feedstock ODS steel powder was provided by collaborators at Ames Laboratory, made with their unique gas atomization reaction synthesis (GARS). The GARS ODS steel powder had the nominal composition of 14YWT (14Cr-0.4Ti-3W-0.35Y-0.1O, wt.%). Meanwhile the largely spherical powder was not ball milled, hence it can be cold sprayed. The P92 steel plate was used as a surrogate for RAFM steel, having nominal composition of 9Cr-2W-Si0.5-Mn0.5-Mo0.4-Ni0.3-V0.2-C0.1, wt.%. The state-of-the-art cold spray system was used with helium carrier gas and robust processing parameters to ensure good deposition quality. Subsequently FSP was successfully used to further process the cold sprayed plates. Multiple “single pass” FSP runs were performed on plate #1 to optimize FSP parameters, including FSP tool plunge depth, compression force, and automated temperature control program. The #2 plate was processed with a multi-pass FSP raster to impact an extended area (i.e., ~4” long, ~3” wide), followed by another iteration of cold spray and FSP, resulting in a solid ODS steel plate of ~5 mm thickness on P92 steel substrate. Preliminary microstructure characterization and mechanical testing were performed for plate #2. In addition, to explore joining ODS steel to W-Ni-Fe tungsten heavy alloys, cold spray of ~1 mm thick layer of pure Ni powder followed by ~2 mm thick of GARS ODS steel powder on P92 steel substrate were done. Such a composite deposit underwent FSP, and the cross-section was examined with optical microscopy and hardness.

PROGRESS AND STATUS

Introduction

The conventional fabrication route [1] of ODS steel plate involves production of powder by gas atomization, ball milling, powder vacuum canning, hot isostatic pressing, hot cross rolling, cold rolling, with annealing steps often required in-between rolling steps. This route is time consuming, expensive, hard to scale up, and extremely delicate as cracks can develop and the plate can “bend out of shape” during the laborious rolling process. Based on the realistic consideration that conventional route is not capable of producing tons of ODS steel for fusion energy application, some researchers [1] proposed to “plate” a mm-level thickness of ODS steel onto RAFM steel, with the idea that the ODS steel plating would be a critical top layer to handle expected extreme temperature and radiation dose in a fusion environment. This means that on top of the laborious plate fabrication process, additional bonding step (e.g., diffusion bonding) is required to make ODS steel plating. Therefore, it would be highly desirable to directly deposit an ODS steel layer onto a RAFM steel without the abovementioned laborious steps. Unfortunately, melt-based additive methods won't be suitable as dispersed particles tend to agglomerate in molten metal. Cold spray is a solid-state based method that could offer a potential solution. Yet effective cold spray would require the feedstock

powder to be largely spherical for aerodynamic purposes. Namely, the flaky ball milled ODS steel powder won't work well with cold spray.

The GARS method produces spherical precursor ODS steel powder with an outer shell of Cr-rich oxide, whereas the nano-oxide forming species, i.e., Y and Ti, are at the powder interior in the form of Fe-intermetallics. Upon heating and consolidation (e.g., hot isostatic pressing [HIP]), oxygen atoms diffuse into the powder interior to react with Y/Ti, forming the Y-Ti-O nano-oxides [2]. Therefore, GARS ODS steel powder offers the geometrical (i.e., spherical) and compositional (i.e., Y/Ti/O species all contained in the powder) requirements for cold spray deposition. Moreover, FSP can be used to further process the GARS ODS steel powder cold spray deposit, leading to full consolidation of the bulk material and further disperse the formation of Y-Ti-O particles.

Experimental Procedure

Figure 1(a) shows a cross-section overview in a scanning electron microscope (SEM) of the GARS ODS steel powder provided by Ames Laboratory. The powder size ranges between 45 μm and 108 μm . Figure 1(b) is a medium magnification SEM image of several powder particles, showing the grain substructure inside. Figure 1(c) is a high magnification image inside one powder particle, showing bright spots mainly decorating grain boundaries. Energy dispersive X-ray spectroscopy (EDS) mapping in Figure 1(d) reveals that these bright spots correspond to Y signals, namely these are Fe-Y intermetallic particles.

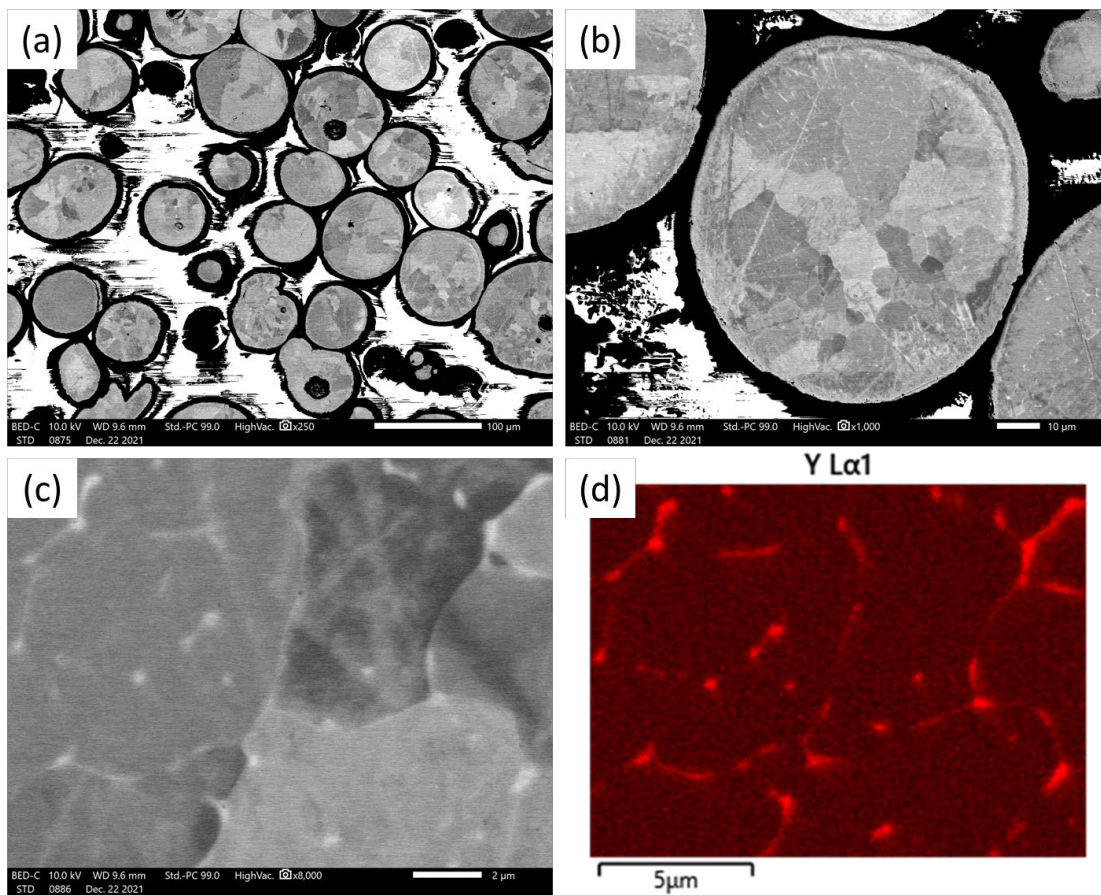


Figure 1. (a) Cross-section SEM overview of the GARS ODS steel powder. (b) Grain substructure inside powder particles. (c) Bright spots decorating grain boundaries. (d) The EDS map showing that the bright spots are Fe-Y intermetallic particles.

The P92 steel substrates had an as-machined surface which could be beneficial for bonding at the cold spray interface. Based on prior experience with steels and Ni alloys, a set of robust cold spray parameters was chosen to ensure effective deposition and preserve limited GARS powder. For example, helium carrier gas was used at 600 psi, with the gas temperature at 650°C. It is noted that 650°C would still be considered “cold” for ODS steel powder since such a temperature would not alter the powder microstructure. As shown in Figure 2, two large-area ODS steel deposits (#1 and #2) were cold sprayed onto P92 substrates, respectively. The #1 was used for optimization of the FSP step, where four trail FSP passes were performed. First to determine the optimal FSP tool plunge depth where abundant material was getting processed while also ensuring that the tool was not “buried” in the material to the point of damaging the tool itself. Then the compression force on the FSP tool was fine tuned to enable temperature controlled FSP run (at 750°C) through a combination of steady force and tool rotation speed (rotation per minute, i.e., RPM). After these optimizations, a “1.5” pass was performed where after one complete pass along the “X” direction for 4”, the tool traversed in the “Y” direction for 8 mm then travelled back in the “X” direction again for 2”. In this way, cross-section samples can be extracted from the tracks of both the single pass and the “overlapping” 2 passes. Upon examination of the two samples with optical microscopy (OM) and hardness mapping, #2 plate was FSP processed with an 8-pass raster.

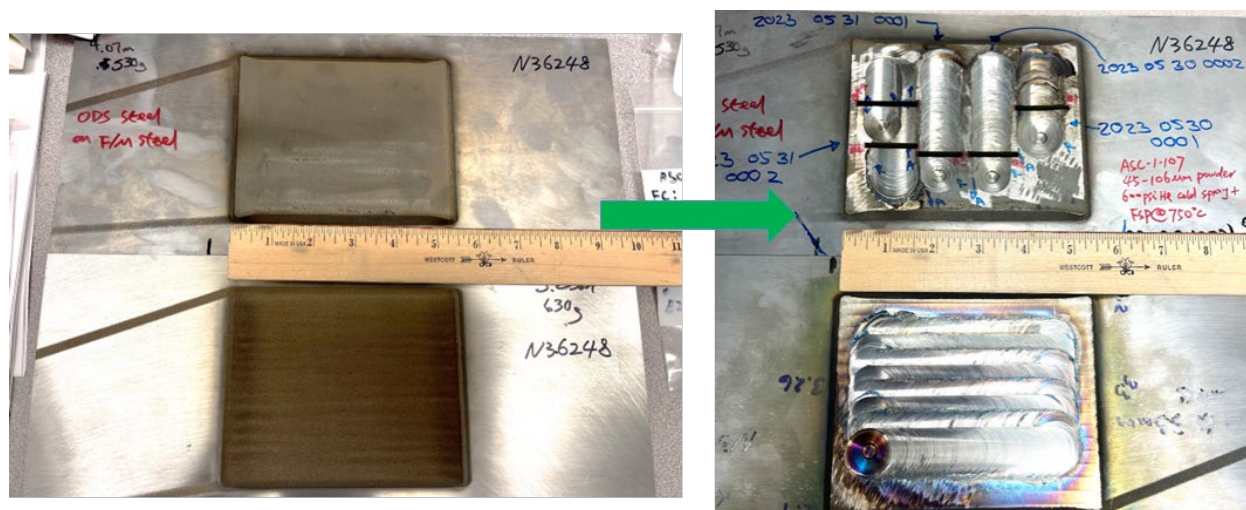


Figure 2. Two large-area ODS steel deposits (#1 and #2) were cold sprayed onto P92 substrates, respectively. The #1 plate was used for optimization of the FSP step. The #2 plate was FSP processed with an 8-pass raster.

Results

Figure 3(a) shows the #2 plate after the second iteration of cold spray and FSP (also 8-pass raster), yielding a total ODS layer thickness of ~5 mm. The yellow dashed box outlines the cross section extracted from the plate, crossing the 8-pass processed area as well as a small portion of as-cold spray areas at the two ends. The red dashed boxes outline the portions of the processed area extracted for making creep test specimens. Note that specimens along the FSP longitudinal and transverse directions were tested. Figure 3(b) shows the OM montage image of the extracted cross section, containing both the ~5 mm ODS layer (top) and the P92 steel substrate (bottom). No cracks or defects can be seen between the processed ODS layer and the substrate. The hardness map also indicates a very uniform structure in the processed area, with the average hardness ~200 HV.

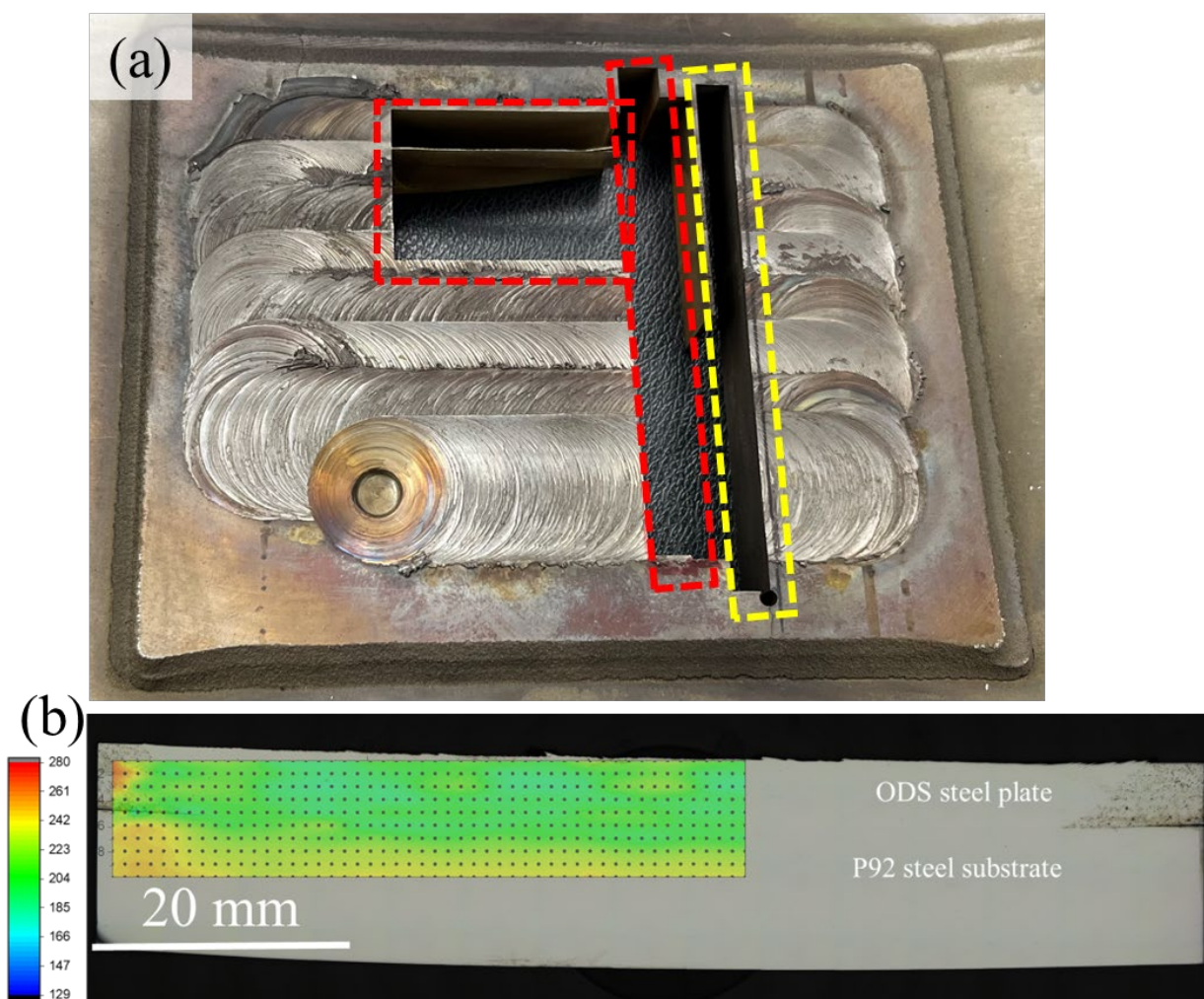


Figure 3. (a) The #2 plate after second iteration of cold spray and FSP. Cross section (yellow box) has been extracted from the plate for OM and hardness. Creep specimens were also extracted in two directions (red boxes). (b) The OM montage image of the plate cross section, with the ODS layer (~5 mm thick) on top, and P92 steel substrate below. At the left and right corners of the ODS layer, un-processed, slightly porous remnant cold spray structure can be seen. Hardness map of the ODS layer shows that the hardness is ~200 HV and very uniform across all the processed area.

Using the same cold spray + FSP workflow, ~1 mm layer of pure Ni powder was deposited on P92 steel substrate, followed by ~2 mm layer of GARS ODS steel powder. The P92 steel substrate is used in place of W-Ni-Fe heavy alloys for this preliminary study. The tungsten heavy alloys are a dual phase composite, consisting of W particles in Ni-based ductile matrix. In this preliminary study, Ni is used as interlayer. Since the heavy alloys contains Ni-based ductile phase, joining the Ni interlayer with the tungsten heavy alloys is expected more or less straightforward (though formation of precipitates cannot be ruled out without experimental evidence), thus P92 steel is used as surrogate substrate. The more critical joining is between the interlayer and the ODS steel. The composite layers were processed with 1 pass of FSP as an initial trial. Figure 4(a) shows the OM montage image of the cross section of the processed layers along with the P92 steel substrate. Note that the sample was etched to reveal fine details, especially at interfaces. The black dashed line approximately outlines the FSP processed zone. Outside the processed zone, both the ODS steel layer and the pure Ni layer show as-cold spray porous structure, as also evidenced by the occasional low-hardness spots in the hardness map in Figure 4(b). Inside the processed zone, the two

layers are mostly consolidated and uniform. However, at the interface between the two layers, especially on the left side (i.e., the “advancing side” of friction stir), there appears to be “inter-flow” of two materials. Such inter-flow is much less prominent at the interface between pure Ni and the substrate. This result suggests that the interlayer would need to be consolidated first with FSP, followed by deposition and consolidation of ODS steel layer, and with a shallower processing depth, to minimize the intermixing.

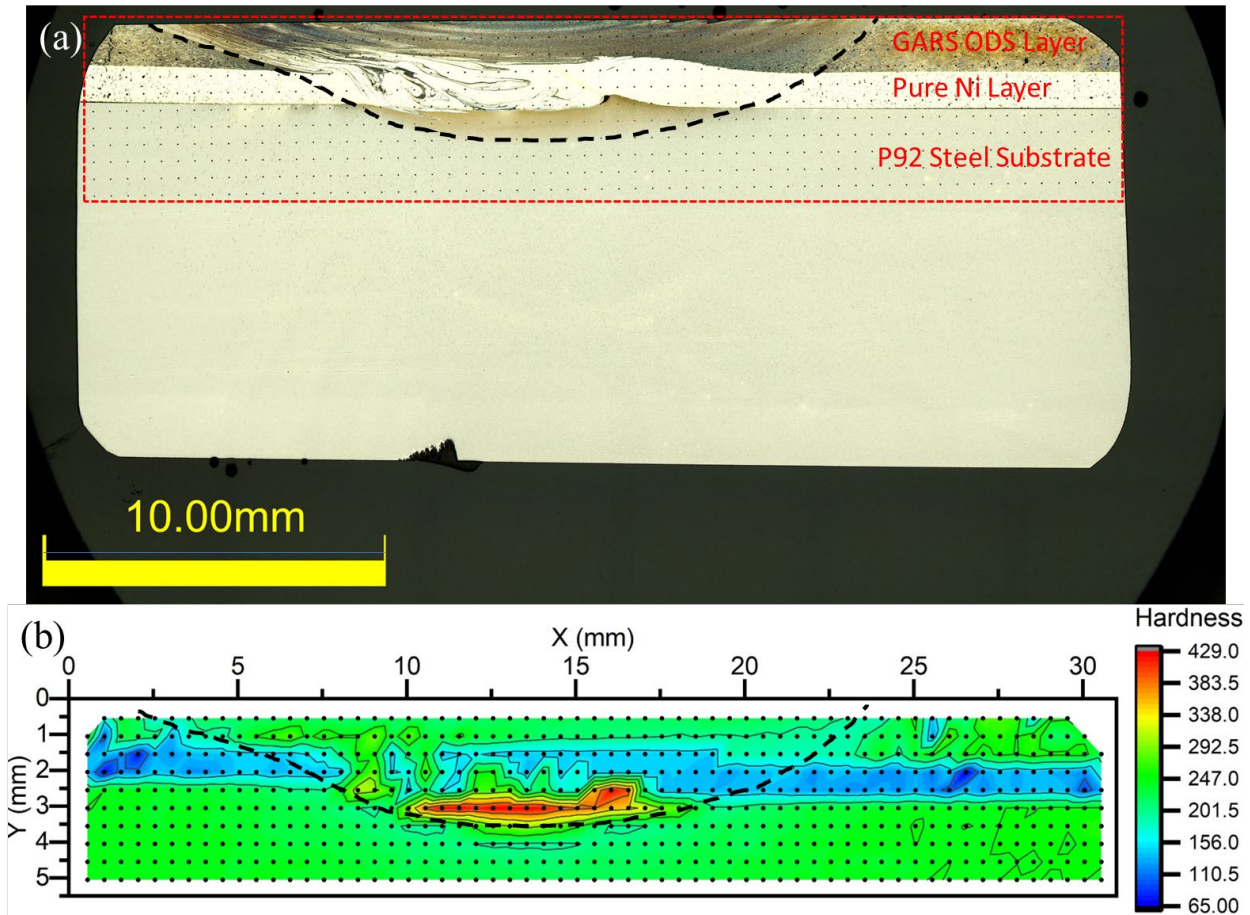


Figure 4. (a) An OM montage image of the cross-section of the FSP processed layers of pure Ni and GARS ODS steel along with the P92 steel substrate. (b) Hardness map of the highlighted portion of the sample.

To advance the scalable manufacturing of ODS steel plates, an innovative pathway was proposed via multi-passes CS and FSP. As illustrated in Figure 5 (a-e), the deposit was built up in two accumulative layers to show the additive capability of this approach. First, a large area (140 mm by 130 mm) CS deposition with a nominal thickness of 4 mm was made and machined to approximately 3.3 mm thick. The first layer was processed with FSP, resulting in a one-layer ODS steel plate (layer #1). Then layer #1 was recoated with CS to form a second deposition with a slightly smaller area (130 mm by 120 mm) and machined to approximately 2.5 mm thick, followed by a second FSP. The slight decrease in the thickness of the second layer allowed for some through thickness overlap between the two FSP layers. The FSP tool position-temperature plot was shown in Figure 5(f). Two iterations of CS+FSP were done here to demonstrate the feasibility towards fabricating thick plates. The final fabricated plate has dimensions of ~140 mm in length, ~130 mm in width, and ~6 mm in thickness, respectively (Figure 5(g)).

To reveal the structural homogeneity and detailed microstructure after two-passes of CS and FSP, Electron Backscatter Diffraction (EBSD) and EDS were employed to characterize the microstructures (layers # 1

and #2 marked in Figure 5(b)) in Figure 6. As shown in Figure 6a, a homogenous structure with equiaxed grains was formed and the average grain size is $\sim 2.78 \pm 0.93 \mu\text{m}$, with no visible cavity and pores detected in layer #1. Although some grains exhibited [101] preferred orientations, their fraction was very limited. The EDS maps in Figure 6(d) showed that Y-O oxide particles were homogeneously distributed around the grain boundaries and within the grains, indicating that most Y-Fe intermetallics have been transformed into oxides. Moreover, some Y-O particles have been developed into Y-Ti-O particles, as evidenced by the overlap of Ti with Y and O element maps (Figure 6(d)).

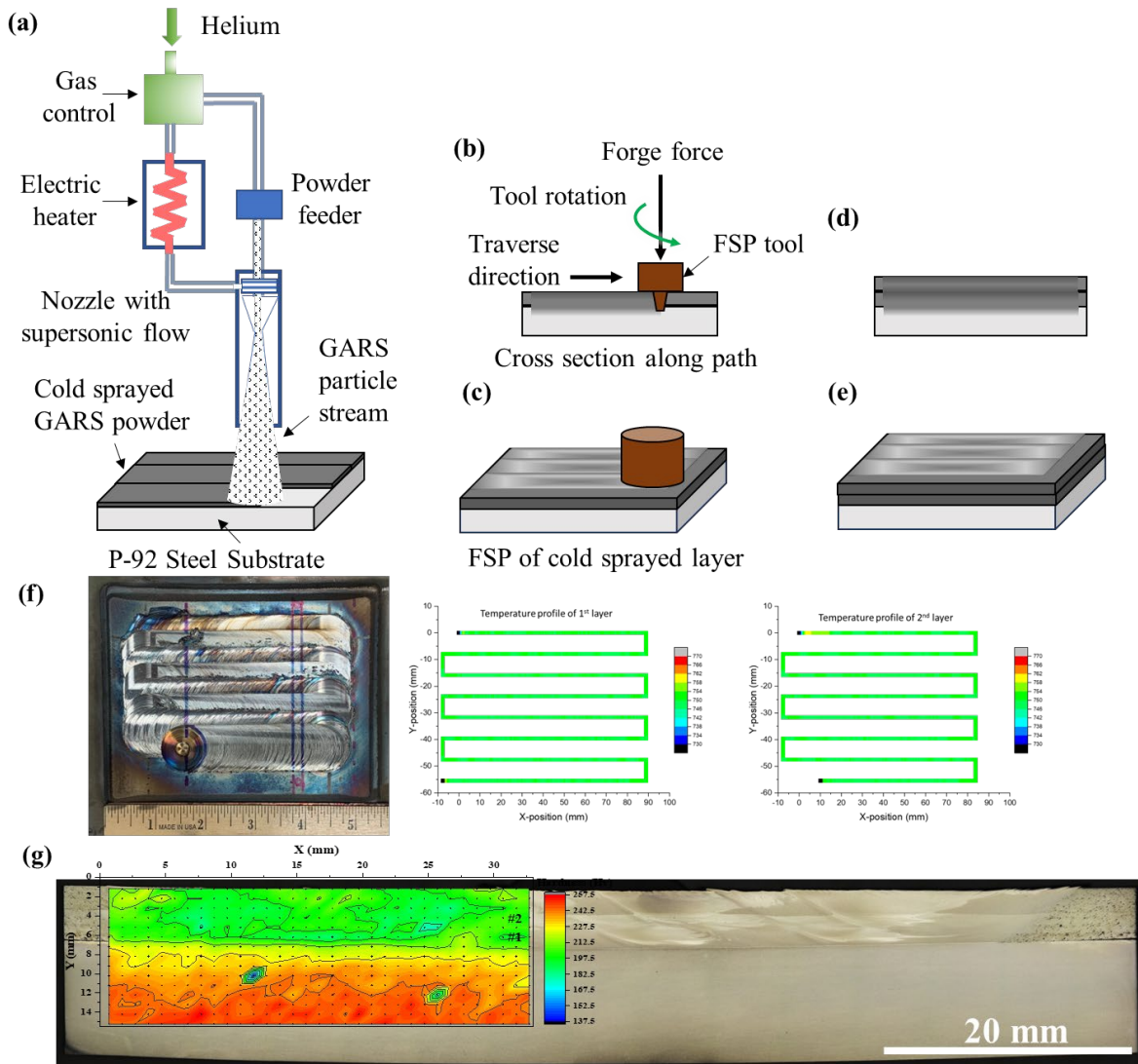


Figure 5. (a) Schematic of multi-passes cold spraying and friction stir processing. (a) The CS of GARS-synthesized powders onto P-92 steel plate. (b) Cross section of FSP of ODS steel plate. (c) The FSP rastering of cold sprayed layer. (d) Cross section of two iterations for CS followed by FSP. (e) Fabricated ODS steel plate on P-92 steel after two iterations of CS and FSP. (f) The tool raster pattern and the FSP tool position-temperature plot. (g) Fabricated large ODS steel plate. A hardness map of the half-plate is inserted.

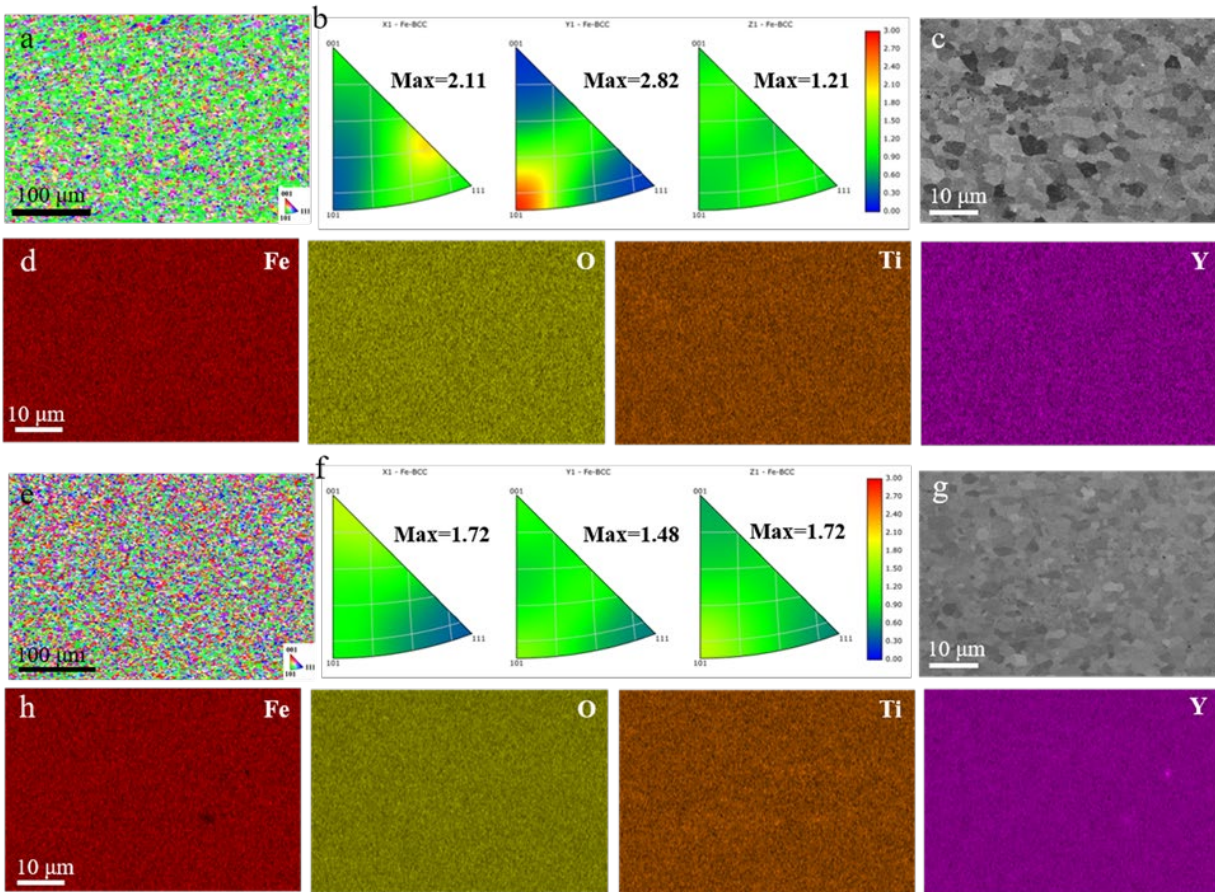


Figure 6. Microstructures of deposition layers 1 and 2 (selected positions #1 and #2 in the harness map of Figure 5). (a) The EBSD map of #1. (b) Inverse Pole Figure (IPF) of a. (c) The BSE image from #1. (d) The EDS maps of Fe, O, Ti, and Y for c. (e) The EBSD map of #2. (f) The IPF of e. (g) The BSE image from #2. (h) The EDS maps of Fe, O, Ti, and Y for g.

To explore the structural homogeneity between different passes/deposited layers, the microstructure of layer #2 was investigated. As shown in Figure 6(e), layer #2 presented an equiaxed-grain structure with an average grain size of $2.52 \pm 0.65 \mu\text{m}$. Similar to layer #1, it did not show any distinct texture, as proven by the IPF color map in Figure 6(f). The EDS maps showed a similar distribution of Y-O oxide particles with no agglomeration. These results verified the structure homogeneity and the capability of additive manufacturing-like production. To reveal the dispersion of oxide particles, atom probe tomography (APT) was employed, as shown in Figure 7. Three-dimensional (3D) ion (Fe, Cr, Y, Ti, O) maps demonstrated that Y-O and Y-Ti-O particles dominated the oxide types, with no significant presence of Cr-O and Ti-O particles. The presence of complex Y-Ti-O particles suggested that most Ti-O particles have been consumed in reactions with existing Y-O particles. The oxide particle number density, derived from the ion maps in Figure 7(a), is $\sim 2.2 \times 10^{22}/\text{m}^3$. Typical Y-O and Y-Ti-O particles were indicated by black and white triangles respectively in the ion maps. The elements of two selected particles (marked by A and B) were analyzed as shown by the histogram concentration profiles in Figure 7 (b) and (c), verifying the presence of two different particle types, i.e., Y-O and Y-Ti-O.

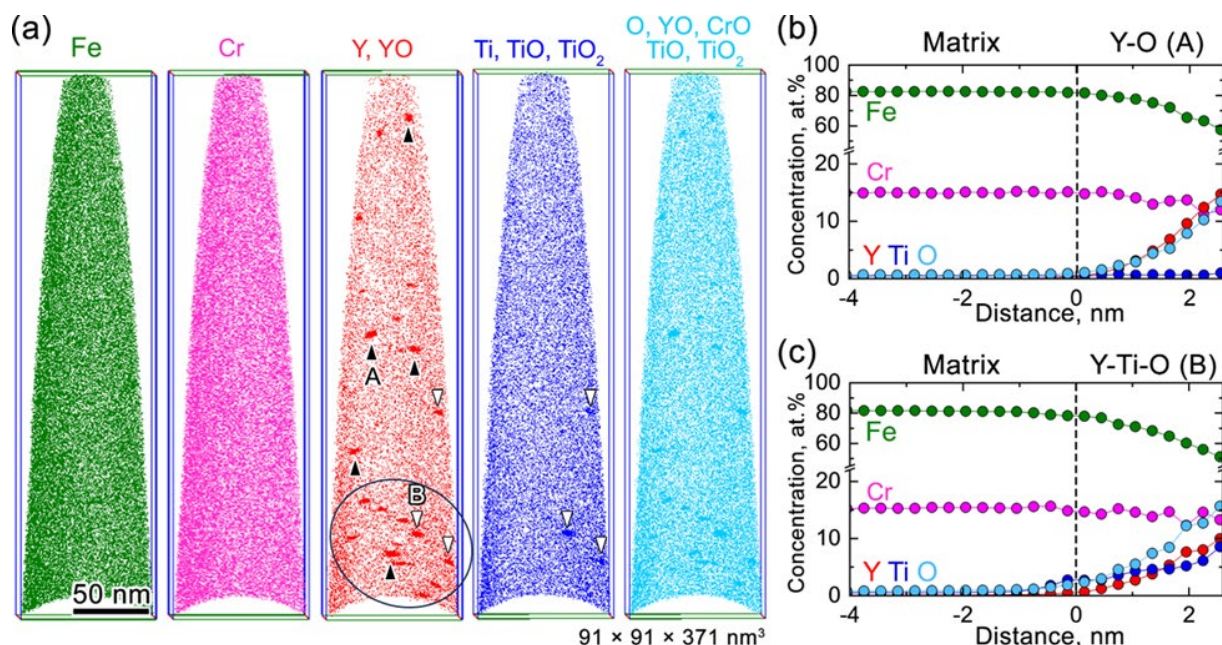


Figure 7. Nanoscale oxide particles in the fabricated ODS steel plate (site #2). (a) The 3D atom maps of Fe, Cr, Y, Ti, and O. (b) and (c) Proximity histogram concentration profiles across the matrix/oxide interfaces of A and B as indicated by arrows in (a).

Mechanical tests, including the tensile and creep tests, are summarized in Figure 8. Four tensile samples were extracted from the fabricated plate along both the FSP longitudinal and transverse directions. The corresponding tensile curves are shown in Figure 8(a). The samples along the FSP direction exhibited a 0.2% yield strength (YS) of ~ 477.5 MPa and an ultimate tensile strength (UTS) of ~ 655.5 MPa, which are higher than the corresponding values of ~ 402 MPa and ~ 617 MPa for the samples along the transverse direction. The uniform elongation (UE) was $\sim 18.5\%$, also higher than the 14% observed in the transverse direction. All samples' YS, UTS, UE, and total elongation (TE) were summarized in Table 1. The creep results from samples taken from the longitudinal and transverse directions tested at 650°C and 150 MPa, can be found in Figure 8(b). The creep rupture life of the longitudinal and transverse samples were 62 and 51 hours respectively. The specimen tested along the transverse direction initially strained further after loading (10% vs. 6%) but the overall strain at failure was lower than the longitudinal specimen (21% vs. 28%). These differences may be attributed to the slight structural heterogeneity along the transverse direction. Conclusively, the fabricated big plate showed excellent synergistic mechanical properties. These findings validate the feasibility of using additive-manufacturing-inspired techniques for large-scale ODS steel production and pave the way for substantial improvements in materials performance for fusion energy applications.

A manuscript reporting the results of this research has been submitted to Journal of Materials Engineering and Performance.

Future work will focus on the evaluation of the fracture toughness and further enhancement of structural uniformity and mechanical performances of fabricated ODS steel plates.

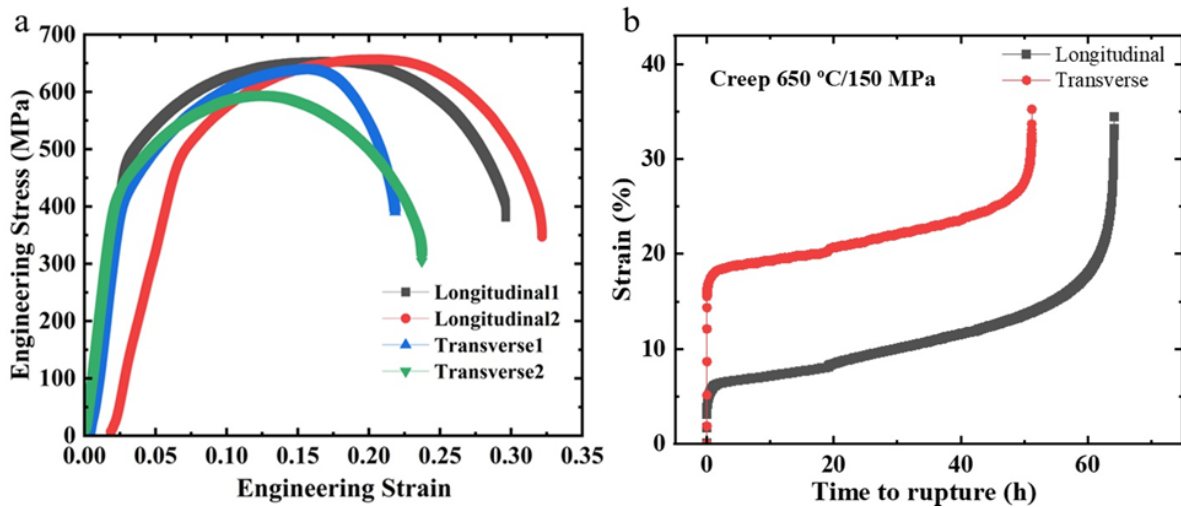


Figure 8. Mechanical properties of the fabricated ODS steel plate. (a) Tensile test. (b) Creep test.

Table 1. Summary of tensile properties of the fabricated ODS steel plate

Specimen #	0.2% offset YS (MPa)	UTS (MPa)	Uniform Elongation (%)	Total Elongation (%)
Longitudinal1	468	654	16.9	29.6
Longitudinal2	487	657	20.0	30.3
Transverse1	404	638	15.5	21.8
Transverse2	400	596	12.5	23.7

Acknowledgements

This research was supported by the U.S. Department of Energy (US DOE), Office of Science, Office of Fusion Energy Sciences, through Contract No. AT2030110-13784 and was performed at the Pacific Northwest National Laboratory, which is operated by Battelle for the US DOE under Contract No. DE-AC05-76RL0-1830. We are grateful to cold spray technical support provided by Chris Smith, Justin Olson, and Mark Rhodes.

References

- [1] M. Rieth, M. Dürrschnabel, S. Bonk, G. Pintsuk, G. Aiello, J. Henry, Y. de Carlan, B.E. Ghidersa, H. Neuberger, J. Rey, C. Zeile, N. De Wispelaere, E. Simondon, J. Hoffmann, Impact of materials technology on the breeding blanket design – Recent progress and case studies in materials technology, *Fusion Engineering and Design* 166 (2021) 112275.
- [2] J. Rieken, Gas atomized precursor alloy powder for oxide dispersion strengthened ferritic stainless steel, Ames Laboratory (AMES), Ames, IA (United States), 2011, p. 362.

2.2 COST-EFFECTIVE THERMOMECHANICAL PROCESSING OF NANOSTRUC-TURED FERRITIC ALLOYS: MICROSTRUCTURE AND MECHANICAL PROPERTIES INVESTIGATION—Y. Lin, T.S. Byun (Oak Ridge National Laboratory)

Extended Abstract: Full manuscript submitted to Materials

OBJECTIVE

The objective is to develop cost-effective manufacturing methods for producing nanostructured ferritic alloys (NFAs) with fine grains and high nanoparticle densities, incorporating the benefits of nanoparticle dispersion into ferritic alloys for fusion reactors.

SUMMARY

The NFAs, such as oxide-dispersion strengthened (ODS) alloys, play a vital role in advanced fission and fusion reactors, offering superior properties when incorporating nanoparticles under irradiation. Despite their importance, the high cost of mass-producing NFAs through mechanical milling presents a challenge. This study delves into the microstructure-mechanical property correlations of three NFAs produced using a novel, cost-effective approach combining severe plastic deformation (SPD) with continuous thermomechanical processing (CTMP) method. Analysis using scanning electron microscopy (SEM)-electron backscatter Diffraction (EBSD) revealed nano-grain structures and phases, while scanning transmission electron microscopy (STEM)- energy dispersive X-ray spectroscopy (EDS) quantified the size and density of Ti-N, Y-O, and Cr-O fine particles. Atom probe tomography (APT) further confirmed the absence of finer Y-O particles and characterized the chemical composition of the particles, suggesting possible nitride dispersion strengthening. Mechanical testing demonstrated that the CTMP alloys exhibit strength and ductility comparable to mechanically milled ODS alloys. Although mechanically milled 14YWT ODS alloys showed finer nanoparticles and higher densities, the CTMP NFAs present a promising avenue with their cost-effective production and potential radiation resistance. Further enhancements in uniform nanoparticle distribution and increased sink strength are recommended to mitigate cavity swelling, advancing their suitability for nuclear applications.

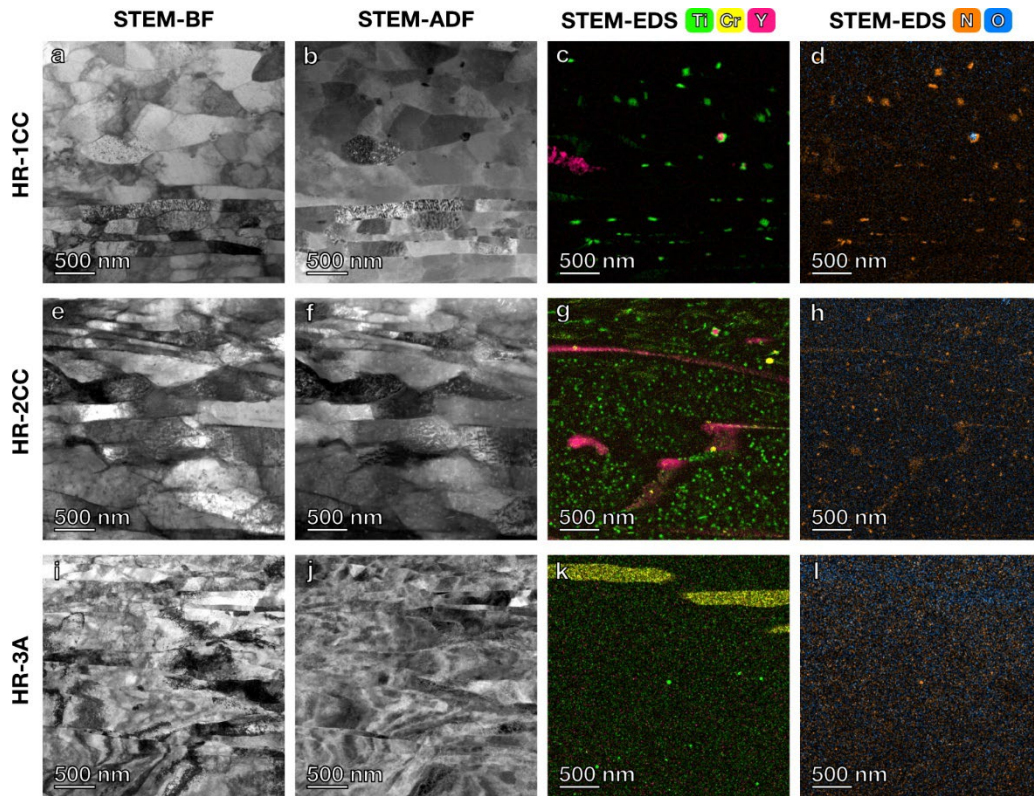


Figure 1. The STEM bright-field (BF) and annular dark-field (ADF) images with corresponding EDS elemental maps for: (a-d) HR-1CC (14YWT powder only), (e-h) HR-2CC (14YWT powder + Fe_2O_3), and (i-l) HR-3A (14YWT powder + Y_2O_3) alloys.

Results

Future work will focus on optimizing the CTMP process, including reducing grain size, improving homogeneity, increasing the density of fine particles, and elucidating the mechanisms behind oxide and nitride formation.

3. CERAMIC COMPOSITE STRUCTURAL MATERIAL DEVELOPMENT

3.1 EMERGING CONTINUOUS SiC FIBERS FOR HIGH-TEMPERATURE APPLICATIONS—H. Gietl (Idaho National Laboratory), O. Karakoc, S. Harrison (Free Form Fibers), T. Koyanagi, Y. Katoh (Oak Ridge National Laboratory)

Abstract of a manuscript in Ceramics International (<https://doi.org/10.1016/j.ceramint.2024.06.100>)

Silicon carbide (SiC) fibers are responsible for the ultimate strength and toughness of SiC-fiber reinforced composites in harsh environments. The development of a new generation of continuous SiC fibers continues to advance the mechanical properties of composite materials. Tyranno™ SA4 fiber was recently released as a successor of Tyranno™ SA3 fiber. Laser-driven chemical vapor deposition (LCVD) has been adopted as an alternative fiber processing route to synthesizing high-strength SiC fiber with tailorable small diameters and chemical compositions. Both Tyranno™ SA4 and laser-driven CVD fibers show very high tensile strength, about 4 GPa in the as-fabricated condition. The degradation of thermal stability and strength due to annealing in an inert environment were similar for Tyranno™ SA3 and SA4 fibers because of their similar carbon-rich, crystalline microstructure. Silicon-rich fibers produced by LCVD possessed heterogeneous crystallinity, which was attributed to laser power distribution and showed microstructural instability at 1500°C and above. The new SiC fibers demonstrated an increase in as-fabricated strength but faced the same challenges in environmental resistance as the traditional SiC fibers do.

4. PLASMA-FACING AND HIGH HEAT FLUX MATERIALS AND COMPONENT TESTING

4.1 MICROSTRUCTURAL FEATURES IN DUCTILE-PHASE-TOUGHENED TUNGSTEN IRRADIATED INDIVIDUALLY WITH Ni²⁺ AND He⁺ IONS AT 1,000°C

—W. Jiang, J. V. Haag IV, L. Kovarik, B. Matthews, W. Setyawan (Pacific Northwest National Laboratory), D. Chen (University of Houston)

OBJECTIVE

This study aims to elucidate the microstructural features in ductile-phase-toughened tungsten sequentially irradiated with Ni²⁺ and He⁺ ions at 1,000°C by performing individual ion irradiations.

SUMMARY

Previous investigations reported that 87R DPT W sequentially irradiated with Ni²⁺ and He⁺ ions at 1,000°C displayed a microstructure with small cavities and solid precipitates in the W phase, larger cavities at the interphase boundary, and no features in the NiFeW phase. To better understand this complex microstructure, we prepared two focused ion beam (FIB) samples from 87R DPT W irradiated individually with Ni²⁺ and He⁺ ions at 1,000°C. The results show that precipitate formation in the W phase is solely due to Ni²⁺ irradiation, while cavity formation in W is caused exclusively by He⁺ ion irradiation. Both irradiations contribute to the cavity population at the interphase boundary. Additionally, thermal annealing of room temperature (RT) irradiated 87R DPT W at 1,000°C was performed, and the annealed sample was examined using transmission electron microscopy (TEM). The microstructure resembles that of the sample irradiated directly at 1,000°C, though with slightly smaller cavities and higher number density. A manuscript detailing the findings is currently in preparation.

PROGRESS AND STATUS

Introduction

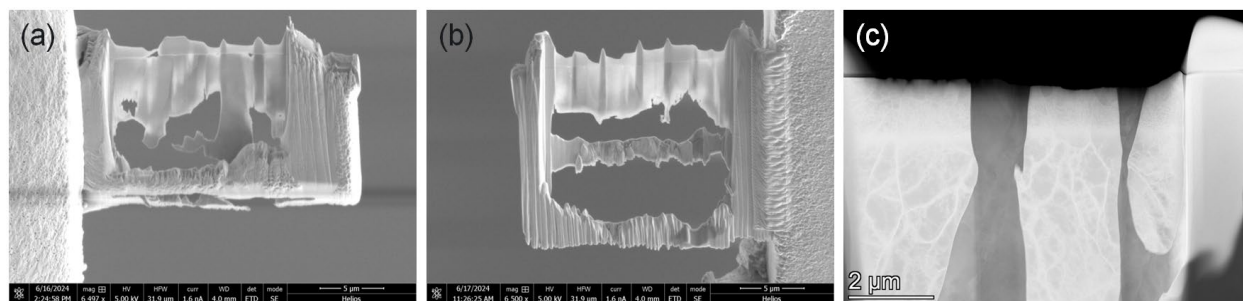


Figure 1. The FIB samples for 87R DPT W irradiated at 1,000°C with (a) Ni²⁺ ions, (b) He⁺ ions, and at RT with (c) Ni²⁺ and He⁺ ions.

To better understand the microstructural features in 87R DPT W irradiated at 1000°C to 3.0×10^{16} Ni²⁺/cm² and 1.3×10^{16} He⁺/cm² [1], we prepared two new FIB samples from individual irradiations with Ni²⁺ and He⁺ ions at the same ion fluences and temperature using a Thermo Fisher G4 Hydra plasma focused ion beam (PFIB) dual-beam microscope. Figures 1(a) and (b) show sample images for Ni²⁺ and He⁺ ion irradiations, respectively. The depth of interest ranged from 500 to 1,000 nm based on Stopping and Range of Ions in Matter (SRIM) simulations [2]. Regions containing NiFeW and W interphases were selected and capped with ~500 nm of e-beam-deposited W and 3 µm of W deposited using a Xe ion beam. The W was preferred over the usual Pt due to its higher resistance to ion sputtering, which helps preserve the sample surface. A lamella was then extracted and attached to a Cu grid using a standard lift-out procedure. For better lamella thinning with a precise Ga⁺ ion beam, a Field Electron and Ion Company (FEI) Helios 600 Nanolab dual-beam FIB microscope was employed. The thinning process began at a low tilt ($\pm 1.5^\circ$ from 52°) using the Ga⁺ ion beam at 30 kV. When the sample reached ~200 nm in thickness,

the tilt was adjusted to 54-55° ($\pm 2-3^\circ$ from 52°), and the beam energy was reduced to 5 kV for final thinning. To ensure even thinning, W regions were targeted with a double pattern, given a lower sputtering rate of W compared to NiFeW. When the lamella became electron-transparent at 5 keV (thickness <100 nm), it was further tilted to 57° ($\pm 5^\circ$ from 52°) and polished at 2 kV. The FIB sample of 87R DPT W sequentially irradiated with Ni²⁺ and He⁺ ions at RT, shown in Figure 1(c), underwent additional milling with Ar⁺ ions to remove surface damage and oxide layers, crucial for identifying small microstructural features. This ion milling was performed on both cross-sectional surfaces at 900 eV for 30 min, followed by further polishing of both sides at 500 eV for 30 min.

The FIB samples were examined using a probe aberration-corrected Thermo Fisher Scientific Themis Scanning transmission electron microscope (STEM) microscope with a spatial resolution of 0.05 nm. Both high-angle annular dark-field (HAADF) STEM and conventional bright-field (BF) TEM were conducted at an accelerating voltage of 300 kV. Data analysis was carried out using the Gatan Microscopy Suite 3. Additionally, Fresnel defocusing techniques were employed to observe cavities in the irradiated samples.

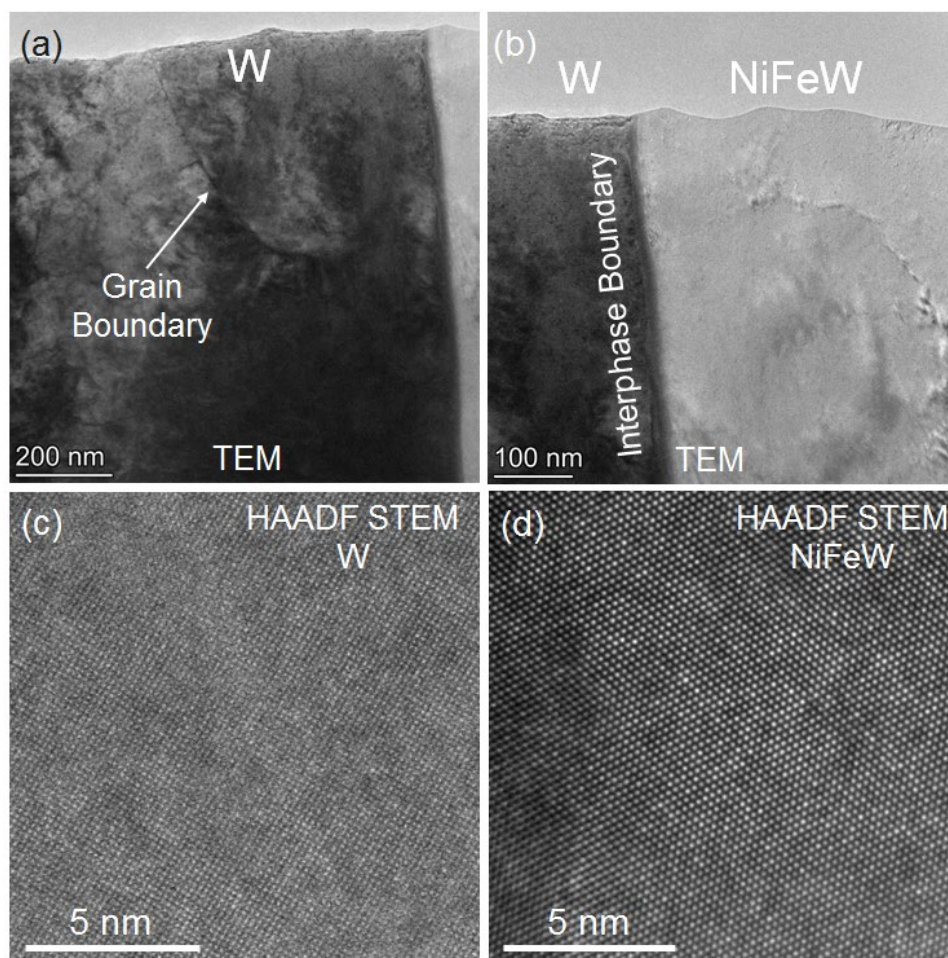


Figure 2. (a) Microstructures of (a) the W phase and (b) NiFeW phase with an interphase boundary in 87R DPT W sequentially irradiated to 3.0×10^{16} Ni²⁺/cm² and 1.3×10^{16} He⁺/cm² at RT. Atomic resolution images of (c) W at the image center depth of 430 nm and (d) NiFeW at 310 nm in the irradiated area.

The microstructure of 87R DPT W irradiated sequentially with Ni²⁺ and He⁺ ions at RT is shown in Figure 2 at various magnifications. A high density of black spots, indicative of small dislocation loops, is

observed in the irradiated depth region of the W phase [Figure 2(a)]. No discernable cavities or precipitates are detected in the grain interior or boundary of the W phase [Figure 2(a)], the NiFeW phase, or the interphase boundary [Figure 2(b)]. Atomic-level resolution images in Figures 2(c) and (d) show some dark contrast in W and NiFeW phases in the near-surface region, suggesting lattice damage that may include He-vacancy clusters in both W and NiFeW phases. Preliminary results [1] suggested some microstructural features in W and at the interphase boundary, but after ion milling of the FIB sample, those features disappeared, indicating they were likely artificial surface defects rather than irradiation-induced cavities.

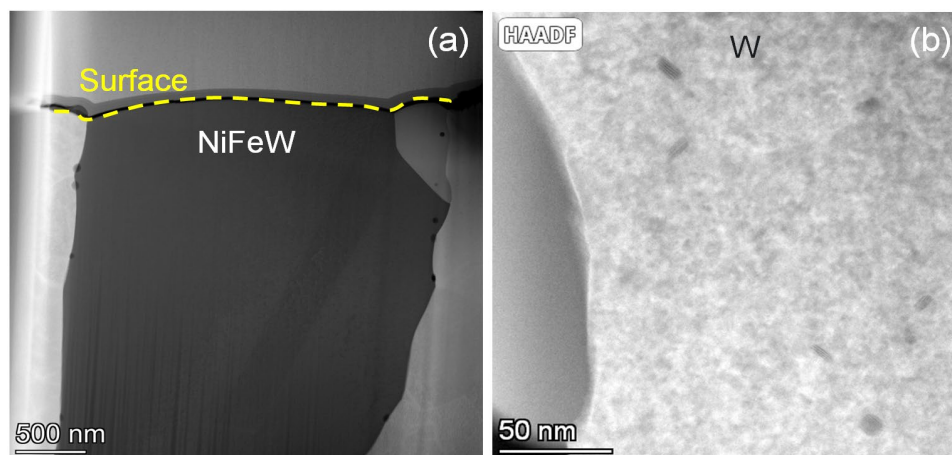


Figure 3. The HAADF STEM images of the microstructure (a) near the surface and (b) at the image center depth of 550 nm in 87R DPT W irradiated to 3.0×10^{16} Ni²⁺/cm² at 1,000°C.

A general view of the cross-sectional microstructure of 87R DPT W after Ni²⁺ ion irradiation at 1,000°C is shown in Figure 3(a). The top is a tungsten layer deposited for sample surface protection during FIB processes. Round cavities, ~50 nm in size and low in number density, are observed at the interphase boundary within the depth range of 250 nm to 1.2 μm. Small precipitates inside the W phase are also present, as shown in Figure 3(b). These features are confirmed by Energy-Dispersive Spectroscopy (EDS) mapping (data not shown). The composition of the precipitates is approximately 26 at.% Ni, 13 at.% Fe, and 61 at.% W. Moreover, STEM provides no evidence of void formation in the interior of either W or NiFeW phase.

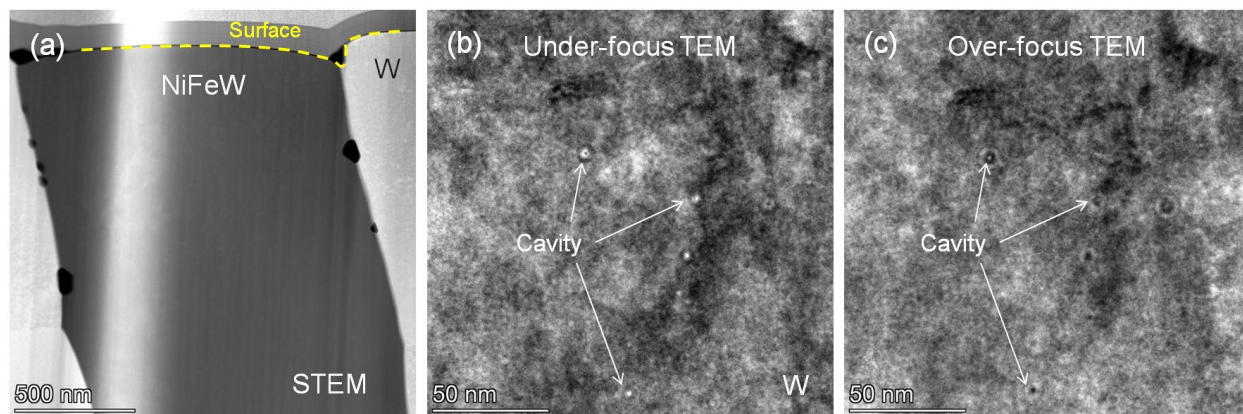


Figure 4. (a) A HAADF STEM image of the microstructure near the surface of 87R DPT W irradiated to 1.3×10^{16} He⁺/cm² at 1,000°C. (b) Under-focus and (c) over-focus TEM images showing the formation of cavities in the interior of W at the image center depth of 570 nm.

Figure 4(a) shows a STEM view of 87R DPT W irradiated with He⁺ ions at 1,000°C. The image exhibits large cavities formed at the interface boundaries. The size of these cavities ranges from 25 to 110 nm, distributing from 180 nm to 1 μm in depth. The vertical contrast band in Figure 4(a) indicates a thicker region in NiFeW due to FIB polishing effects. No evidence for the formation of solid precipitates was found in the sample. To confirm cavity formation in W, defocusing TEM examinations of the W interior at a depth of ~570 nm were conducted. Figures 4(a) and (b) show TEM images under under-focus and over-focus conditions, respectively. Bright features under under-focus reverse to dark under over-focus, as indicated by arrows in Figures 4(b) and (c), suggesting that these features are cavities in the W phase. The corrected cavity size is ~4 nm, comparable to that (3.8 nm) observed in 87R DPT W irradiated sequentially with Ni²⁺ and He⁺ ions at 1,000°C. This result is also consistent with a previous study [3] that reported the mean cavity size of ~4 nm in pure W irradiated with He⁺ ions to a comparable He fluence at 1,000°C. That study [3] also found that an increase in the He⁺ ion fluence at 1,000°C led to a higher cavity number density with minimal impact on cavity size.

Results

Data acquisition for 87R DPT W irradiated with Ni²⁺ and He⁺ ions at RT and 1000°C is complete, and most data analysis is also finished. Figures and tables are being prepared for a manuscript currently in draft.

Acknowledgements

This research was supported by the U.S. Department of Energy (US DOE), Office of Science, Office of Fusion Energy Sciences, through Contract No. AT2030110-13784 and was performed at the Pacific Northwest National Laboratory, which is operated by Battelle for the US DOE under Contract No. DE-AC05-76RLO-1830. Ion irradiation experiment was performed at the University of Houston.

References

- [1] W. Jiang, J.V. Haag IV, B.E. Matthews, W. Setyawan, D. Chen, Fusion Materials Semiannual Progress Report for Period Ending December 31, 2023, DOE/ER-0313/75, U.S. Department of Energy, p.63.
- [2] W. Jiang, J.V. Haag IV, W. Setyawan, D. Chen, Fusion Materials Semiannual Progress Report for Period Ending June 30, 2023, DOE/ER-0313/74, U.S. Department of Energy, p.93.
- [3] X. Yi, K. Arakawa, D. Nguyen-Manh, F. Ferroni, P. Liu, W. Han, *et al.*, Fusion Eng. Des. 125 (2017) 454.

4.2 SIMULTANEOUS EXPOSURE OF FUSION MATERIALS TO NEUTRON IRRADIATION AND HYDROGEN ENVIRONMENT—W. Zhong, T. Koyanagi, Y. Katoh (Oak Ridge National Laboratory), Y. Hatano (University of Toyama)

OBJECTIVE

Novel irradiation capsules containing vanadium hydride were designed and irradiated in the High Flux Isotope Reactor (HFIR) to create a hydrogen gas environment during neutron irradiation. The objective of this work is to characterize the hydrogen environment inside the capsule through post-irradiation examination of the vanadium and vanadium hydride samples.

SUMMARY

Two irradiation capsules were irradiated and are investigated in this work. One capsule (VH01) containing vanadium hydride, whereas the other capsule (VNH1) containing only vanadium metal, serving as a reference. Thermal desorption spectroscopy (TDS) experiment was performed on the vanadium metal from both capsules. The results confirmed hydrogen absorption by the vanadium metal in the VH01 capsule, consistent with the observed reduction in hydrogen content in the vanadium hydride. These findings highlight the successful generation of a hydrogen environment during irradiation and provide valuable data on hydrogen behavior in irradiated materials. This activity is a part of the FRONTIER project collaboration.

PROGRESS AND STATUS

Introduction

Two irradiation capsules were irradiated in HFIR and are investigated in this work. One capsule (VH01) contained vanadium hydride to create hydrogen gas environment during irradiation, and the other capsule (VNH1) contained only vanadium metals, serving as a reference to study the irradiation effects without hydrogen influence. Both capsules were inserted in the hydraulics tubes of HFIR for about 31.5 hours with the fast neutron fluence ($E > 0.1$ MeV) of $\sim 1.1 \times 10^{20}$ n/cm².

Thin specimens of metallic vanadium were included in both VH01 and VNH1 capsules for irradiation. These specimens were tested using TDS to investigate their hydrogen absorption during irradiation. Figure 1 shows the thermal desorption spectroscopy results for vanadium in both capsules. Small amount of the hydrogen release was observed in the VNH1 capsule, which may result from the (n, p) reaction in vanadium or the corrosion of capsule with the reactor coolant. On the other hand, significant hydrogen release was observed in the vanadium sample in the VH01 capsule, indicating significant hydrogen absorption by vanadium in the capsule. The TDS experiment was stopped at ~ 330 °C due to the high hydrogen build-up. These results confirm the presence of a hydrogen environment within the VH01 capsule during irradiation, demonstrating that samples in the VH01 capsule were concurrently exposed to both neutron irradiation and a hydrogen-rich atmosphere.

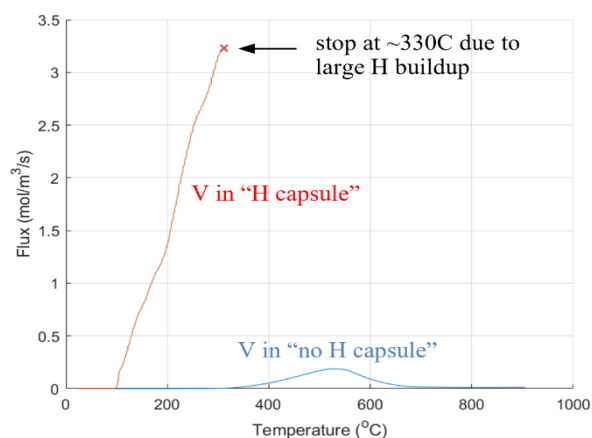


Figure 1. Thermal desorption spectroscopy results for metallic vanadium in both VH01 and VNH1 capsules. Significant hydrogen release was observed in vanadium in VH01 capsule indicating hydrogen absorption during irradiation in Vanadium in VH01 capsules.

Pressure-composition isotherm measurements were performed on irradiated and unirradiated vanadium hydride in a vacuum chamber of known chamber volume. Figure 2 shows the measured pressure as a function of time (including temperature ramping and holding). Samples were inserted in a quartz tube. Pressure was monitored during the temperature ramping and the holding at 400°C. Obvious desorption for unirradiated VH starts at 400°C, whereas slight earlier desorption was observed after irradiation. The final pressure was determined when the pressure is stable at least for 5 minutes. The equilibrium pressure for unirradiated and irradiated VH are determined as 12.1 Torr and 7.2 Torr respectively. The reduced equilibrium pressure of VH after irradiation verifies the hydrogen release from VH during irradiation, which created hydrogen environment in the irradiation capsule during irradiation. This is consistent with the observation of hydrogen absorption in metallic vanadium shown in Figure 1. In addition, both unirradiated and irradiated vanadium hydride reach equilibrium pressure within 30 minutes, which is much shorter than the irradiation time (31.5 hours), supporting that vanadium hydride may also achieve equilibrium during the irradiation.

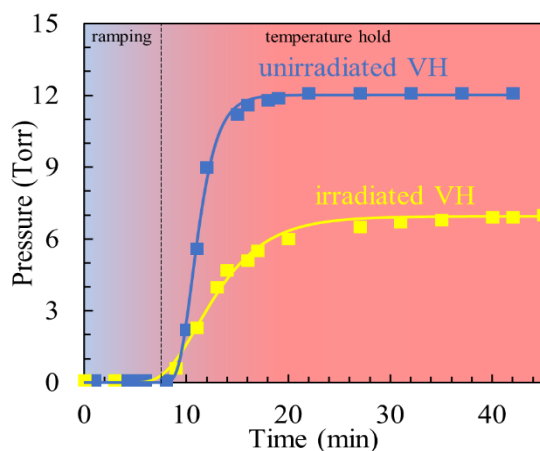


Figure 2. Pressure as a function of annealing time for unirradiated and irradiated VH.

Results

Hydrogen retention and desorption properties of the fusion materials in the VH01 capsules will be characterized.

4.3 ANNEALING AND ELEVATED TEMPERATURE TENSILE STUDIES ON W/NiFe DUCTILE-PHASE TOUGHENED W COMPOSITES—R. Prabhakaran, W. Setyawan (Pacific Northwest National Laboratory)

OBJECTIVE

The objective of this task is to investigate the high-temperature operating limit of W/NiFe ductile-phase toughened (DPT) W composites and to explore how hot-rolling may improve the high-temperature tensile and fracture toughness.

SUMMARY

This report summarizes the recent annealing studies and mechanical test results obtained by conducting tensile testing of DPT W-NiFe specimens at room and elevated temperatures.

PROGRESS AND STATUS

Introduction

Tungsten is a promising candidate material for plasma-facing components (PFCs) due to its excellent high-temperature strength, low sputtering rate, good thermal conductivity, and high melting temperature. [1-2] However, the potential application of tungsten as a structural material in PFCs is limited due to its low ductility which will further degrade after irradiation. [3] Therefore, introducing a DP to develop a tungsten composite could serve as an alternative route to overcome its limitations. The DPT is a fracture toughness improvement concept that is being utilized to develop tungsten-based composites for fusion reactor divertor and plasma-facing materials. Liquid-phase sintered tungsten heavy metal alloys (WHAs), due to their balance of strength, ductility and toughness, are being considered to be a suitable alternative to monolithic polycrystalline tungsten (W) for fusion applications.

The low melting point of the alloying elements Fe and Ni being 1538°C and 1455°C, respectively, could restrict the operational space. However, to avoid recrystallisation of tungsten and to preserve its original mechanical properties, the temperature should be kept anyway below 1300°C, which means that the improvement in ductility and toughness by using Fe and Ni remains expected, though to a lesser extent compared to room-temperature mechanical property improvement. [4] Determining the mechanical properties of DPT-W at elevated temperatures is indeed an important aim of this research.

As per the literature, the maximum service temperature for divertors is likely 1200-1300°C [4-6], and hence it is critical to obtain the elevated temperature mechanical properties of WHA. The issue of W fuzz has not been fully resolved and, if significant, it might lower the maximum temperature to about 700°C. [7-9] The melting temperature of the DP phase (near Ni:Fe weight ratio of 7:3) is ~1440°C.

We have previously conducted tensile tests on as sintered 90W (purchased powders from MiTech; sintered at Pacific Northwest National Laboratory [PNNL]), 95W (two batches: MiTech and Plansee), 97W (two batches: MiTech and Plansee), and 90W-87R rolled materials (sintered at PNNL) using an Instron 5582 servo-mechanical test frame equipped with Epsilon ONE optical extensometer. [10,11] Recently, room temperature tensile testing was conducted using an Instron 8801 servo hydraulic test frame on as sintered 90W, 95W and 97W samples (MiTech), and the results showed that the 0.2% offset yield strength (YS) values were similar for all samples, and it was slightly lower for 97W. However, the ultimate tensile strength (UTS) increased significantly as W% reduced. There was no significant difference between uniform and total elongations for a particular %W, and these values (UE and TE) increased significantly as W% reduced (i.e., as the percent of ductile phase increased), as expected. Additional details can be found in our previous report. [12]

Different thermomechanical plastic deformation processing routes, such as hot-rolling (HR), extrusion and swaging, can increase the strength of WHAs. [13-19] We have characterized the effects of the composite

architecture on deep notch bend bar toughness for a 90 wt.% W–Fe–Ni WHA, hot rolled to different thickness reductions of 62, 74 and 87%. [20] As per our previous study, the deformed W and DP phases that form a ‘brick-and-mortar (BAM)’ like microstructure could improve strength by hot working, while enhancing the ductility and toughness, by creating a more distributed damage zone under deep notch bar loading. [20-21]

During 2022, HR was performed on the sintered 90 wt.% W–Fe–Ni alloy (size: ~ 1” thick x 1” wide x 2.25” long pieces) procured from MiTech (HD 17D; Lot # 36124). Hot rolled plates with different thickness reductions (57R, 78R and 86R) were successfully fabricated. Additional information about 2022 HR operations can be found in the previous report. [12] Tensile test samples were obtained from these 90W hot rolled plates (57R, 78R and 86R). Room temperature tensile testing was performed on 90W hot rolled samples and the results showed that as the rolling reduction was increased from 0R→57R→78R→86R, the YS and UTS increased along with it. The difference between the uniform and total elongation gradually improved as the rolling reduction was increased. In addition, both UE and TE increased (more significant at 57R and 86R) as the rolling reduction was increased. Additional details can be found in our previous report. [12]

During 2023, HR was performed on the sintered 90 wt.% W–Fe–Ni alloy (~1” thick x 1” wide x 2” long pieces) procured from MiTech (HD 17D; Lot # 36124) and obtained hot rolled plates with two different thickness reductions: 66R (3:1 aspect ratio) and 83R (6:1 aspect ratio). Based on our studies, it appears that hot rolling at 1150/900°C combination at a 10% reduction per pass (to get plates with 66R and 83R total reductions) seems optimal for a 1” starting thickness. However, the thickness of hot rolled plates with total reductions of 66R and 83R obtained from 1” blocks were about 0.35” and 0.17”, and these are inadequate to prepare mechanical test specimens on the thickness side. Hence, efforts were also made to perform HR on sintered alloy with a larger starting thickness (~2” thick x 2” wide x 2” long pieces). The thicknesses of hot rolled plates with total reductions of 66R and 83R obtained from 2” blocks are about 0.71” and 0.36”, and these are adequate to prepare mechanical test specimens on the thickness side. Additional information about these HR studies can be found in our previous report [22].

In the past, researchers have performed heat treatment on WHA to improve the mechanical properties, especially the ductility and fracture toughness. [23-25] Annealing could help to homogenize the microstructure and heal processing damage, which is also an issue for the toughness properties of material in the as sintered condition. [24,26] We recently performed 1300°C annealing studies on a limited number of samples obtained from 90W-0R (MiTech) and 90W-86R (rolled at PNNL) for three different time periods (6, 12 and 24 hours) and evaluated its effect on the mechanical properties and microstructure, and the results could be found in our previous report. [22,27] The UTS values increased slightly for all durations. Annealing increased both UE and TE significantly irrespective of the duration. Our previous work also showed that it is necessary to perform additional annealing studies at different time periods (1.5, 3, 6, 12 and 24 hours) and then perform tensile testing of 90W-0R samples to get better statistics and to determine the optimum annealing time. [22,27]

Currently, efforts are ongoing to understand the mechanical behavior of DPT W–NiFe alloys (as sintered and rolled samples) at elevated temperatures: 245°C (0.3T_m); 418°C (0.4T_m), 591°C (0.5T_m), 764°C (0.6T_m) and 937°C (0.7T_m), where T_m is the melting temperature of nickel (1728K; 1455°C). This report is focused in documenting the recent comprehensive annealing studies on as sintered 90W-0R and 95W-0R, and elevated temperature tensile test studies of annealed 95W-0R at PNNL.

Experimental Procedure

Procurement of W–Fe–Ni alloys

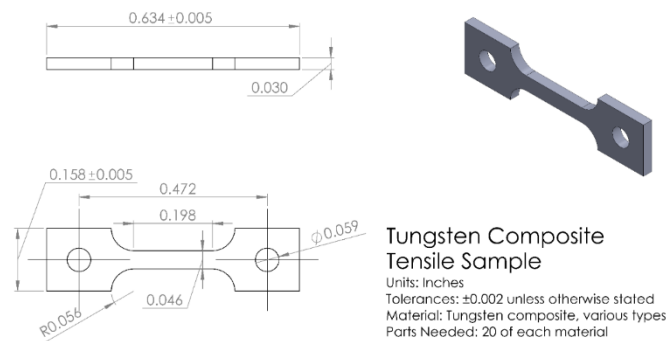
Sintered 90, and 95 weight % alloys were procured from MiTech to perform the annealing studies and mechanical testing at room and elevated temperatures. Table 1 shows the lot information of the WHA alloys.

Table 1. Sintered W-Ni-Fe alloys procured from MiTech

Material	Vendor	Vendor Code	Lot Number	Lot Chemistry (wt.%)
90W	MiTech	HD 17D	36124	90.37 W; 6.82 Ni and 2.81 Fe
95W	MiTech	HD 18D	36843	95.11 W; 3.45 Ni and 1.44 Fe

Tensile specimen fabrication

Sub-size tensile specimens, as shown in Figure 1, were machined (single orientation) using an electrical discharge machining (EDM) from as sintered 90W and 95W samples. Tensile specimens were fabricated to perform annealing studies and tensile testing at room and elevated temperatures. The nominal gage width, gage thickness and reduced length of a sub-size tensile specimen are 1.684 mm, 0.762 mm, and 5.029 mm, respectively. The total length and shoulder width of the sub-size tensile specimen are 16.104 mm and 4.013 mm, respectively.

**Figure 1.** Subsize tensile specimen design.

Annealing (1300°C) of DPT W-NiFe alloys

The PNNL has a Materials Research Furnaces, Inc. (MRF) Model M-4x6-M-1600-V&G front-loading furnace with a usable work zone of 3.5" diameter x 4.0" high, and a maximum operating temperature of 1600°C. The hot zone is a 180° split design with tungsten mesh heating elements for operation in vacuum (50-100 milliTorr) and inert gas (Ar, N₂ or Ar/O₂ gas mixture). Additional information about this furnace can be found in previous reports. [28,29]

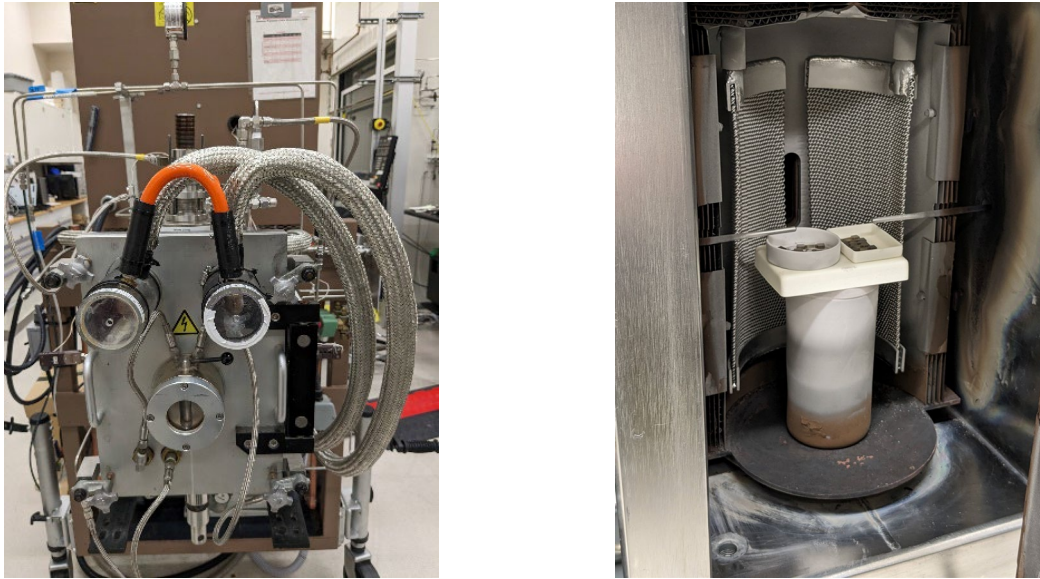


Figure 2. The MRF furnace (1600°C); Left: Exterior; Right: Interior – samples for annealing studies.

The MRF furnace was utilized for performing elevated temperature annealing studies on as sintered 90W-0R and 95W-0R tensile samples (fabricated using EDM) at 1300°C (under 5-10 milliTorr vacuum) for five different annealing times (1.5, 3, 6, 12 and 24 hours). Prior to annealing, the EDM recast layer (a few microns) were removed by gentle grinding. The melting temperatures of W, Ni and Fe are 3422°C, 1455°C and 1535°C, respectively and it is essential to consider the vapor pressure chart for various metals.

Two alumina crucibles were utilized for the annealing study. The alumina crucibles were positioned in such a way that it is at the center of the heat zone, as shown in Figure 2. Tensile specimens (see Figure 1) were placed inside the alumina crucibles. Once the samples were placed inside, the furnace door was closed, and the roughing pump was turned on until the vacuum levels reached 5-10 milliTorr. The temperature of the MRF furnace was gradually increased at a ramp rate of 3-5°C/min until it reached 1300°C. The samples were then annealed for a particular annealing time and then the furnace hot zone was shut down so that the samples can cool down via natural cooling. The furnace does not have any other cooling system. The vacuum level was maintained until the samples reached the ambient temperature. Figure 3 shows the typical condition of the tensile samples before and after 1300°C annealing. Annealing could help to homogenize the microstructure and heal processing damage, which is also an issue for the toughness properties of material in the as sintered condition. [24,26]

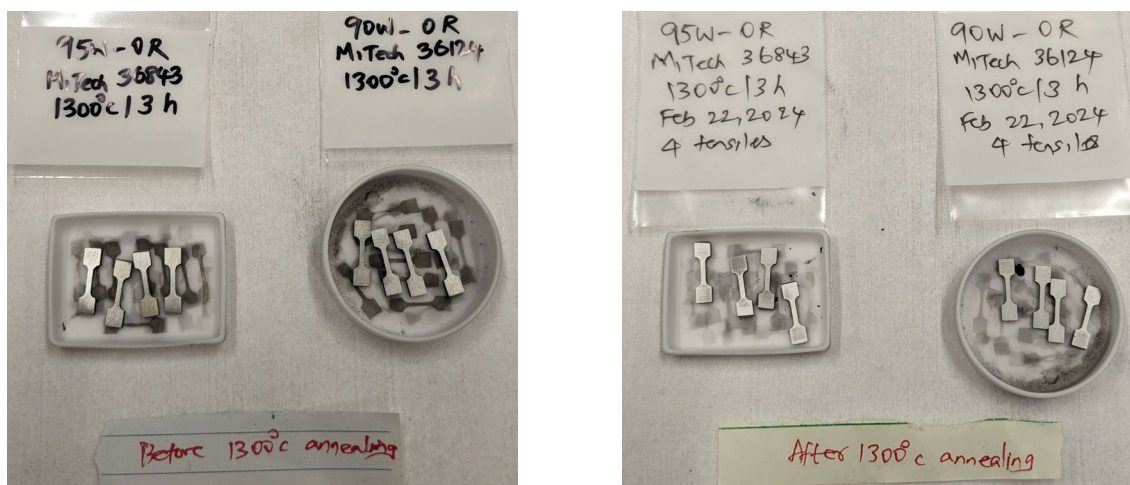


Figure 3. Tensile samples before and after 1300°C annealing for 3 hours.

Room temperature tensile testing of 1300°C annealed 90W samples

An Instron 8801 servo-hydraulic mechanical testing system was utilized for conducting tensile testing in the displacement control mode in order to determine the effect of annealing and optimum annealing time. This test system can be employed to perform both static and dynamic mechanical tests at ambient and elevated temperatures. Additional information on this test frame can be found in the previous report. [28] Both flat sides of the tensile samples that were annealed at 1300°C for different durations were polished to at least 1-micron condition to remove minor cracks and local residual stresses due to EDM.



Figure 4. Shoulder-loaded TZM tensile fixture.

During 2023, a study was performed using as sintered 90W-0R samples to determine if it is necessary to polish the tensile specimen's thickness sides also besides polishing the two flat sides. As mentioned in our previous report, the results showed that it is not necessary to polish the thickness sides (which is more labor intensive and prone to error due to hand polishing). [27]

The specimen gage width and thickness (see Figure 1) were measured using calipers prior to tensile testing. The displacement rate during tensile testing was constant at a crosshead speed of 0.06 mm/min (1 micron/s), which can be converted to an estimated strain rate of $1.99\text{E-}4/\text{s}$ for specimens with a 5.029 mm reduced length. Subsize tensile specimens were shoulder loaded instead of pin loaded to avoid tear out at the pin hole and warping of the pins, using the fixture shown in Figure 4. At least three annealed specimens per condition (duration) were tensile tested at room temperature.

The ASTM Standard E8/E8M was utilized for performing tensile testing and data analysis. [30] Load, displacement and time were recorded during tensile testing. The displacement was measured from the crosshead movement. The load data was obtained from the load cell. Engineering stress-strain curves were generated by using load-displacement data recorded during testing along with initial specimen gage width, thickness and reduced length. These curves were used to determine 0.2% offset YS, UTS, UE, and TE.

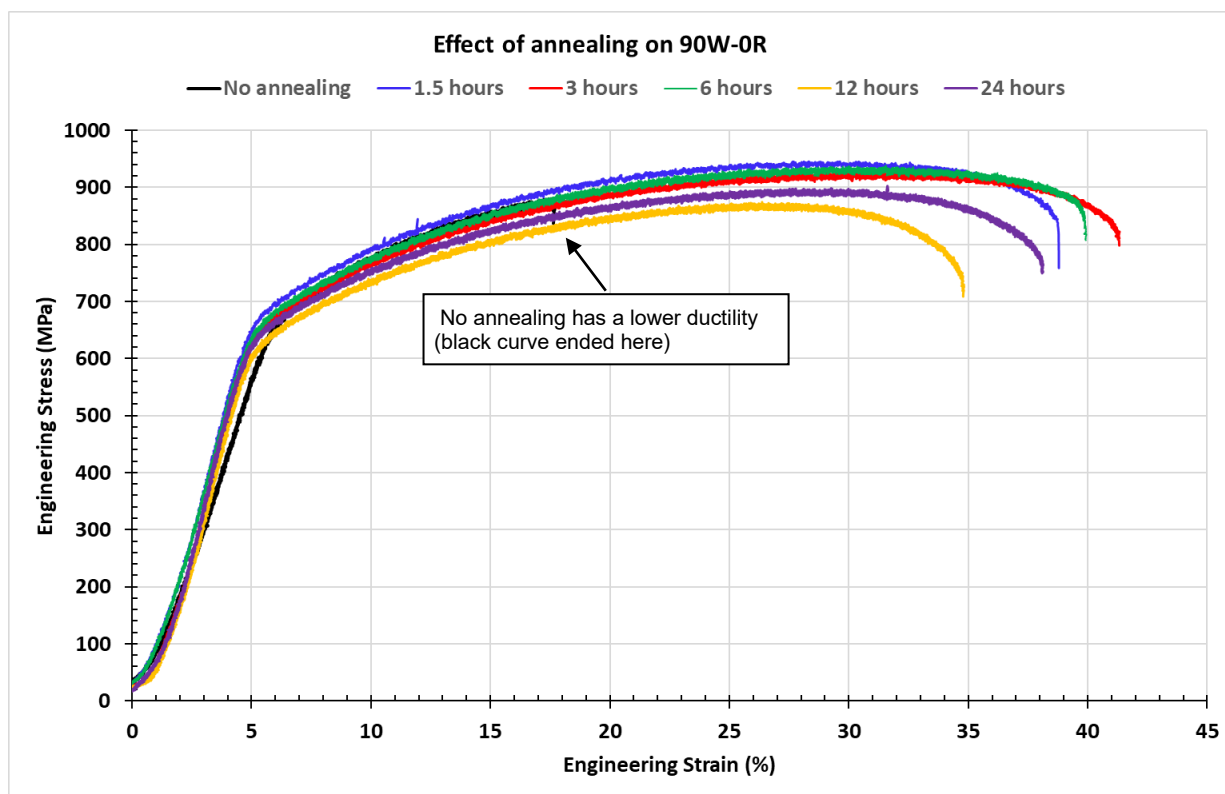


Figure 5. Room temperature engineering stress strain curves of 1300°C annealed 90W samples.

Representative engineering stress versus strain curves of sintered 90W samples before and after 1300°C annealing at various durations are shown in Figure 5. Table 2 shows the room temperature tensile properties generated from the engineering stress-strain data. The 0.2% offset YS values reduced slightly as the annealing duration was increased, and the highest reduction of 7% was at 12 hours duration (see Table 3; Figure 6). The UTS values increased by 9% when samples were annealed for 1.5 hours, and the percent change reduced as the duration was increased. Annealing increased the UE by more than 100% irrespective of the duration, and the highest increase (142%) was for 3 hours annealing. Annealing also increased the TE by almost more than 200% for all durations except 12 hours (191% increase). Annealing for 3 hours resulted in the highest increase (244%) in TE.

Based upon the available information (see Table 3), it appears that annealing at 1300°C for 3-6 hours is optimal for as sintered 90W samples. We chose 1300°C for 3 hours as the baseline, and then annealed multiple specimens to perform tensile testing at elevated temperatures.

Table 2. Room temperature tensile properties of 1300°C annealed 90W samples

Annealing	Sp ID	YS (MPa)	UTS (MPa)	UE (%)	TE (%)
None	1	650	875	10.10	10.15
	2	650	855	8.65	9.00
	3	650	865	10.90	11.37
	Average	650	865	9.88	10.17
	SD	0	10	1.14	1.19
1300°C/1.5 h	1	620	928	25.13	38.42
	2	640	940	22.80	32.82
	3	650	944	20.97	30.80
	4	650	957	22.48	31.30
	Average	640	942	22.85	33.34
SD	14	12	1.72	3.50	
1300°C/3 h	1	625	920	24.40	35.40
	2	613	921	23.02	34.12
	3	630	931	24.20	33.73
	4	635	929	23.92	36.82
	Average	626	925	23.89	35.02
SD	9	6	0.61	1.40	
1300°C/6 h	1	610	915	24.35	36.84
	2	630	920	22.45	32.60
	3	613	914	24.00	35.20
	4	630	930	23.35	34.00
	Average	621	920	23.54	34.66
SD	11	7	0.84	1.80	
1300°C/12 h	1	604	868	20.05	29.30
	2	605	882	22.70	31.60
	3	600	855	19.25	27.85
	Average	603	868	20.67	29.58
	SD	3	14	1.81	1.89
1300°C/24 h	1	605	890	21.62	32.57
	2	630	906	21.35	29.45
	3	613	893	22.50	33.40
	Average	616	896	21.82	31.81
	SD	13	9	0.60	2.08

Table 3. Difference in tensile properties of 90W samples due to 1300°C annealing for different durations

Annealing duration (hours)	Difference in tensile properties due to annealing				Annealing duration (hours)	% Difference in tensile properties due to annealing			
	YS (MPa)	UTS (MPa)	UE (%)	TE (%)		YS	UTS	UE	TE
0	-	-	-	-	0	-	-	-	-
1.5	-10	77	13	23	1.5	-2	9	131	228
3	-24	60	14	25	3	-4	7	142	244
6	-29	55	14	24	6	-5	6	138	241
12	-47	3	11	19	12	-7	0	109	191
24	-34	31	12	22	24	-5	4	121	213

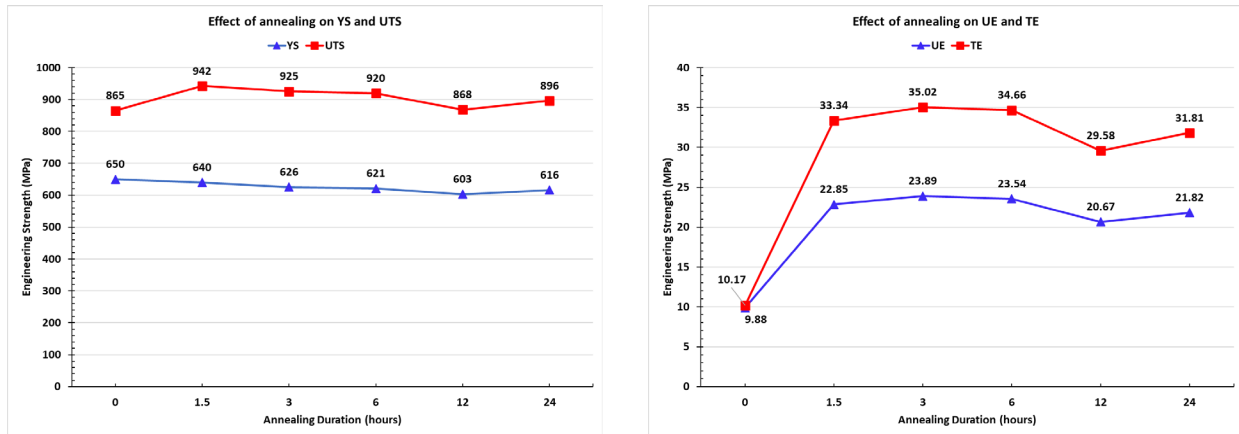


Figure 6. Effect of 1300°C annealing for different durations on sintered 90W tensile properties.

Elevated temperature tensile testing of 1300°C annealed 95W samples

An MRF Model M-4x6-M-1600-V&G front-loading furnace with a maximum operating temperature of 1600°C was utilized for elevated temperature tensile testing. The hot zone is a 180° split design with tungsten mesh heating elements for operation in vacuum (50-100 milliTorr) and inert gas (Ar, N₂ or Ar/O₂ gas mixture). The MRF furnace has a usable work zone of 3.5" dia. x 4.0" high. It has water-cooled pull rods (17-4 PH stainless steel) on either side of the furnace, and a tensile fixture that can withstand elevated temperatures without any water cooling is required. Additional information about this furnace can be found in previous reports. [28,29]



Figure 7. LEFT: Instron frame with MRF furnace for elevated temperature tensile testing; RIGHT: The TZM tensile fixture placed at the center of furnace hot zone.

The SiC fixtures can perform well at these elevated temperatures (>1000°C), however, the cost of machining is high, and durability is low, especially under tensile loading. Hence, efforts were made earlier to identify a metallic material and fixture design that would allow us to utilize the furnace and perform tensile testing at elevated temperatures close to 1000°C. Based upon material availability, machinability, cost, and

mechanical properties at elevated temperatures, TZM was chosen as the fixture material. An acronym for the molybdenum alloy 'titanium-zirconium-molybdenum', TZM is a molybdenum alloy containing 0.5% titanium, 0.08% zirconium, 0.02% carbon and the balance molybdenum. This TZM has a higher recrystallization temperature than pure molybdenum, thus reducing the likelihood of embrittlement at higher temperatures. And in elevated temperature applications, TZM's higher strength, hardness, creep resistance and ductility ensure that it will not weaken or soften. The recommended temperatures for using TZM is between 700 and 1400°C. [31] However, like pure molybdenum, TZM begins to oxidize at 400°C and oxides rapidly in oxidizing atmospheres above 500°C. Hence, it is required to utilize TZM under an argon purging or vacuum environment at elevated temperatures. Additional information about TZM can be found in our previous report. [12] The TZM tensile fixture fabricated at PNNL earlier is shown in Figure 4.

An Instron 8801 servo-hydraulic mechanical testing system was utilized for conducting elevated temperature tensile testing in the displacement control mode in order to determine the effect of temperature on the mechanical properties of annealed (1300°C/3 hours) 95W-0R specimens. Tensile testing was performed at the following temperatures: 245°C (0.3T_m); 418°C (0.4T_m), 591°C (0.5T_m), 764°C (0.6T_m) and 937°C (0.7T_m), where T_m is the melting temperature of nickel (1728K; 1455°C). Both flat sides of the annealed tensile specimens were polished to at least 1-micron condition to remove minor cracks and local residual stresses due to EDM. The specimen gage width and thickness were measured using calipers prior to tensile testing. Subsize tensile specimens (see Figure 1) were shoulder loaded instead of pin loaded to avoid tear out at the pin hole and warping of the pins, using the TZM fixture shown in Figure 4. Two specimens were tested per condition (test temperature).

The MRF furnace was connected to the Instron 8801 frame as shown in Figure 7. The TZM tensile fixture with a tensile specimen was connected to both sides of the water-cooled 17-4 PH stainless steel pull rods. The MRF furnace has two Type C thermocouples and it measured the temperature at the center of the hot zone (left and right sides). The tensile fixture was positioned in such a way that it is at the center of the heat zone, as shown in Figure 7. After placing the tensile fixture inside, the furnace door was closed. Argon purging at 5 standard liter per minute (SLPM) was performed for at least one hour (prior to heating), and then the temperature of the MRF furnace was gradually increased at a ramp rate of 3-5°C/min until it reached the desired test temperature (245°C, 418°C, 591°C, 764°C and 937°C). After reaching the desired test temperature, the tensile specimen was soaked at this temperature inside the furnace for at least three hours to ensure temperature uniformity across the specimen thickness.

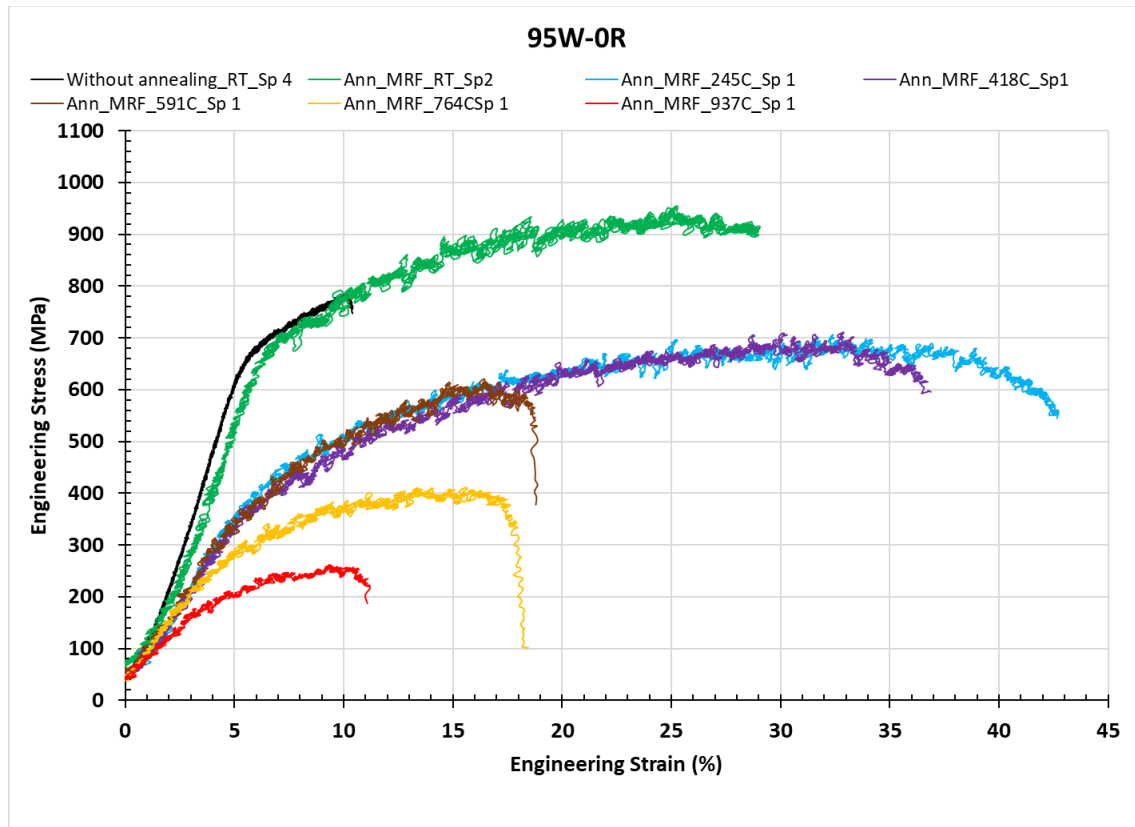


Figure 8. Engineering stress strain curves of 1300°C annealed 95W samples at different test temperatures. After completing the above-mentioned temperature soak process, the tensile testing process was initiated. The displacement rate during tensile testing was constant at a crosshead speed of 0.06 mm/min (1 micron/s), which can be converted to an estimated strain rate of $1.99\text{E-}4/\text{s}$ for specimens with a 5.029 mm reduced length. The ASTM Standard E8/E8M was utilized for performing tensile testing and data analysis.[30] Load, displacement and time were recorded during tensile testing. The displacement was measured from the crosshead movement. The load data was obtained from the load cell. After the completion of tensile testing, the furnace window door at the front was opened to take photos of tested tensile specimen and document the failure location. At the end of tensile testing, the furnace hot zone was shut down so that the tensile specimen cooled down via natural cooling. The argon purging was maintained until the furnace reached the ambient temperature.

Engineering stress-strain curves were generated by using load-displacement data recorded during testing along with initial specimen gage width, thickness and reduced length. These curves were used to determine 0.2% offset YS, UTS, UE, and TE. Representative engineering stress versus strain curves of 1300°C annealed 95W samples tested at different temperatures are shown in Figure 7. Due to the presence of furnace bellows (top and bottom – to prevent leakage), the stress-strain curves displayed some noise.

Table 4. Tensile properties of 1300°C annealed 90W samples at different test temperatures

Annealing	Temperature	Sp ID	YS (MPa)	UTS (MPa)	UE (%)	TE (%)
None	RT	1	665	809	5.80	5.97
		2	655	785	4.45	4.65
		3	650	765	3.32	3.87
		4	655	779	3.83	4.27
		Average	656	785	4.35	4.69
		SD	6	18	1.07	0.91
1300°C/3 h	RT	1	660	925	18.60	23.85
		2	655	927	18.40	24.40
		Average	658	926	18.50	24.13
		SD	4	1	0.14	0.39
1300°C/3 h	RT	1	611	961	16.44	17.69
		2	585	949	16.30	18.50
		Average	598	955	16.37	18.10
		SD	18	8	0.10	0.57
1300°C/3 h	RT	1	680	939	16.32	18.35
		2	650	929	16.83	20.98
		Average	665	934	16.58	19.67
		SD	21	7	0.36	1.86
1300°C/3 h	245°C	1	350	679	23.65	35.25
		2	355	660	23.73	36.93
		Average	353	670	23.69	36.09
		SD	4	13	0.06	1.19
1300°C/3 h	418°C	1	350	682	21.30	27.40
		2	320	682	22.00	28.25
		Average	335	682	21.65	27.83
		SD	21	0	0.49	0.60
1300°C/3 h	591°C	1	325	597	7.80	10.98
		2	320	558	7.10	10.50
		Average	323	578	7.45	10.74
		SD	4	28	0.49	0.34
1300°C/3 h	764°C	1	220	400	8.55	12.80
		2	250	395	7.41	12.82
		Average	235	398	7.98	12.81
		SD	21	4	0.81	0.01
1300°C/3 h	937°C	1	180	254	4.35	6.80
		2	170	237	3.75	5.75
		Average	175	246	4.05	6.28
		SD	7	12	0.42	0.74

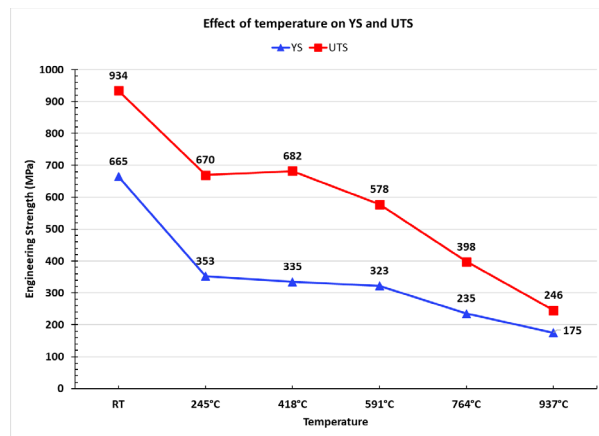
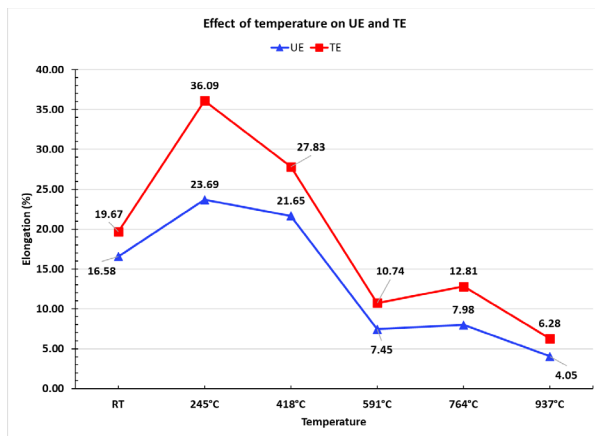


Figure 9. Effect of test temperature on 1300°C annealed 95W tensile properties.

Table 5. Difference in room and elevated temperature tensile properties of 1300°C annealed 95W samples

Difference in tensile properties compared to RT					% Difference in tensile properties compared to RT				
Temperature	YS (MPa)	UTS (MPa)	UE (%)	TE (%)	Temperature	YS	UTS	UE	TE
RT	-	-	-	-	RT	-	-	-	-
245°C	-313	-265	7	16	245°C	-47	-28	43	84
418°C	-330	-252	5	8	418°C	-50	-27	31	41
591°C	-343	-357	-9	-9	591°C	-52	-38	-55	-45
764°C	-430	-537	-9	-7	764°C	-65	-57	-52	-35
937°C	-490	-689	-13	-13	937°C	-74	-74	-76	-68

Table 4 shows the tensile properties (generated from the engineering stress-strain data) of 95W samples at different test temperatures. The 0.2% offset YS values reduced by ~50%, 65% and 74% as the test temperature was increased from room temperature to 245°C-591°C, 764°C and 937°C, respectively (see Table 5 and Figure 9). The UTS values also reduced by ~28%, 38%, 57% and 74%, as the test temperature was increased from room temperature to 245°C-481°C, 591°C, 764°C and 937°C. The UE and TE increased by 43% and 84%, respectively as the test temperature was increased from RT to 245°C. As the test temperature was further increased to 418°C, the increase in ductility was lower (31% UE and 41% TE). However, as the test temperature was $\geq 591^\circ\text{C}$, UE and TE values reduced compared to room temperature values. When tested at 937°C, the UE and TE reduced significantly by 76% and 68%, respectively.

Results

The following activities are being planned to be performed:

- Perform fractography of annealed 95W tensile tested specimens at various elevated temperatures (245°C, 418°C, 591°C, 764°C and 937°C)
- Perform room and elevated temperature fracture toughness testing of annealed (sintered) samples.
- Perform 1300°C annealing on recently hot-rolled 90W-66R (3:1 aspect ratio) and 90W-83R 66R and 83R (6:1 aspect ratio) samples, and then conduct room and elevated temperature tensile and fracture toughness testing to evaluate the effect of annealing and HR on the mechanical behavior of 90W alloy.

Acknowledgments

This research was supported by the U.S. Department of Energy (US DOE), Office of Science, Office of Fusion Energy Sciences, through Contract No. AT2030110-13784 and was performed at the PNNL, which is operated by Battelle for the US DOE under Contract No. DE-AC05-76RL0-1830.

References

- [1.] S. Wurster, et al., *Recent progress in R&D on tungsten alloys for divertor structural and plasma facing materials*. Journal of Nuclear Materials, 442 (1-3): p. S181-S189, 2013.
- [2.] D. Stork, et al., *Developing structural, high-heat flux and plasma facing materials for a near-term DEMO fusion power plant: the EU assessment*. Journal of Nuclear Materials, 455(1-3): p. 277-291, 2014.
- [3.] A. Hasegawa, et al., *Neutron irradiation effects on the microstructural development of tungsten and tungsten alloys*. Journal of Nuclear Materials, 471: p. 175-183, 2016.
- [4.] R. Neu, et al., *Investigations on tungsten heavy alloys for use as plasma facing material*, Fusion Eng. Des. 124 (2017) 450–454.
- [5.] R. Neu, et al., *Results on the use of tungsten heavy alloys in the divertor of ASDEX Upgrade*, J. Nucl. Mater. 511 (2018) 567–573.

- [6.] M. Alam, et al., *The effect of hot rolling on the strength and fracture toughness of 90W-7Ni3Fe tungsten heavy metal alloys*, Materials Science & Engineering A 824, 141738, 2021.
- [7.] G.M. Wright, et al., *Comparison of tungsten nano-tendrils grown in Alcator C-Mod and linear plasma devices*, J. Nucl. Mater. 438 (2013) S84–S89.
- [8.] D. Dasgupta, et al., *Prediction of temperature range for the onset of fuzz formation in helium-plasma-implanted tungsten*, Surf. Sci. 698 (2020) 121614.
- [9.] Q. Yang, et al., *Nanostructured fuzz growth on tungsten under low-energy and high-flux He irradiation*, Sci. Rep. 5 (2015) 1–9.
- [10.] J. Wang, et al., *Tensile testing and microstructural characterization of ductile phase toughened W-NiFe alloys*, in Fusion materials Semiannual Progress Report for the Period Ending June 30, 2020, 2020.
- [11.] J. Wang, et al., *Microstructural characterization and mechanical testing of ductile-phase toughened tungsten*, in Fusion materials Semiannual Progress Report for the Period Ending December 31, 2019, 2019.
- [12.] R. Prabhakaran, et al., *Status of the elevated temperature mechanical test facility, hot rolling and tensile testing at PNNL*, PNNL-SA-181771, Vol 73, Chapter 4, in Fusion Materials Semiannual Progress Report for Period Ending December 31, 2022, DOE/ER-0313/73, U.S. Department of Energy, 2023.
- [13.] X. Gong, et al., *Effect of tungsten content on microstructure and quasi-static tensile fracture characteristics of rapidly hot extruded W-Ni-Fe alloys*, Int. J. Refract. Metals Hard Mater. 30 (2012) 71–77.
- [14.] X. Gong, et al., *Microstructure and highly enhanced mechanical properties of fine-grained tungsten heavy alloy after one-pass rapid hot extrusion*, Mater. Sci. Eng. 528 (2011) 3646–3652.
- [15.] Z.S. Levin, K. Ted Hartwig, *Hardness and microstructure of tungsten heavy alloy subjected to severe plastic deformation and post-processing heat treatment*, Mater. Sci. Eng. 635 (2015) 94–101.
- [16.] Y. Yang, et al., *Microstructure and mechanical properties of a hydrostatically extruded 93W-4.9Ni-2.1Fe alloy*, Mater. Sci. Eng. 435–436 (2006) 620–624.
- [17.] Y. Yu, H. Hu, et al., *Microstructure evolution and recrystallization after annealing of tungsten heavy alloy subjected to severe plastic deformation*, J. Alloys Compd. 685 (2016) 971–977.
- [18.] Y. Yu, et al., *Effect of heat treatment on microstructure and mechanical properties of hydrostatically extruded 93W-4.9Ni-2.1Fe alloy*, J. Alloys Compd. 622 (2015) 880–884.
- [19.] Z.H. Zhang, et al., *Deformation characteristics of the 93W-4.9Ni-2.1Fe tungsten heavy alloy deformed by hydrostatic extrusion*, Mater. Sci. Eng. 435–436 (2006) 632–637.
- [20.] C. Henager Jr., et al., *Ductile-phase toughened tungsten for plasma-facing materials in fusion reactors*, Int. J. Powder Metall. 53 (2017) 53–69.
- [21.] B.N. Nguyen, et al., *Tailoring ductile-phase toughened tungsten hierarchical microstructures for plasma-facing materials*, J. Nucl. Mater. 540 (2020) 152382.
- [22.] R. Prabhakaran, W. Setyawan, *High-temperature mechanical testing of W/Ni-Fe ductile-phase toughened W composites*, PNNL-SA-194713, Vol. 75, Chapter 4, In Fusion Materials Semiannual Progress Report for Period Ending Dec 31, 2023, DOE/ER-0313/75, U.S. Department of Energy, 2024.
- [23.] R.M. German, L.L. Bourguignon, Powder Met. Def. Technol., 6 (1984), pp. 117-131.
- [24.] M. Li, et al., *Impact of heat treatment on tensile properties of 97W-2Ni-1Fe heavy alloy*, Journal of Nuclear Materials, Volume 512, 15 December 2018, Pages 1-7.
- [25.] M.E. Alam, G.R. Odette, *Improving the fracture toughness and ductility of liquid-phase sintered WNiFe tungsten heavy alloys by high-temperature annealing*. Materials (Basel). 2023 Jan 18;16(3):916.
- [26.] M.E. Alam, G.R. Odette, *On the influence of specimen size and geometry on the fracture toughness of tungsten heavy metal alloys*. J. Nucl. Mater. 2022;571:154025.
- [27.] R. Prabhakaran, et al., *High temperature mechanical testing of W/NiFe ductile-phase toughened W composites*, PNNL-SA-188793, Vol 74, Chapter 4, in Fusion Materials Semiannual Progress Report for Period Ending June 30, 2023, DOE/ER-0313/74, U.S. Department of Energy, 2023.

- [28.] R. Prabhakaran, et al., *Status of the elevated temperature mechanical test facility setup at PNNL*, PNNL-SA-170069, Vol 71, Chapter 4, In Fusion Materials Semiannual Progress Report for period ending December 31, 2021, DOE/ER-0313/71, US Department of Energy, 2022.
- [29.] R. Prabhakaran, et al., "*Status of the elevated temperature mechanical test facility setup at PNNL*", PNNL-SA-176100, Vol 72, Chapter 4, In Fusion Materials Semiannual Progress Report for Period Ending June 30, 2022, DOE/ER-0313/72, U.S. Department of Energy, 2022.
- [30.] ASTM E8/E8M-21, Standard Test Methods for Tension Testing of Metallic Materials, ASTM International, West Conshohocken, PA, 2021.
- [31.] Rembar website; <https://www.rembar.com/when-to-use-tzm-alloy-instead-of-pure-molybdenum>; updated July 30, 2020 (accessed 31 Aug 2024).

4.4 MECHANICAL RESPONSES OF TUNGSTEN IN A DUCTILE-PHASE-TOUGHENED TUNGSTEN HEAVY ALLOY TO ION IRRADIATION SIMULATING FUSION REACTOR ENVIRONMENTS—A. Garcia-Caraveo, S. Doran, T. Rohwer, T. Chen (Oregon State University), L. Shao (Texas A&M University), W. Jiang, J. V. Haag IV, R. Prabhakaran, W. Setyawan (Pacific Northwest National Laboratory)

OBJECTIVE

In this reporting period, nanomechanical testing were applied to ion-irradiated ductile-phase-toughened (DPT) tungsten heavy alloys to evaluate irradiation hardening and embrittlement. More specifically, the hardness and fracture toughness of the brittle and ductile phases were reported following three types of irradiation at 500°C, i.e., He⁺ only, Ni⁺ only, and sequential Ni⁺ + He⁺ irradiation. Through this project, a graduate student from an under-represented group was recruited. The student was selected to spend a summer internship at Pacific Northwest National Laboratory (PNNL) to continue her training on transmission electron microscopy and focused ion beam (FIB), which are fundamental skills for the success of this project. This effort promotes the Department of Energy's (DOEs) education mission and the future workforce pipeline for United States (US) energy sectors.

SUMMARY

The DPT W-Ni-Fe heavy alloys (WHAs) have significantly improved fracture toughness compared to tungsten, mitigating the brittle challenge of W-based plasma-facing materials. With the strong interface between the hard and the ductile phases, microcracks initiated in the hard W phase are arrested and blunted by the ductile NiFeW phase, which also bridges co-planar microcracks [1, 2]. However, after ion irradiation (which emulates helium accumulation and radiation damage effects of 14 MeV neutrons), helium cavities were observed at the W/NiFeW interface [3], raising concerns about possible interfacial debonding, which impairs the above toughening mechanisms. Further development, evaluation, and qualification of DPT alloys for fusion applications require answering the following questions. (1) To what extent does the radiation damage affect the mechanical properties and microcrack initiation and propagation behavior? (2) How can we design new DPT alloys with tailored composition and microstructure for improved performance in fusion environments? One critical step to answering these questions and understanding the mechanisms is quantifying the microstructure-specific properties, which will also provide input to computational models for performance prediction and microstructure optimization. Yet, given the shallow irradiated zones of ion irradiation samples, small-scale mechanical testing is the only feasible technique.

Small-scale mechanical testing has demonstrated success in characterizing mechanical responses to ion irradiation. Prior studies mainly applied nanoindentation based techniques to understand irradiation hardening effects [4–6]. On the other hand, instrumented nanomechanical stages for in-situ scanning electron microscopy (SEM) enable mechanical testing on focused-ion FIB milled specimens with different geometries, introducing different stress fields to derive different micromechanical properties. Our previous project report summarized the demonstrations of notched and unnotched microcantilever bending and micropillar compression techniques in obtaining microscopic fracture toughness, elastic modulus, and critical resolved shear stress of the W phase [7].

PROGRESS AND STATUS

Introduction

In this report, we present the irradiation hardening of W and NiFeW phases under different irradiation conditions, as well as the degradation of fracture toughness of W due to irradiation. The results indicate irradiation-induced embrittlement of the W phase and possible degradation of the DPT mechanisms.

Experimental Procedure

Materials & Irradiation

The material used for this research is W-NiFe alloy sample W90, which contains 90W-7Ni3Fe (by wt%). The alloy is a liquid-phase sintered material that consists of hard, single-crystal body-centered-cubic (BCC) tungsten spheres embedded in a matrix of ductile face-centered-cubic (FCC) Ni-Fe-W phase. The sample was supplied and mechanically polished by PNNL. The irradiation was performed at the Accelerator Laboratory, Texas A&M University. As shown in Figure 1a, the sample was partially masked and successively irradiated with Ni⁺ and He⁺ ions, at a nominal temperature of 500°C. By adjusting the mask positions, the irradiated sample contains four different regions, namely, Ni⁺ irradiated, Ni⁺ and He⁺ successively irradiated, He⁺ irradiated, and unirradiated.

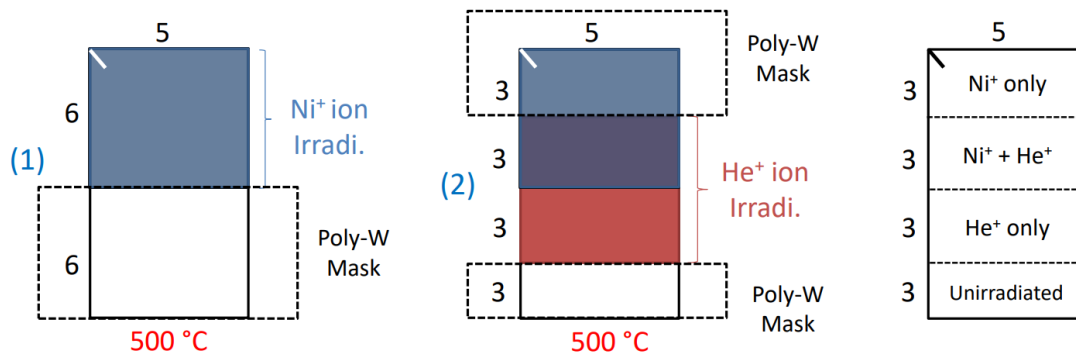


Figure 1. Irradiation layout to realize four different irradiation conditions on a single irradiated sample.

A uniform damage profile deeper than 1 μm facilitate micromechanical testing by mitigating the variance of mechanical property within the tested sample volume. However, ion irradiation is known to produce ununiform damage profile due to the dependence of stopping power on ion energies. With the aid of Stopping and Range of Ions in Matter (SRIM)13 simulations [8], Ni⁺ ions of three different energies, and 1.8 MeV He⁺ at ten different glancing angles, were irradiated to the sample with the fluence of each condition carefully determined to achieve flat displacement damage and helium distribution profiles. As shown in Figure 2, the displacement damages are approximately 27.3 and 30 displacements per atom (dpa), with implanted helium of 0.0607 and 0.0384 at. %, in W and NiFeW phases, respectively. The helium – dpa ratios are approximately 22.2 and 12.8 appm/dpa in W and NiFeW phases, respectively.

EI-Guebaly et al. assessed the neutron activation, radiation damage and transmutation products in different WHAs as the divertor in the ARIES-ACT2 configuration [9]. Data interpolation showed that the W90 alloy would receive ~26 and ~92 dpa in the W and NiFeW phases, respectively, after 10 years of operation (8.65 full power years) at the front of the divertor dome. Based on the transmutation calculations in pure W, Ni and Fe, reported in [9], the accumulated helium – dpa ratios after 10 years of operation under the same condition above would be 0.62 and 12.8 appm/dpa in W and NiFeW phases, respectively. On a first-order approximation, this ion-irradiation experiment intends to simulate dpa damages equivalent to 10 and 3.3 years of operation for the W and NiFeW phases, respectively. We preserve the helium – dpa ratio in the NiFeW phase in the experimental design, while exaggerating the helium content in W by a factor of ~36 compared to that under the ARIES-ACT2 fusion conceptual condition. For this report focusing on the mechanical responses of the W phase, this exaggeration provides a conservative evaluation of helium embrittlement, which is a potential materials challenge suggested by our previous microstructure characterization results [3, 10].

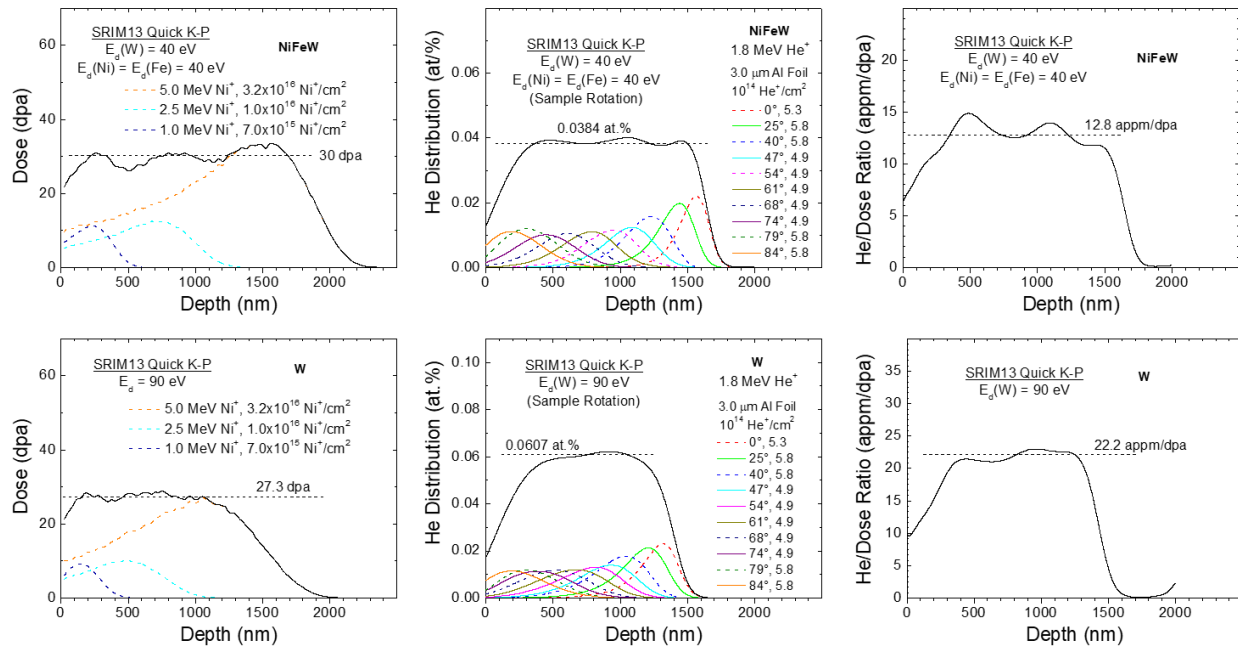


Figure 2. Depth profiles of the displacement damage, He concentration, and appm/dpa ratio from quick Kinchin-Pease SRIM13 simulations of Ni⁺ and He⁺ irradiations in NiFeW and W.

Micromechanical testing

To study irradiation hardening, nanoindentation with a Berkovich tip was performed using the FemtoTools FT-NMT04 nanoindenter. Within each region of a certain irradiation condition, 45 indents were performed. Displacement-controlled mode was used to reach a maximum depth of 250 nm at a displacement rate of 125 nm/s. To obtain continuous hardness data at different indentation depth, continuous stiffness measurement (CSM) technique was applied.

Microcantilevers were fabricated using a Quanta 3D SEM / FIB system. The micro-milling was done using gallium ions of 30 keV. Initial milling employs high beam current of 15 nA, which was gradually reduced to 0.5 nA to finish the specimen preparation. The lower beam current was employed to achieve a fine finish of the specimen surface. To cut the sharp notch, a current of 18 pA was used.

Free-standing notched microcantilevers were employed to test the fracture toughness of the W phase before and after different types of irradiations. A straight-trough notch (STN) geometry with a rectangular-shaped cross section was employed for the easiness of data processing and the existence of reference protocols in the literature [11]. The microcantilever geometry and dimensions where $b = 1 \mu\text{m}$, $w = 1 \mu\text{m}$, $a = 0.35 \mu\text{m}$, $L_0 = 0.35 \mu\text{m}$ and $L_1 = 5 \mu\text{m}$, as shown in Figure 3.

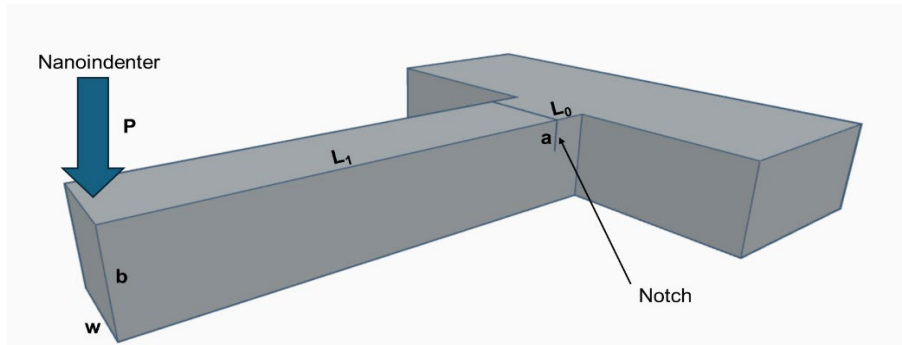


Figure 3. Free-standing STN microcantilever dimension diagram reference.

In-situ SEM bending experiments were performed with a FemtoTools FT-NMT04 nanoindenter. The in-situ data allows the analysis of the cantilever displacement, fracture initiation and crack propagation. A sharp wedge tip was used to apply the load in a displacement-controlled mode with a displacement rate of 50 nm/s. During microscopic fracture toughness testing, CSM technique was employed to obtain a stiffness evolution for crack length estimation. The CSM frequency and oscillation amplitude were chosen to be 200 Hz and 20 nm, respectively.

Irradiation Hardening

Figure 4 shows the hardness as a function of indentation depth obtained from the W and NiFeW phases for different irradiation conditions. Data points from different phases were differentiated with the aid of optical micrographs of the indentation marks. Selected data points were used to calculate the mean hardness of different regions from a contact depth range from 0.1 to 0.15 μm , as shown in Table 1. There is a clear hardening effect from each irradiation condition compared to the unirradiated sample on W single crystals. In both phases, hardness increases in the order of unirradiated, He⁺ irradiated, Ni⁺ irradiated, and He⁺ + Ni⁺ irradiated. Irradiation hardening is more severe in the W than the NiFeW phase. For the W phase, He⁺, Ni⁺, and Ni⁺+He⁺ irradiations caused increases in hardnesses of approximately 25%, 59%, and 61%, respectively. For the NiFeW phase, He⁺ irradiation caused approximately 7% increase in the hardness, while Ni⁺ and Ni⁺+He⁺ irradiations have similar hardening effects of approximately 12% increase in the hardnesses.

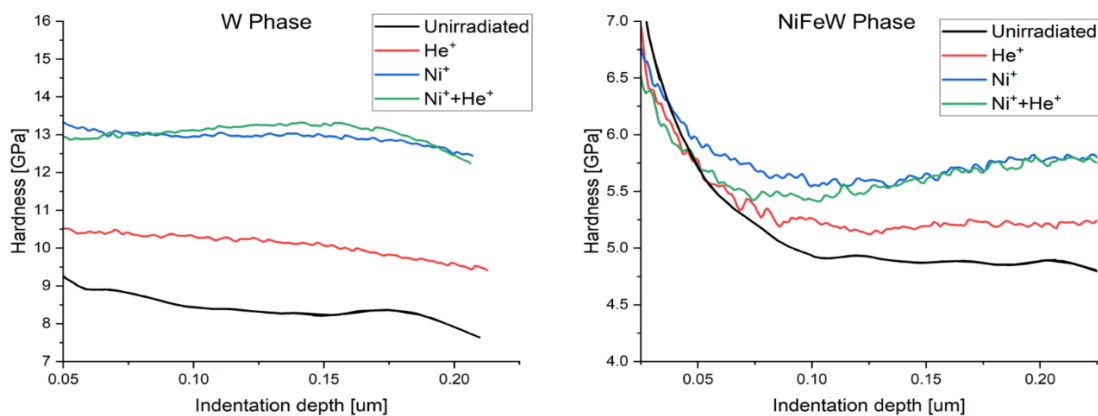


Figure 4. Phase-specific (averaged) hardness profiles of irradiated conditions for W phase (a) and NiFeW phase (b). Each presented curve is an average of more than 12 indents for the W phase and more than 4 indents for the NiFeW phase.

Table 1. Average hardness and Elastic Modulus for W and NiFeW phases of the different irradiation conditions

	Av. Hardness (GPa)		Elastic Modulus (GPa)	
	W	NiFeW	W	NiFeW
Unirradiated	8.3 ± 0.4	4.92 ± 0.07	320 ± 20	220 ± 10
He⁺	10.2 ± 0.3	5.3 ± 0.2	234 ± 5	163 ± 9
Ni⁺	13.0 ± 0.3	5.20 ± 0.8	257 ± 6	172 ± 6
Ni⁺ + He⁺	13.2 ± 0.3	5.5 ± 0.1	260 ± 6	169 ± 7

The He⁺ irradiated zone presents observable hardness increase compared to the unirradiated zone. Besides defects, He⁺ irradiation at high temperatures produce complexes of helium and vacancies and helium bubbles. According to Cui et al., He bubble accumulation is the main cause of hardening at an irradiation temperature of around 800°C in Tungsten, where the homologous temperature (Th) is Th = 0.29 [12, 13]. In this study, at a lower irradiation temperature of 500°C, where Th = 0.21 for W and Th = 0.45 for NiFeW, helium-vacancy complexes and helium bubbles are expected to be the main contributor to hardening in the He⁺-irradiated condition.

Ni⁺ irradiation primarily introduced hardening via the formation of voids and dislocation loops. Following Ni⁺ irradiation, the relative hardness increase is more significant in the W phase than in the NiFeW phase. This can be rationalized by the higher melting temperature of W, hindering defect recovery at 500°C. On the other hand, in the NiFeW phase, both interstitial, vacancy and even some loops are mobile [14], mitigating the accumulation of defect structures.

Between Ni⁺ and Ni⁺ + He⁺ irradiation zones, the hardness differences are insignificant for both W and NiFeW phases. It is possible that the similar hardness values for both irradiated zones were a result of the sequential nature of the irradiation, as opposed to simultaneous. The Ni⁺ + He⁺ irradiated zone was first exposed to Ni⁺ irradiation which introduces vacancy clusters/voids and dislocation damage structures. When He⁺ ions were implanted later, the existing defect structures may serve as sinks to both He atoms and point defects, mitigating the hardening effect from He⁺ irradiation. In addition, during the He⁺ irradiation at elevated temperature and with low dpa rate, the damage structure introduced by Ni⁺ may even experience thermal recovery.

The nanoindentation data also showed reduction of elastic moduli of both phases after irradiation, with the level of degradation more significant in W than NiFeW. Both phases see the most significant elastic modulus reduction after He⁺ irradiation than other conditions. This trend agrees with the theoretical prediction that elastic modulus decreases with increasing vacancy concentration. As helium stabilizes vacancies and small clusters, He⁺ irradiation alone causes more elastic modulus degradation than the other two irradiation conditions. This also agrees with the abovementioned speculation that defect structures formed under Ni⁺ irradiation may capture some of the implanted helium and thus mitigate the impact of implanted helium on elastic modulus.

Fracture toughness

Figure 5 shows the single-crystal tungsten microcantilevers for each irradiated condition before loading and after fracture initiation and propagation, in a-d and e-h, respectively. Guided by the electron backscatter diffraction (EBSD) survey on the irradiated sample, these microcantilevers were prepared with the {100} cleavage planes nearly normal to the beam longitudinal direction. During the micromechanical tests, the fractures were found to propagate along the cleavage planes.

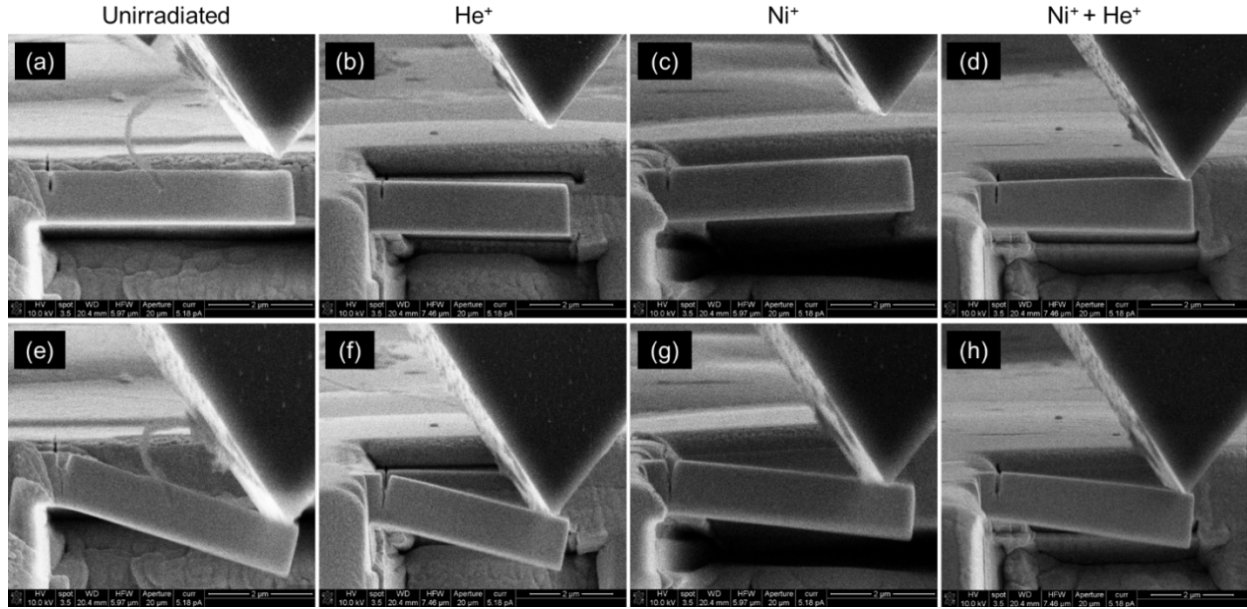


Figure 5. Snapshots during the in-situ bending tests of notched W microcantilevers for each irradiated condition before the test (a-d) and during the test (e-f).

The crack resistance was evaluated using the J-integral method to consider the effects of plasticity on fracture, as subjected to change by radiation damage. Taking input of the raw data of load (P), displacement (u), and stiffness (k), the analysis considers elastic plastic fracture mechanics (EPFM) and uses the iterative method described in American Society for Testing and Materials (ASTM) Standards 1820 [15]:

$$J(a) = J^{el}(a) + J^{pl}(a) \quad (1)$$

$$J_n^{el} = \frac{K_{q,n}^2(1-\nu^2)}{E} \quad (2)$$

$$J_n^{pl} = \left\{ J_{n-1}^{pl} + \frac{\eta_n}{b-a_n} \frac{A_n^{pl} - A_{n-1}^{pl}}{w} \right\} \left\{ 1 - \gamma_n \frac{a_n - a_{n-1}}{b - a_n} \right\} \quad (3)$$

where $J^{el}(a)$ and $J^{pl}(a)$ are the elastic and plastic J-integral values at specific crack lengths a . For each single-phase W microcantilever, the $J^{el}(a)$ was evaluated using the elastic modulus values obtained from the nanoindentation experiments of each irradiated condition shown in Table 1, and $\nu = 0.28$. The number of iteration steps is n and the stress intensity factor K_q was evaluated following ASTM 399 [16]

$$K_{q,n} = \frac{P_n L_P}{w b^{1.5}} f\left(\frac{a_n}{b}\right) \quad (4)$$

$$f\left(\frac{a_n}{b}\right) = 4 \frac{3\left(\frac{a_n}{b}\right)^{0.5} \left(1.23 - \left(\frac{a_n}{b}\right)\right) \left(1 - \left(\frac{a_n}{b}\right)\right) \left(-6.09 + 13.96\left(\frac{a_n}{b}\right) - 14.05\left(\frac{a_n}{b}\right)^2\right)}{2\left(1 + 2\left(\frac{a_n}{b}\right)\right) \left(1 - \left(\frac{a_n}{b}\right)\right)^{1.5}} \quad (5)$$

Here b and w are geometric dimensions as shown in Figure 3, L_P is the distance from the applied load to the notch, P is the load, and $f(a_n/b)$ is a geometry factor specified for the cantilever geometry, as proposed by Wurster et al. [11].

According to Alfreider *et al.* [17], the crack length can be calculated using the stiffness evolution during the bending test, in which the crack length a_n was found by the following correlation:

$$\left(\frac{a_n}{b}\right) = 1 - 2.897 \left(\frac{k_n}{k_{max}}\right) + 10.618 \left(\frac{k_n}{k_{max}}\right)^2 - 23.620 \left(\frac{k_n}{k_{max}}\right)^3 + 24.497 \left(\frac{k_n}{k_{max}}\right)^4 - 9.600 \left(\frac{k_n}{k_{max}}\right)^5 \quad (6)$$

where a_n is the crack length, k_n is stiffness and k_{max} is the maximum value of stiffness obtained during the test.

The plastic part of the J-integral was calculated using geometry independent prefactors $\eta = 1.9$ and $\gamma = 0.9$ as proposed for straight-trough notch bend specimen in ASTM 1820 [15]. The plastic work A^{pl} was computed numerically from the load-displacement curve for each point n where u_n , P_n and k_n are the respective displacement, load and stiffness shown in the following equation:

$$A_n^{pl} = A_n - A_n^{el} = \int_0^{u_n} P du - \frac{P_n^2}{2k_n} \quad (7)$$

Since J-integral is a function of the crack length a_n , using equation 6, the crack extension during the bending test was calculated using the measured stiffness k . Figure 6, shows the calculated crack length compared with the load-displacement curve for the single-phase W microcantilevers for each irradiated condition.

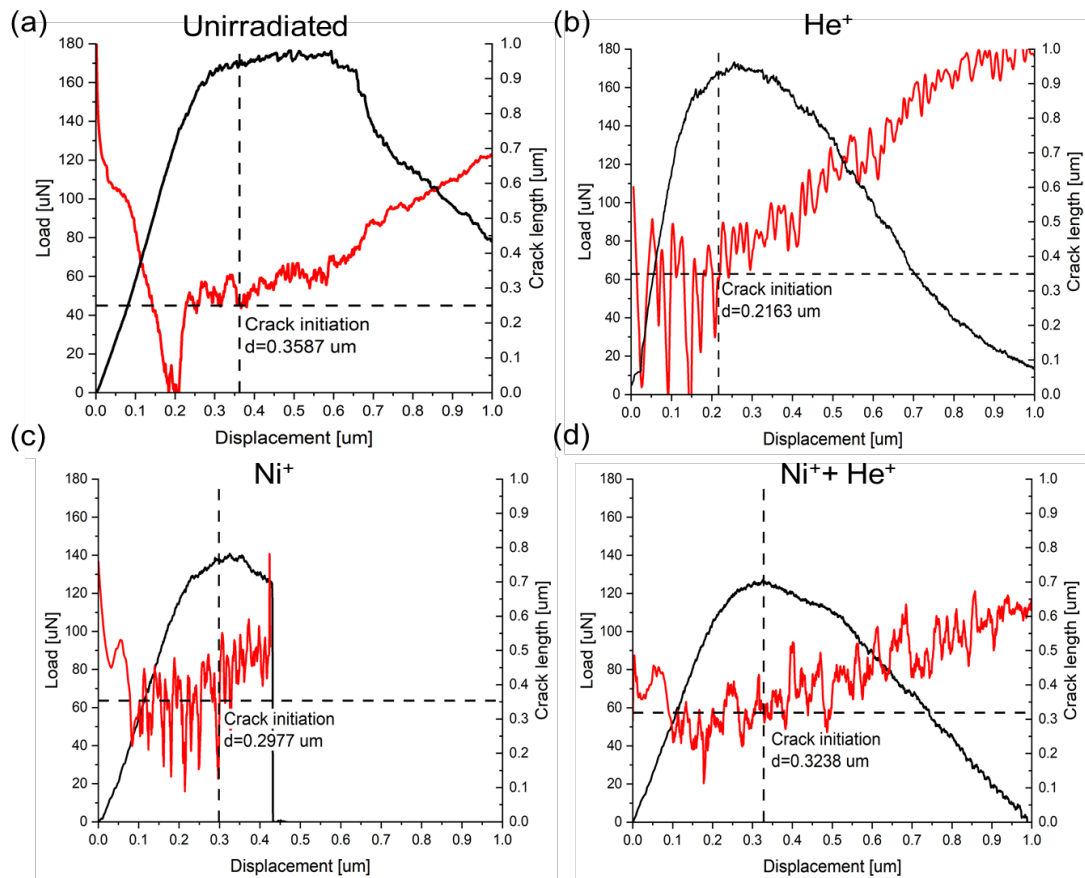


Figure 6. Load-displacement curve (black) and crack length curve (red) show crack initiation and growth for unirradiated (a), He⁺ irradiated (b), Ni⁺ irradiated (c), and Ni⁺ and He⁺ irradiated (d) microcantilevers.

The J-Integral curve was generated from Equation 1, where the J elastic component was calculated using Equation 2, and the J plastic component was calculated from Equation 3. Figure 7 shows the plot of the result, and the J initiation obtained from the crack initiation value for each irradiated condition.

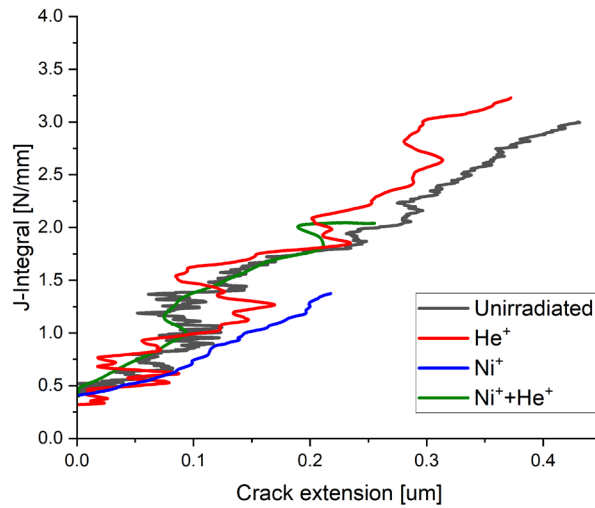


Figure 7. J-curve for W unirradiated (a), He⁺ irradiated (b), Ni⁺ irradiated (c), and Ni⁺ and He⁺ irradiated (d) microcantilevers.

K_i , the fracture initiation toughness, was determined using the following equation and the results are shown in Table 2.

$$K_i = \sqrt{\frac{EJ_i}{(1-\nu^2)}} \quad (8)$$

Table 2. Fracture toughness for single-phase W microcantilevers per irradiated condition

Sample	Crack initiation		
	Displacement	J_i	K_i
	[μm]	[N/mm]	$\text{MPa}\cdot\text{m}^{1/2}$
Unirradiated	0.3587	0.4400	12.4
He ⁺	0.2163	0.3205	9.02
Ni ⁺	0.2977	0.4098	10.68
Ni ⁺ + He ⁺	0.3238	0.4028	10.65

Shown in Figure 8, fractography was obtained for each irradiated condition. Ductile fracture surfaces were observed for all the cases except the Ni⁺ irradiated condition, agreeing to the J curves shown in Figure 7. Even for the Ni⁺ irradiated microcantilever, river marks are observable, indicating low level of plasticity during the crack initiation and propagation processes.

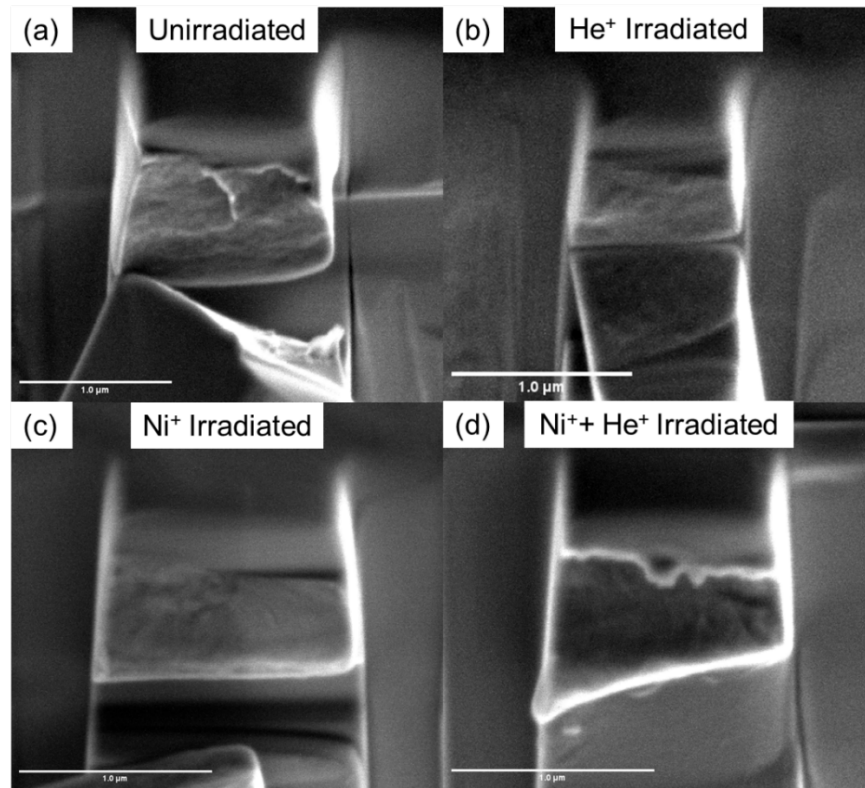


Figure 8. Fractography for single-phase W unirradiated (a), He⁺ irradiated (b), Ni⁺ irradiated (c), and Ni⁺ and He⁺ irradiated (d) microcantilevers.

By combining nanoindentation and microcantilever bending tests, we gain comprehensive insights into the mechanical response of the tungsten phase after different types of ion irradiations. The knowledge leads to the following speculations that may inspire future studies. Firstly, it is believed that He⁺ alone promotes the accumulation of vacancies more than the other two irradiation conditions. Consequently, the He⁺ irradiated tungsten exhibits the lowest elastic modulus and fracture initiation toughness compared to the samples irradiated under the other two conditions. The reduction in fracture initiation toughness may be attributed to the loss of bonding strength due to the increased vacancy content.

Secondly, plasticity plays an important role during the fracturing of the tungsten micro-cantilevers. In fact, plasticity is believed to be more pronounced in the dispersed form of tungsten particles in DPT alloys than in bulk tungsten. In this study, we observed that the Ni⁺ irradiated sample lost most plasticity, as indicated by the J-curves in Figure 7. This aligns with the greater hardening effect of Ni⁺ irradiation than He⁺, as reflected by the hardness results in Table 1. We believe that irradiation-induced defect structures may play a significant role in hardening and reducing plasticity.

Thirdly, it is interesting to observe that the “Ni⁺+He⁺” irradiation produces a similar hardening effect to Ni⁺ irradiation alone but less embrittlement in the microcantilever bending experiments. While additional microcantilever bending tests are needed to improve the statistical reliability, it is possible that during the low-dpa He⁺ irradiation at elevated temperature, some defects introduced through the prior Ni⁺ irradiation were recovered.

Results

As discussed above, additional microcantilever bending tests will be conducted, with the in-situ SEM focusing on the plasticity during the fracture processes. To better understand how irradiation affects the

degradation of fracture toughness, it is essential to analyze the radiation damage using TEM. This will help correlate the changes in microstructure due to irradiation with the resulting embrittlement and understanding the relationship between plasticity loss during fracture and hardening. Furthermore, this current study emphasizes the importance of understanding the plasticity behavior across the hard-ductile interface and its propagation into the ductile phase. While tungsten experiences considerable embrittlement, the ductile phase exhibits less irradiation hardening. Since the primary toughening mechanisms in DPT alloys rely on the plasticity and cohesion of the ductile phase, evaluating the interfacial mechanical properties of various DPT alloys after irradiation may be critical for designing and assessing DPT alloys for fusion applications. Lastly, the current study also suggests that the interaction between different types of irradiations and the competition between thermal and athermal effects may influence the damage microstructure development and the mechanical property degradation. Given that ion irradiation is the only feasible technique to surrogate material damage under conceptual fusion conditions, it is critical to evaluate the atypical effects of ion irradiations to support future design of ion irradiation experiments as surrogate to fusion neutron damage.

Acknowledgements

This research was supported by the US DOE, Office of Science, Office of Fusion Energy Sciences, through Contract No. AT2030110-13784 and was performed at PNNL, which is operated by Battelle for the US DOE under Contract No. DE-AC05-76RL0-1830.

References

- [1.] Alam ME, Odette GR (2020) On the remarkable fracture toughness of 90 to 97W-NiFe alloys revealing powerful new ductile phase toughening mechanisms. *Acta Materialia*, 186:324–340. <https://doi.org/10.1016/j.actamat.2020.01.012>
- [2.] Haag JV, Edwards DJ, Henager CH, Setyawan W, Wang J, Murayama M (2021) Characterization of ductile phase toughening mechanisms in a hot-rolled tungsten heavy alloy. *Acta Materialia*, 204:116523. <https://doi.org/10.1016/j.actamat.2020.116523>
- [3.] Jiang W, Zhang D, Li D, Heo J, Wang Z, Zhang L, Overman N, Varga T, Hu Z, Wang X, Shao L, Setyawan W (2022) Behavior of helium cavities in ion-irradiated W-Ni-Fe ductile-phase toughened tungsten. *Journal of Nuclear Materials*, 561:153565. <https://doi.org/10.1016/j.jnucmat.2022.153565>
- [4.] Hosemann P (2018) Small-scale mechanical testing on nuclear materials: bridging the experimental length-scale gap. *Scripta Materialia*, 143:161–168. <https://doi.org/10.1016/j.scriptamat.2017.04.026>
- [5.] Chen T, He L, Cullison MH, Hay C, Burns J, Wu Y, Tan L (2020) The correlation between microstructure and nanoindentation property of neutron-irradiated austenitic alloy D9. *Acta Materialia*, 195:433–445. <https://doi.org/10.1016/j.actamat.2020.05.020>
- [6.] Hosemann P, Vieh C, Greco RR, Kabra S, Valdez JA, Cappiello MJ, Maloy SA (2009) Nanoindentation on ion irradiated steels. *Journal of Nuclear Materials*, 389(2):239–247. <https://doi.org/10.1016/j.jnucmat.2009.02.026>
- [7.] Garcia Caraveo AV, Chen T (2022) Application of microcantilever bending tests to local fracture toughness determination in W-Ni-Fe ductile-phase toughened tungsten. *Fusion materials semiannual progress report*, DOE/ER313/73:36–43.
- [8.] Ziegler JF, Ziegler MD, Biersack JP (2010) SRIM – The stopping and range of ions in matter (2010). *Nuclear Instruments and Methods in Physics Research Section B: Beam Interactions with Materials and Atoms*, 268(11–12):1818–1823. <https://doi.org/10.1016/j.nimb.2010.02.091>
- [9.] El-Guebaly LA, Setyawan W, Henager Jr CH, Kurtz RJ, Odette GR (2021) Neutron activation and radiation damage assessment for W-Ni-Fe tungsten heavy alloys with variable Ni content. *Nuclear Materials and Energy*, 29:101092. <https://doi.org/10.1016/j.nme.2021.101092>
- [10.] Haag JV, Olszta MJ, Edwards DJ, Jiang W, Setyawan W (2023) Characterization of boundary precipitation in a heavy ion irradiated tungsten heavy alloy under the simulated fusion environment. *Acta Materialia*, :119059. <https://doi.org/10.1016/j.actamat.2023.119059>
- [11.] Wurster S, Motz C, Pippan R (2012) Characterization of the fracture toughness of micro-sized tungsten single crystal notched specimens. *Philosophical Magazine*, 92(14):1803–1825. <https://doi.org/10.1080/14786435.2012.658449>

- [12.] Cui MH, Shen TL, Zhu HP, Wang J, Cao XZ, Zhang P, Pang LL, Yao CF, Wei KF, Zhu YB, Li BS, Sun JR, Gao N, Gao X, Zhang HP, Sheng YB, Chang HL, He WH, Wang ZG (2017) Vacancy like defects and hardening of tungsten under irradiation with He ions at 800 °C. *Fusion Engineering and Design*, 121:313–318. <https://doi.org/10.1016/j.fusengdes.2017.05.043>
- [13.] Cui M, Shen T, Pang L, Zhu Y, Jin P, Liu C, Fang X, Wang Z (2018) He ion implantation induced He bubbles and hardness in tungsten. *Nuclear Materials and Energy*, 15:232–236. <https://doi.org/10.1016/j.nme.2018.05.004>
- [14.] Gao N, Yao ZW, Lu GH, Deng HQ, Gao F (2021) Mechanisms for interstitial dislocation loops to diffuse in BCC iron. *Nature Communications*, 12(1):225. <https://doi.org/10.1038/s41467-020-20574-6>
- [15.] Weihs TP, Hong S, Bravman JC, Nix WD (1988) Mechanical deflection of cantilever microbeams: A new technique for testing the mechanical properties of thin films. *Journal of Materials Research*, 3(5):931–942. <https://doi.org/10.1557/JMR.1988.0931>
- [16.] Liu X, Athanasiou CE, Padture NP, Sheldon BW, Gao H (2021) Knowledge extraction and transfer in data-driven fracture mechanics. *Proceedings of the National Academy of Sciences*, 118(23):e2104765118. <https://doi.org/10.1073/pnas.2104765118>
- [17.] Alfreider M, Kozic D, Kolednik O, Kiener D (2018) In-situ elastic-plastic fracture mechanics on the microscale by means of continuous dynamical testing. *Materials & Design*, 148:177–187. <https://doi.org/10.1016/j.matdes.2018.03.051>

4.5 SECONDARY ION MASS SPECTROMETRY ANALYSIS OF SINGLE CRYSTAL AND IRRADIATED TUNGSTEN SAMPLES—G. Parker (University of Illinois Chicago), T. Misicko (Louisiana Tech University), X-Y. Yu (Oak Ridge National Laboratory)

OBJECTIVE

Tungsten (W) is the leading choice for plasma facing components (PFCs) which can withstand high temperature and neutron bombardment from nuclear reactors. Single crystal tungsten (SCW), namely irradiated tungsten unshielded (W18) and irradiated tungsten shielded (TE01), were chosen to understand the transmutation effects. Time-of-flight secondary ion mass spectrometry (ToF-SIMS) is used to perform surface analysis and depth profiling of each sample, from surface to two micrometers. Depth profiling is important in observing transmutation effects because tungsten easily oxidizes in air. We used reconstructed mass spectra from ToF-SIMS depth profiling to remove the surface oxidation induced interferences in the presented findings.

SUMMARY

The SCW coupons provide reference ToF-SIMS spectra as a control. Both the TE01 and W18 irradiated samples show transmutation effects as rhenium, rhenium oxides, osmium, and osmium oxides are present in reconstructed SIMS spectra. The W18 sample was irradiated at a temperature of 700°C, while the TE01 sample was irradiated at 753°C. The neutron fluence was consistently maintained at a level of $2.2\text{-}3.5 \times 10^{25}$ n/m² (equivalent to 0.6-0.7 dpa). All samples observed a purity of W exceeding 99.99 wt.%.

PROGRESS AND STATUS

Figures 1 – 3 depict reconstructed ToF-SIMS spectra from depth profiling of the unirradiated SCW, unshielded SCW (W18) and shielded SCW (E01), respectively in the position ion mode. The SCW control coupon shows tungsten isotopic distribution patterns consistent with findings in literature (Figure 1). The ToF-SIMS spectral analysis of SCW showed pristine W isotope signals and the accompanying clusters of W₂⁺ and W₃⁺, respectively.

Unlike the pristine SCW, many transmutation products are observed in collected spectra of irradiated W (Figures 2 – 3). The irradiated SCW spectra both show Re⁺, Os⁺, ReO⁺, and OsO⁺ among others, indicating observations of transmutation products due to neutron irradiation of W.

Shielding provided a layer of protection for the TE01 sample compared to the W18 unshielded SCW. Also, fewer transmutation products are present in the shielded sample. However, W and its accompanying clusters are still observed.

The CsM⁺ ions can also be used as the basis for quantitative measurements of metal ions. Interestingly, CsM⁺ ions, such as CsW⁺ ions, were observed in high intensity in the W18 unshielded sample. In contrast, the CsW⁺ ion intensity is lower in the TE01 spectrum. This finding indicates reduced transmutation product variety with lower quantity in the shielded SCW.

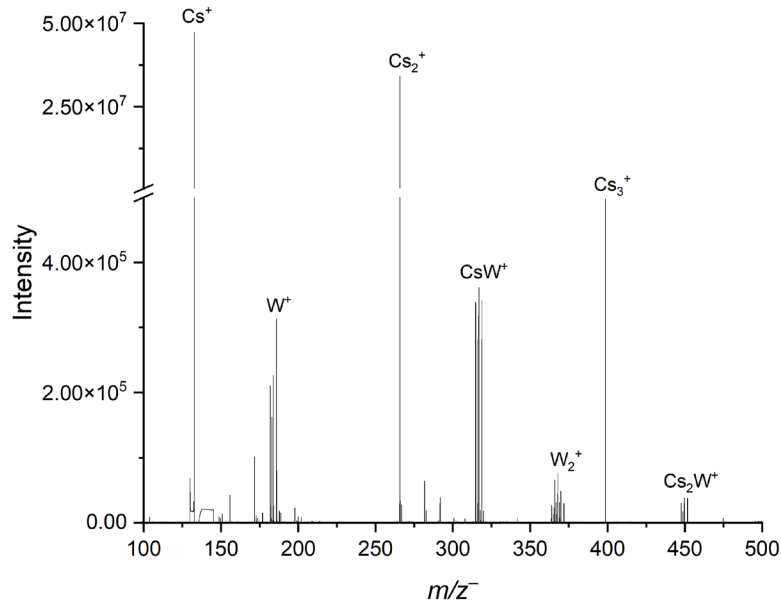


Figure 1. The SCW control coupon shows tungsten isotopic distribution patterns consistent with findings in literature.

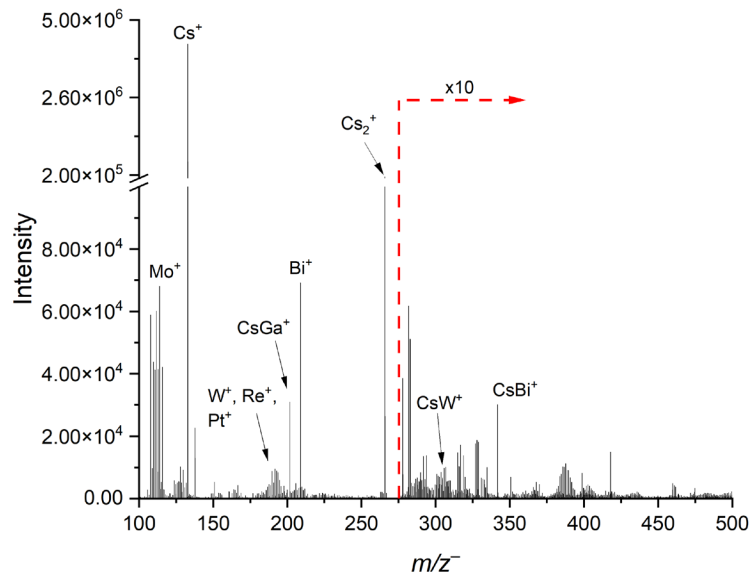


Figure 2. Irradiated SCW un-shielded (W18) shows transmutation products in ToF-SIMS spectrum reconstructed from depth profiling.

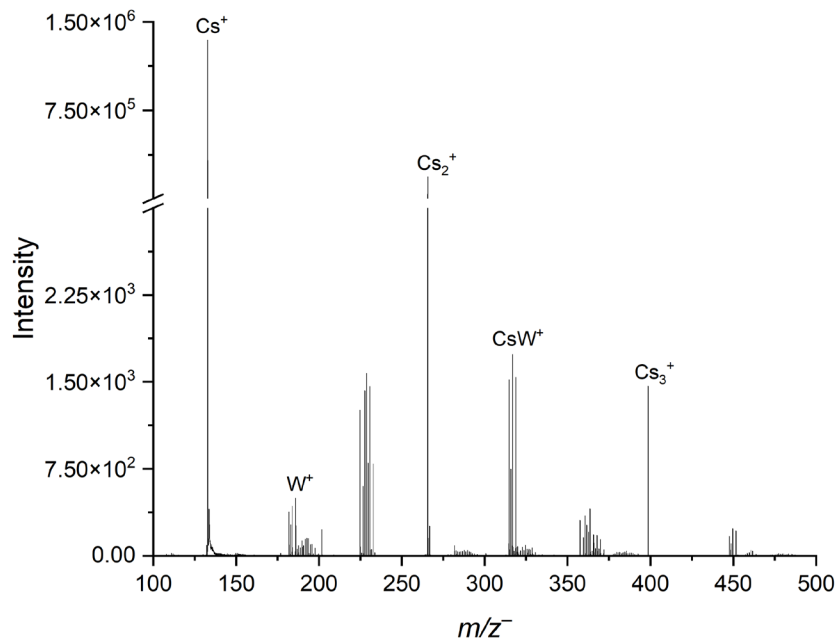


Figure 3. Irradiated SCW with shielding (TE01) shows some transmutation products in ToF-SIMS spectrum reconstructed from depth profiling.

Results

Continued analysis of transmutation products observed of shielded or unshielded SCW coupons is currently underway. Depth profiling analysis via ToF-SIMS is effective to identify neutron penetration based on observed transmutation products into the bulk of the samples and reveal differences in transmutation products. A manuscript reporting key peak identification and reference ToF-SIMS spectra of unirradiated and irradiated SCW will be submitted in the fall of 2024.

4.6 QUANTITATIVE ASSESSMENT OF Ni⁺ AND He⁺ ION IRRADIATION DAMAGE IN A TUNGSTEN HEAVY ALLOY UNDER THE SIMULATED NUCLEAR FUSION ENVIRONMENT—J. V. Haag IV, B. Matthews, M. Olszta, W. Jiang, D. Edwards, Y. Fu, W. Setyawan (Pacific Northwest National Laboratory)

PROGRESS AND STATUS

This reporting cycle, a manuscript has been prepared for publication with the same title as this report discussing the performance of an as-sintered 90W-7Ni-3Fe (wt.%) under high temperature (700°C) sequential Ni⁺ and He⁺ irradiation. This work focuses on the characterization of cavity type defects in an irradiated tungsten heavy alloy (WHA) exposed to conditions mimicking five years of service in a fusion reactor. Prior reporting periods have identified the formation of irradiation induced/assisted nanoscale carbides selectively at the interphase boundary sites between the W and Ni-Fe-W ductile phases under these conditions, presumably due to carbon impurities introduced during the ion irradiations, and these findings have been recently published [1]. This carbide formation is determined to be concerning for the retention of boundary cohesion in these materials as their formation is noted to lead to a deterioration of bulk mechanical properties. However, the extent of this carbide formation plus that of the irradiation damage has not yet been elucidated.

This work extends the ongoing Pacific Northwest National Laboratory (PNNL) effort in understanding WHA performance under fusion relevant conditions by producing a quantitative understanding of cavity formation in these dual-phase alloy systems. The key takeaways from this work include: the identification of large, faceted cavities in the Ni-Fe-W phase and small spherical bubbles in W. This can be readily viewed in the high angle annular dark field (HAADF) scanning transmission electron microscope (STEM) images in Figure 1 below. These defects are quantitatively assessed to derive an average cavity size and number density as well as a peak void swelling value (in %). The W phase was noted to possess a peak swelling value of ~0.45% at a depth of 225-250nm and the Ni-Fe-W a peak swelling of ~1.41% at a depth of 300-350nm. Due to the small size scale and high density of cavities in the W phase, further analysis is currently being performed to improve the accuracy of cavity identification and measurement, therefore the W swelling results are subject to change. All effort has been made in the collection of this data to produce experimental swelling measurements which provide adequate detail to inform modelling efforts on site-specific damage evolution. To maintain sensitivity to the surface-localized nature of ion-irradiation damage in these alloys, the characteristic damage in both phases has been tracked as a function of depth, and the peak damage value is derived experimentally and can then be compared to Stopping and Range of Ions in Matter (SRIM) predictions. These swelling values are then compared to existing literature on the high temperature irradiation effects studies in pure W, pure Ni, and Ni alloys; revealing that the Ni-Fe-W ductile phase appears to swell less severely than pure Ni under similar conditions.

As WHAs are, by nature, dual-phase alloy systems, it is also necessary to observe and quantify the accumulation of defects at the interphase boundaries between the W and Ni-Fe-W phases, like that shown in Figure 2. Preliminary work in prior reporting cycles has identified potential preferential segregation of cavities along the interphase boundaries, primarily lying along the Ni-Fe-W side of the boundary. This phenomenon is investigated in further detail in this study and is attributed to the higher degree of defect mobility in the Ni-Fe-W phase over that of W due to its comparatively low melt temperature. The increased defect mobility allows a greater degree of damage trapping at the interphase boundaries and therefore preferential cavity accumulation at these sink sites. While a single static image of the boundary, like that in Figure 2, suggests a high density of cavities lying along the interface boundary, it is now necessary to develop a more quantitative understanding of site-specific damage evolution in WHA systems. To quantitatively characterize the extent of this cavity segregation along interphase boundary planes, a multi-projection feature identification approach has been applied. A region of interest is imaged in STEM mode across a large angular range, collecting a tilt series dataset. This technique allows for higher fidelity feature tracking and deconvolution of projection effects from the TEM foil, and superior cavity identification. The individual location, morphology, and overall density of features can be characterized, and this work has produced the first available quantitative sense of damage accumulation at these key sites for material performance. To do this, an 'areal coverage' value of cavity contact along a 2D boundary plane is derived,

analogous to a volumetric swelling in 3D, and is used to express the extent of cavity segregation along specific boundaries. The extent of the cavity areal coverage was derived to be ~11.8% in this work. These results point towards the need for micromechanical testing of these irradiated materials to understand the effects of cavity segregation on boundary cohesion, and thereby determine the embrittlement effect the applied irradiation conditions have upon the bulk mechanical behavior of WHA systems.

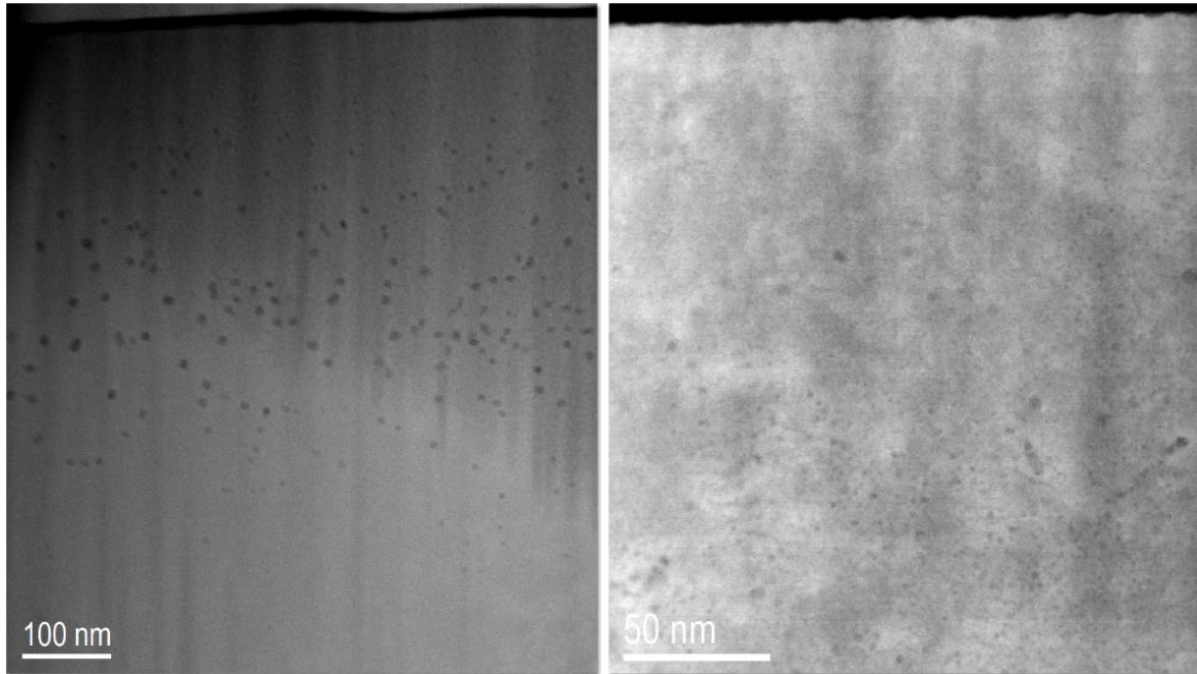


Figure 1. The HAADF STEM micrographs of (left) Ni-Fe-W ductile phase, and (right) W phase in a 700°C Ni⁺ and He⁺ irradiated WHA.

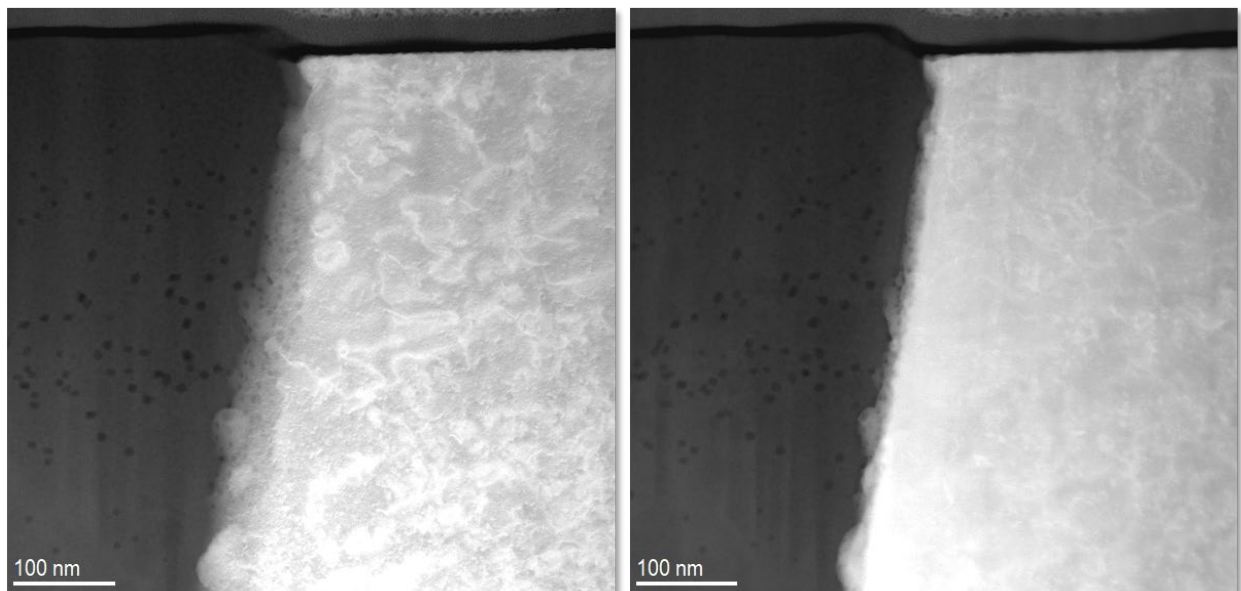


Figure 2. The HAADF STEM micrographs from the same interphase boundary region taken at two different orientations.

Acknowledgements

This research was supported by the U.S. Department of Energy (US DOE), Office of Science, Office of Fusion Energy Sciences, through Contract No. AT2030110-13784 and was performed at the PNNL, which is operated by Battelle for the US DOE under Contract No. DE-AC05-76RL0-1830.

References

- [1] J.V. Haag IV, M.J. Olszta, D.J. Edwards, W. Jiang, W. Setyawan, Characterization of boundary precipitation in a heavy ion irradiated tungsten heavy alloy under the simulated fusion environment, *Acta Materialia*, V. 274, Aug. 2024, <https://doi.org/10.1016/j.actamat.2023.119059>.

4.7 FLASH POLISHING TECHNIQUES ON TUNGSTEN FOR TRANSMISSION ELECTRON MICROSCOPY OBSERVATION—W. Zhong, Y. Lin, S. Calzada (Oak Ridge National Laboratory)

OBJECTIVE

Focused ion beam (FIB) is commonly used to prepare electron transparent samples for transmission electron microscopy (TEM) characterization. However, the ion milling using kilovolt gallium ions generates artifacts in TEM samples that could affect data analysis and interpretation. The goal of this work is to develop flash polishing techniques for W to reduce FIB artifact for TEM observation.

SUMMARY

A flash polishing recipe was developed for tungsten in this work. Artifact-free samples were successfully prepared using a combination of FIB and flash polishing techniques for unirradiated tungsten using the 1%NaOH solution. However, the same recipe proved unsuitable for irradiated tungsten, necessitating adjustments in voltage and etching time. An improved recipe was identified for irradiated tungsten, though further refinements may be needed to completely eliminate polishing artifacts.

PROGRESS AND STATUS

The FIB was used to prepare a thin lamella of tungsten samples with a specific thickness for subsequent flash polishing. Several recipes were tested, varying the voltage from 13 V to 25 V and the etching time from 1 ms to 50 ms to determine the most suitable parameters for effectively removing FIB-induced artifacts. Flash polishing was performed at room temperature using a 1%NaOH solution mixed with demineralized water. After flash polishing, the samples underwent a sequential cleaning process in deionized water, ethanol, acetone and then ethanol, with each step lasting 1 minute.

For unirradiated tungsten, tungsten sample with the thickness of 200 nm was prepared by FIB before the flash polish. Figure 1 shows the Scanning/transmission electron microscopy (STEM) bright field (BF) image of the tungsten samples after the flash polishing using 18 V for 1 ms. Most of the FIB artifacts were removed from flash polishing. Dislocation lines are clearly observed in the BF images with negligible FIB-induced artifact.

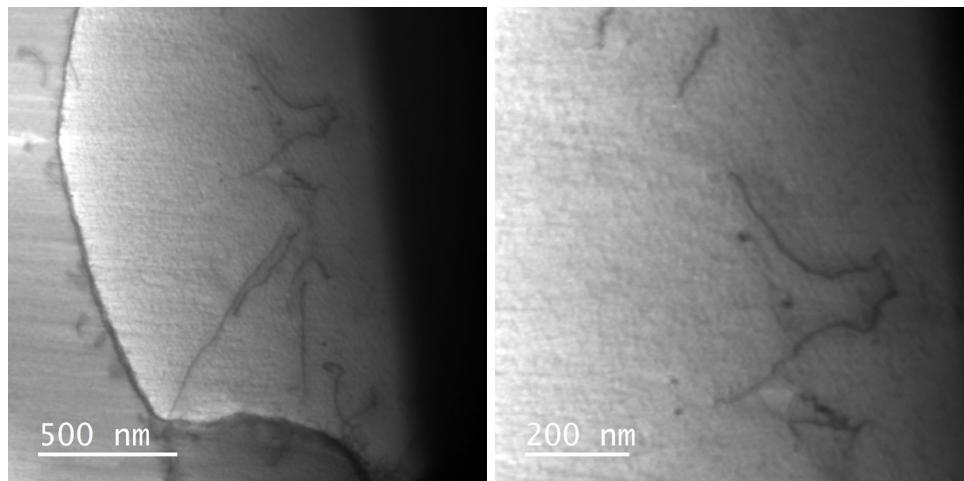


Figure 1. The STEM BF image of unirradiated pure W after flash polishing.

The flash polishing recipe developed for unirradiated tungsten is not suitable for irradiated tungsten, possibly due to the production of transmutation elements (such as Re and Os) or irradiation-induced defect formation. Figure 2 shows the microstructure of irradiated tungsten after using the same flash polishing

parameters of 18 V for 1 ms. Small holes are visible within the samples, suggesting non-homogeneous etching using the same recipe.

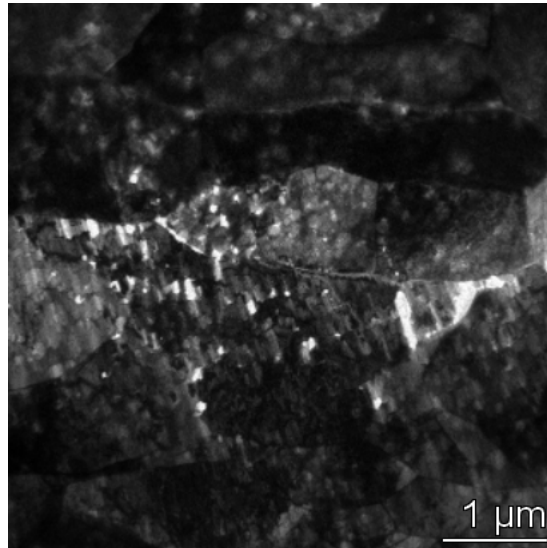


Figure 2. The STEM BF image of irradiated W after flash polishing with 18 V for 1 ms.

The recipe for flash polishing irradiated tungsten samples was adjusted to improve the results. The voltage was set at 19 V, and a lamella with a thicker sample of approximately 600 nm was prepared for polishing. The flash polishing time was carefully controlled between 4-5 ms. Figure 3 shows a STEM BF image of irradiated tungsten polished with the revised recipe, revealing dislocation networks and Re/Os-rich precipitates. Although FIB artifacts are significantly reduced, small dots are still observed, potentially due to insufficient cleaning or the need for further optimization of the recipe.

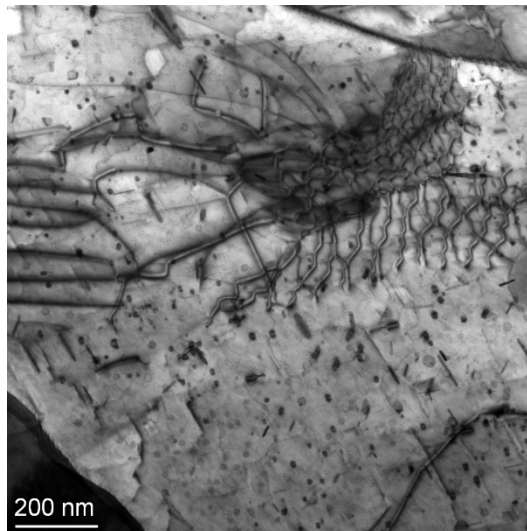


Figure 3. The STEM BF image of irradiated W after flash polishing with 19V for 4 ms.

Results

Irradiation induced defects and precipitate/cluster will be characterized on the flash polished samples.

5. HYDROGEN AND HELIUM EFFECTS

No contributions this reporting period.

6. FUSION CORROSION AND COMPATIBILITY SCIENCE

6.1 COMPATIBILITY of WELDED CNA in EUTECTIC PbLi and DEVELOPMENT SLURRY ALUMINIDE COATINGS on FERRITIC and AUSTENITIC STEELS—M. Romedenne, C. De Lamater-Brotherton, W. Tang, B. Armstrong, Y. Zhang, B. Pint (Oak Ridge National Laboratory)

OBJECTIVE

The objective is to evaluate the compatibility of welded CNA in eutectic PbLi and to develop slurry aluminides coatings to enhance the compatibility of steels with eutectic PbLi at 600°C. The tensile properties of welded and post weld heat treated (PWHT) CNA were studied after exposure to static eutectic PbLi. In parallel, slurry aluminide coatings are being developed and evaluated to improve the compatibility of large scale and complex shape structural components in eutectic PbLi at 600-650°C. Heat treatments are being optimized to determine the most appropriate coating thickness and Al surface concentration in terms of PbLi compatibility.

SUMMARY

Welded CNA steel after PWHT which included normalization and tempering were exposed to eutectic PbLi for 1000 h at 600°C using small scale (SS3 type) tensile specimens to determine if there was any impact of welding on PbLi compatibility. Room temperature tensile properties were measured after exposure. In addition, ferritic martensitic T91 steel and 316H coupons were coated using an Al and Si-rich slurry. Specimens were subsequently heat-treated at 950, 1050 and 1100°C in inert argon atmosphere for 2 h using quartz ampoules. Initial microstructural characterization identified diffusion of Al into the substrate specimens for up to 100 µm with the formation of various intermetallic phases in the case of 316H.

PROGRESS AND STATUS

Introduction

Commercial fusion energy has a vital need to experimentally validate many of the proposed designs of the breeding blanket structures. The Dual Coolant Lead Lithium (DCLL) has been proposed to be made of Reduced Activation Ferritic Martensitic (RAFM) structural steel self-cooled with liquid eutectic Pb-Li and is planned to operate at maximum temperatures of 550-600°C [1]. At these temperatures, compatibility of RAFM steel with eutectic PbLi can pose some issues related to plugging [2,3], mass transfer between RAFM and SiC flow channel inserts [4] as well as mass transport of non-radioactive and radioactive impurities [5]. To enhance the compatibility of RAFM steels in eutectic PbLi, pack-aluminized coatings have been developed and shown to mitigate mass transfer between Fe-based alloys and SiC for up to 2000 h at 650°C [6-8]. However, pack aluminides coatings cannot be easily implemented on large components of complex geometry in contrast with slurry aluminides which are being explored in this study. Previous flowing experiments were conducted using commercial pre-oxidized FeCrAlMo tubing (Kanthal alloy APMT). To move away from that material for future natural and forced convection experiments, coated steel tubing is needed of both FM and austenitic steels.

In addition, these steels will need to be joined. In the colder section of the flow path, coatings may not be required but the performance of joints needs to be investigated. There is currently no literature relative to the compatibility of welded CNA in eutectic PbLi hence static testing has been initiated to fill that gap.

Experimental Procedure

A gas tungsten arc weld was made using CNA welding wire (composition in Table 1) on a CNA plate (composition in Table 1). After welding the plate with the weld was post weld heat treated (normalized and tempered) [9]. The SS3 specimens (25.4 mm total length, 0.76 mm thickness, 7.62 mm gauge length, and 1.52 mm gauge width) of CNA (composition in Table 1) were machined with a weld at the center of the specimen gauge area (Figure 1) and away from the weld (Figure 1) and exposed in static eutectic PbLi for 1000 h at 600°C in Mo capsules (two SS3 specimens per capsule). Specimens extracted away from the weld could be considered as the base metal specimens. After exposure the specimens were cleaned using the standard [1:1:1] solution of acetic acid, ethanol and hydrogen peroxide and were tensile tested post exposure at room temperature with a Instron 1125 machine per ASTM E8-13 standard testing procedures with a strain rate of 0.015 min⁻¹.

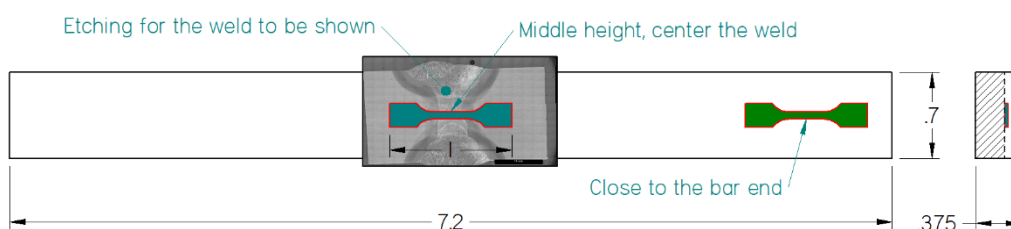


Figure 1. Locations of machined tensile specimens over the etched weld (blue) and away from the weld (green). Unit: in.

Coupons of ferritic martensitic alloy T91 and austenitic type 316H steels (compositions reported in Table 1) were slurry dipped coated in Al and Si-rich slurry (LSR Sialoy H₂O [46Al - 40H₂O - 20PUD - 7Si]). The specimens were dipped twice, and heat treated in argon inert atmosphere at 950, 1050 and 1100°C in quartz ampoules. Specimens were sectioned, Cu-plated and mounted in conductive epoxy as cross sections and polished to 1 μm finish for microstructural characterization. Specimens were observed using secondary electron (SE) and backscattered electron (BSE) imaging using a scanning electron microscope (ZEISS Gemini 460 SEM) equipped with energy dispersive X-ray spectroscopy (EDS) that was used for line scans and elemental maps.

Table1. Alloys chemical composition analyzed by inductively coupled plasma atomic emission spectroscopy, combustion for carbon and inert gas fusion for nitrogen

Wt.%	Fe	Cr	Ni	Mo	Al	Mn	Si	C	Ta	Ti	W	N	Nb
CNA (rod and welding wire)	Base	8.7	<0.01	-	-	0.50	0.16	0.12	0.06	0.12	1.27	0.002	-
CNA plate	Base	8.77	-	-	-	0.57	0.10	0.09	0.05	0.13	1.46	Not known	-
316H	Base	17.2	13.2	2.3	-	1.9	0.5	0.06	-	-	-	-	-
T91	Base	8.631	0.325	0.9	-	0.46	0.35	0.1	-	-	-	-	0.06
F82H	Base	8.1	0.06	-	-	0.45	0.08	0.10	0.09	-	1.8	0.01	-

Results

After liquid metal exposures, specimens are usually weighed to determine mass change. However, in current experiments the specimens were welded to the holder and mass change could not be measured. Room temperature tensile properties were compared to base CNA rod in the normalized and tempered condition before exposure and after 1000 h in eutectic PbLi at 600°C (Figure 2). The Ultimate Tensile Strength (UTS) and 0.2% Yield Strength (0.2YS) of the base and welded CNA were similar after exposure to PbLi (UTS of 636 ± 3 and 629 ± 2 MPa in Figure 2) and were lower than the base CNA (UTS of 804 MPa in Figure 2), while elongation at rupture was similar before and after exposure to eutectic PbLi for base and welded CNA. It is worth to mention that the base metal results without the PbLi exposure were from the heat-treated CNA rod and the base metal results after PbLi exposure were from the CNA plate which was heat treated (normalization and tempering) before and after the welding.

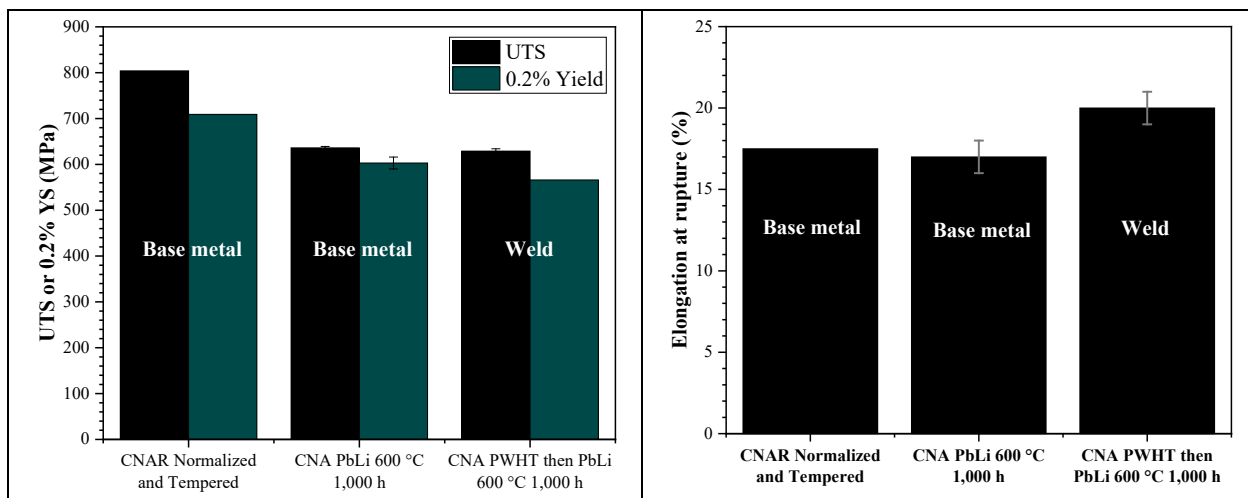


Figure 2. (a) The UTS and 0.2% YS and (b) Elongation at rupture of base and welded CNA before and after exposure to static eutectic PbLi for 1000 h at 600°C, Mo capsule.

The BSE images of coated T91 coupons after heat treatment at various temperatures are reported in Figure 3. After heat treatment, the deposited slurry diffused into the T91 substrate over 60 ± 5 μm , 60 ± 5 μm and 100 ± 5 μm at 950, 1050 and 1100°C respectively (Figure 3).

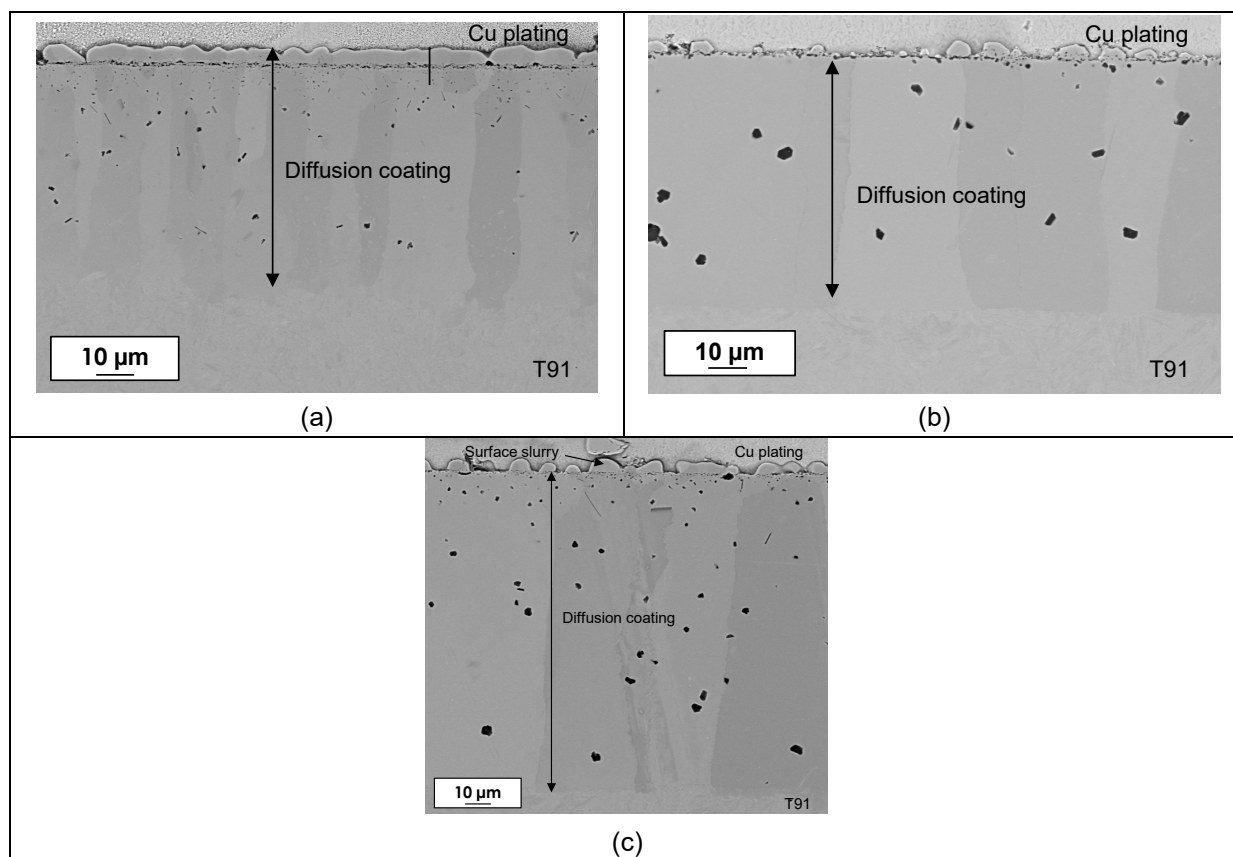


Figure 3. The BSE images of coated T91 specimens after 2 h heat treatment in argon inert atmosphere (quartz ampoule) at (a) 950, (b) 1050 and (c) 1100°C.

Figure 4 shows Al diffusion profiles measured within the coated specimens at the three heat treatment temperatures. The Al surface concentration after heat treatment at 950°C was higher (15 at.% in Figure 4a) than at 1050 and 1100°C (7 at.% in Figure 4a). Surprisingly, the extend of Al diffusion (area under the curve) was twice lower for T91 dipped-coated and heat treated at 1050°C compared to the other two specimens heat treated at 950 and 1100°C (Figure 4a). This suggests that coating process although similar for the three alloys did not result in similar extent of Al diffusion. Previously, the pack aluminized or CVD aluminized ferritic martensitic steel (F82H and Fe-9Cr-2W) specimens had very consistent extent of Al diffusion between specimens and a peak Al content of 35 at.% and a depth of 120 μm for pack-aluminized F82H [6] (pink profile in Figure 4a) and a peak Al content of 18 at.% and a depth of 50 μm for pack aluminized Fe-9Cr2W [10, 11]. Another difference between pack-aluminizing and slurry is diffusion of Si into the alloy in the case of the Si-containing slurry coating (Figure 4b) compared to only Al diffusion in case of pack-aluminized coatings.

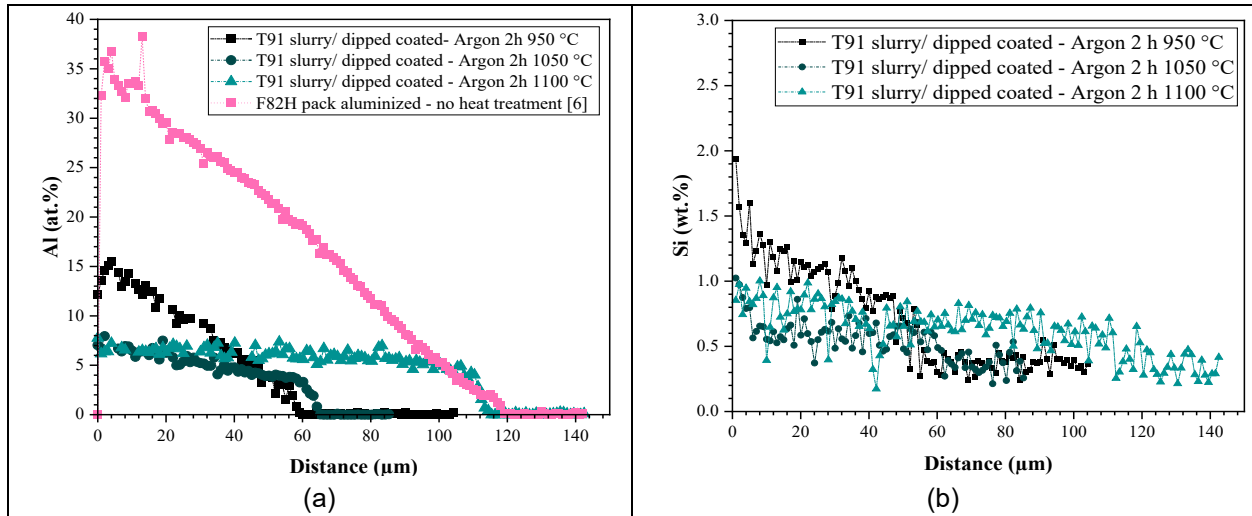


Figure 4. The EDS Al concentration profiles measured within the coated and heat treatment T91 specimens (2h in argon at 950, 1050 and 1100°C, quartz ampoule).

The BSE images of coated 316H coupons after heat treatment at various temperatures are reported in Figure 5. After heat treatment, the deposited slurry diffused into the 316H substrates and larger diffusion depths for heat treatments performed at 1050 and 1100°C were measured compared to 950°C (Figure 5). In addition, intermetallic phases were formed within the substrate (Figure 5).

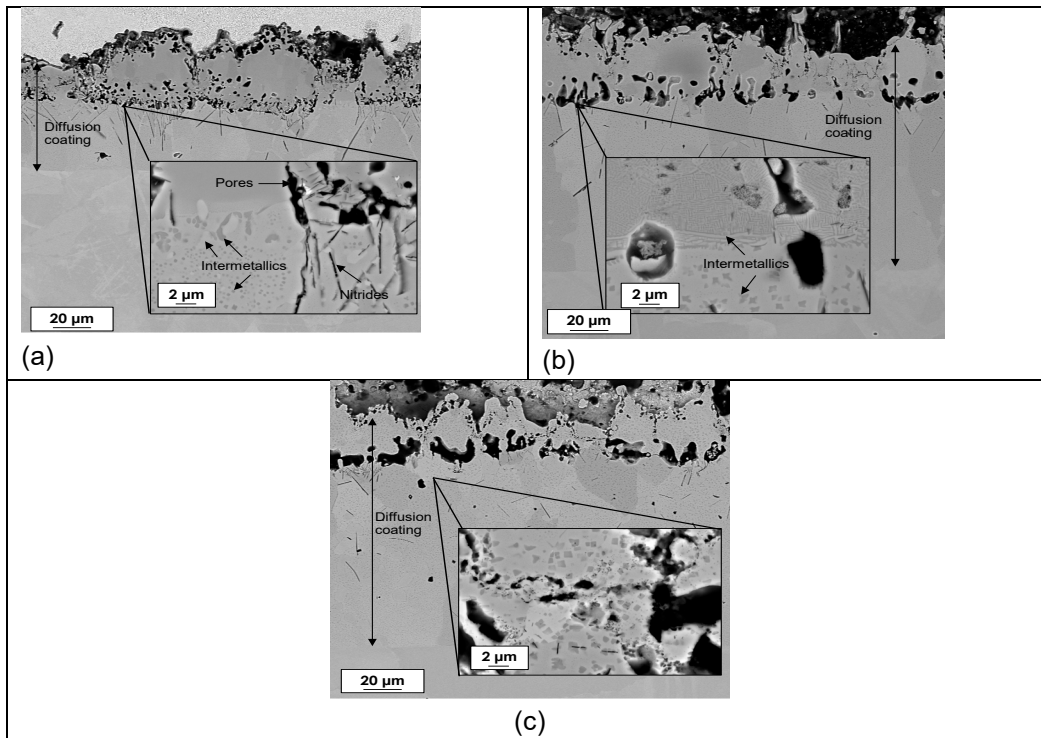


Figure 5. The BSE images of coated 316H specimens after 2 h heat treatment in argon inert atmosphere (quartz ampoule) at (a) 950, (b) 1050 and (c) 1100°C.

Characterization is in progress for the post-exposure welded CNA. Now that reasonably uniform slurry coated specimens have been fabricated, the next step will be exposures in static eutectic PbLi to determine their compatibility. Steel capsules will be coated and exposed to high temperature eutectic PbLi as well to demonstrate the feasibility and compatibility of coated tubes with and without welds.

References

- [1] S. Malang et al., *Fusion Sci. Technol.* 60 (2011) 256.
- [2] W.D. Manly, ORNL-2055 (1958).
- [3] W. Krauss et al., *Fusion Eng. Design* 146 (2019) 1785.
- [4] B. A. Pint, J. Jun and M. Romedenne, *Fusion Eng. Design* 166 (2021) 112389.
- [5] O. K. Chopra et al., *Fusion Technol.* 8 (1985) 1969.
- [6] M. Romedenne, Y. Zhang, Y.-F. Su, B. A. Pint, *J. Nucl. Mater.* 581 (2023) 154465.
- [7] M. Romedenne, C. De Lamater-Brotherton, B. A. Pint, Y. Zhang, DOE/ER-0313/74 (2023) 131.
- [8] M. Romedenne, C. De Lamater-Brotherton, B.A. Pint, Y. Zhang, DOE/ER-0313/75 (2024) 122.
- [9] W. Tang et al., Manuscript in preparation
- [10] B. A. Pint, *J. Nucl. Mater.* 417 (2011) 1195
- [11] B. A. Pint, K. Unocic, *J. Nucl. Mater.* 442 (2013) S572.

7. ADVANCED MANUFACTURING

No contributions this reporting period.

8. MECHANISMS AND ANALYSIS

8.1 DETERMINATION OF FLUORINE DISTRIBUTION IN CrFe ALLOY—G. Parker (University of Illinois Chicago), Y. Li, S. Zinkle (University of Tennessee), X-Y. Yu (Oak Ridge National Laboratory)

OBJECTIVE

Fluorine penetration into manufactured alloys poses a structural deformity. Analysis of an observed fluorine (F) band for a manufactured FeCr alloy was necessary to determine the depth of fluorine penetration. Depth profiles were obtained using the MCs_2^+ in the positive polarity mode using time-of-flight secondary ion mass spectrometry (ToF-SIMS). Three-dimensional (3D) reconstruction and image maps were done using the SurfaceLab software version 7.3 and Igor Pro v9.

SUMMARY

Two heat treated and ion irradiated FeCr alloy coupons were compared against a control sample that was neither heat treated, nor ion irradiated. Chosen temperatures for heat treatment were 250°C and 350°C. We observe that fluorine dissipation in the heat-treated sample. We use the CsM^+ method to show fluorine distributions in two-dimensional (2D) and 3D space of these alloys.

PROGRESS AND STATUS

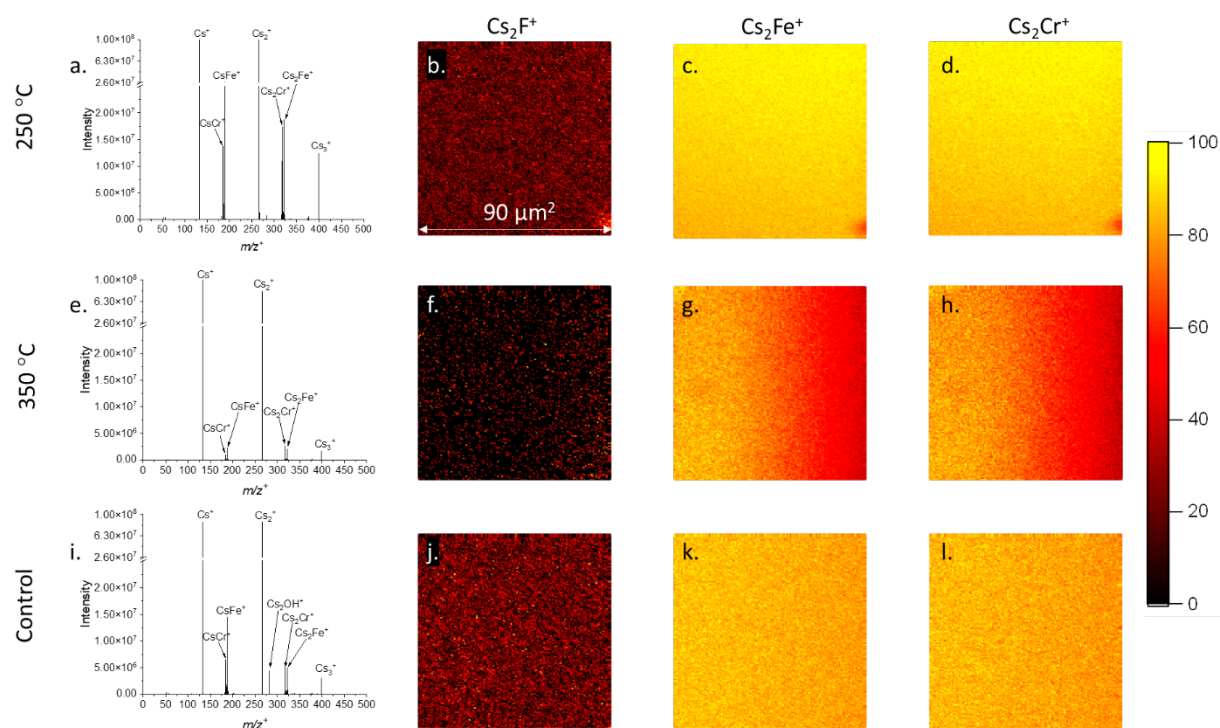


Figure 1. The ToF-SIMS spectra and 2D images of FeCr alloys of fluorine distributions in the 250°C and 350°C treated samples and control.

The unbound fluorine (F^+ , m/z^+ 19.0387) signal could give improper determination to F within the bulk of the sample due to possible matrix effect in SIMS spectra. The MCs_2^+ is a method used in SIMS to detect orders of magnitudes higher for a given analyte not readily observed in its elemental form [1-3]. Figure 1 depicts the SIMS results of three specimens, two FeCr coupons treated at 250°C and 350°C as well as a pristine FeCr coupon, respectively. The FeCr control (Figure 1i) shows some surface oxidation demonstrated by the large Cs_2OH^+ peak observed within the spectra. Observed spectral features show a

reduction in ion intensity for Cs_2Cr^+ and Cs_2Fe^+ from 250°C (Figure 1a) to 350°C (Figure 1e). This drop in signal is likely due to the non-optimized extraction cone height as the mounted sample had interference from copper tape. The SIMS 2D images show the relative abundance of Cs_2F^+ , Cs_2Fe^+ , and Cs_2Cr^+ for the 250°C (Figures 1b – 1d), 350°C (Figures 1f – 1h), and control (Figures 1j – 1l) samples, respectively. This result demonstrates that F decreases as the temperature increases while maintaining high chromium and iron ions within the alloy as expected.

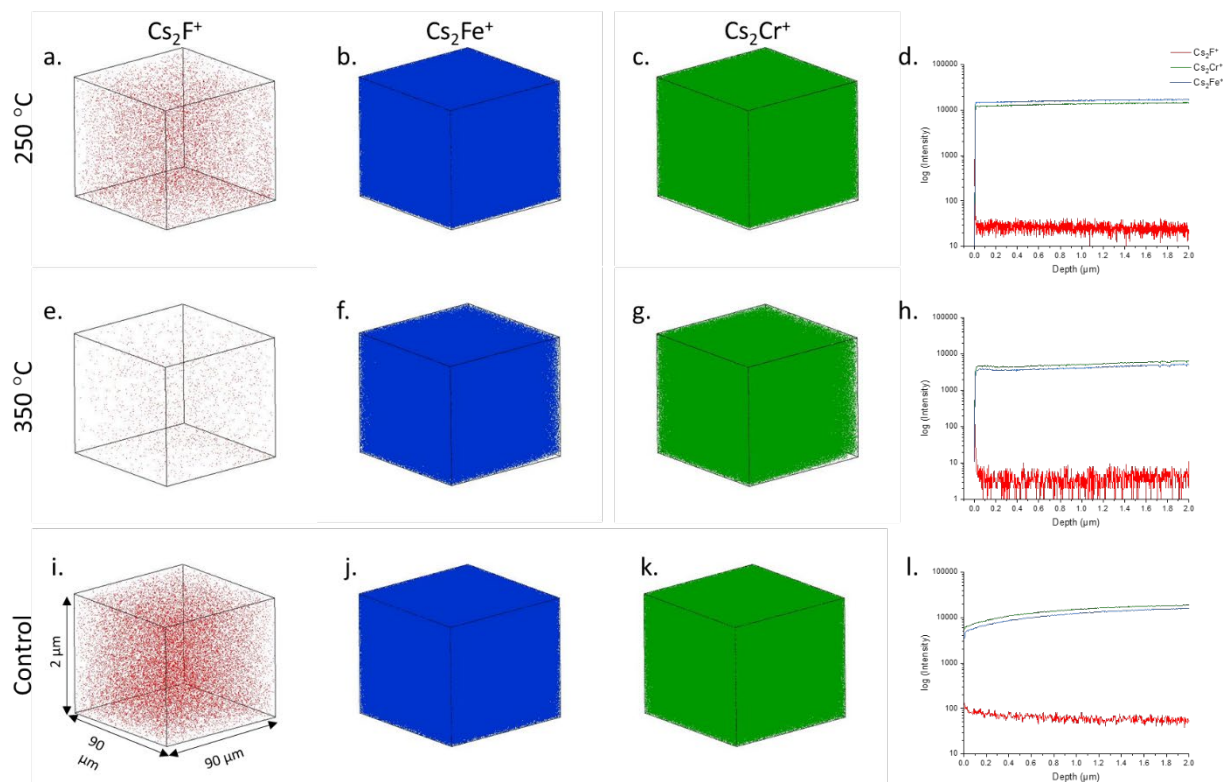


Figure 2. The ToF-SIMS 3D images and depth profiles of fluorine distributions of the FeCr alloys.

Figure 2 shows the 3D reconstruction of the MCs_2^+ peaks for the three coupons as well as the depth profiles for each sample. Figure 2l demonstrates that it takes until 2.0 μm (or 4000 s) before the depth profile begins to even out where elemental Cr and Fe are stabilized (Figure 2l). This effect is most likely due to the oxide layer that had built up on the surface, which also contributes to the rise in F signal when comparing the 250°C and 350°C samples. The Cs_2F^+ ion is used to determine the F^+ ions. Depth profiles at 250°C (Figure 2d) and 350°C (Figure 2h) show F signals close to the SIMS detection limit. The 350°C sample has lower Cs_2F^+ signal than the 250°C sample. Heating the sample to a higher temperature may have removed fluorine. Also, the total ion intensity in the 350°C treated sample is about 1/8 of the 250°C sample, because the former sample had a metal tape that precluded better geometry of data acquisition.

Results

Data and analysis provided demonstrate the need for heat treatment of manufactured alloys to prevent unwanted contaminants from infiltrating the material. Results will be included in a manuscript being prepared for submission in the Fall of 2024.

References

- [1.] Gnaser, H. and H. Oechsner, The influence of polarizability on the emission of sputtered molecular ions. *Surface Science*, 1994. 302(1): p. L289-L292.
- [2.] Saha, B., et al., Secondary emission of MC_n^+ molecular ions under the joint influence of electropositive and electronegative elements. *Surface Science*, 2008. 602(5): p. 1061-1065.
- [3.] Marseilhan, D., et al., Quantification of SiGe layer composition using MC_s^+ and MC_{s2}^+ secondary ions in ToF-SIMS and magnetic SIMS. *Applied Surface Science*, 2008. 255(4): p. 1412-1414.

8.2 THE ROLE OF STACKING FAULT TETRAHEDRA ON VOID SWELLING IN IRRADIATED COPPER—Y. Lin, M. Zachman, (Oak Ridge National Laboratory), S. Zinkle, Z. Yu, H. Xu (University of Tennessee)

Extended Abstract: Full manuscript Published in Communications Materials
(<https://doi.org/10.1038/s43246-024-00491-7>)

OBJECTIVE

The objective of this study is to investigate and understand the underlying mechanism behind the significant difference in void swelling behavior between face-centered cubic (fcc, 1 % dpa⁻¹) and body-centered cubic (bcc, 0.2 % dpa⁻¹) irradiated structural materials.

SUMMARY

A long-standing and critical issue in the field of irradiated structural materials is that void swelling is significantly higher in fcc-structured materials (1% dpa⁻¹) as compared to that of bcc-structured materials (0.2% dpa⁻¹).

PROGRESS AND STATUS

Despite extensive research, the underlying mechanism of the difference in swelling resistance between these two types of materials is not yet fully understood. Here, by combining atomistic simulations and Scanning Transmission Electron Microscopy (STEM) imaging, we find stacking fault tetrahedra (SFTs) are the primary cause of the high swelling rate in pure fcc copper. We reveal that SFTs in fcc copper are not neutral sinks, different from the conventional knowledge. On the contrary, they are highly biased compared to other types of sinks because of the SFT-point defect interaction mechanism. The SFTs show strong absorption of mobile self-interstitial atoms (SIAs) from the faces and vertices, and weak absorption of mobile vacancies from the edges. We compare the predicted swelling rates with experimental findings under varying conditions, demonstrating the distinct contributions of each type of sink. These findings will contribute to understanding the swelling of irradiated structural materials, which may facilitate the design of materials with high swelling resistance.

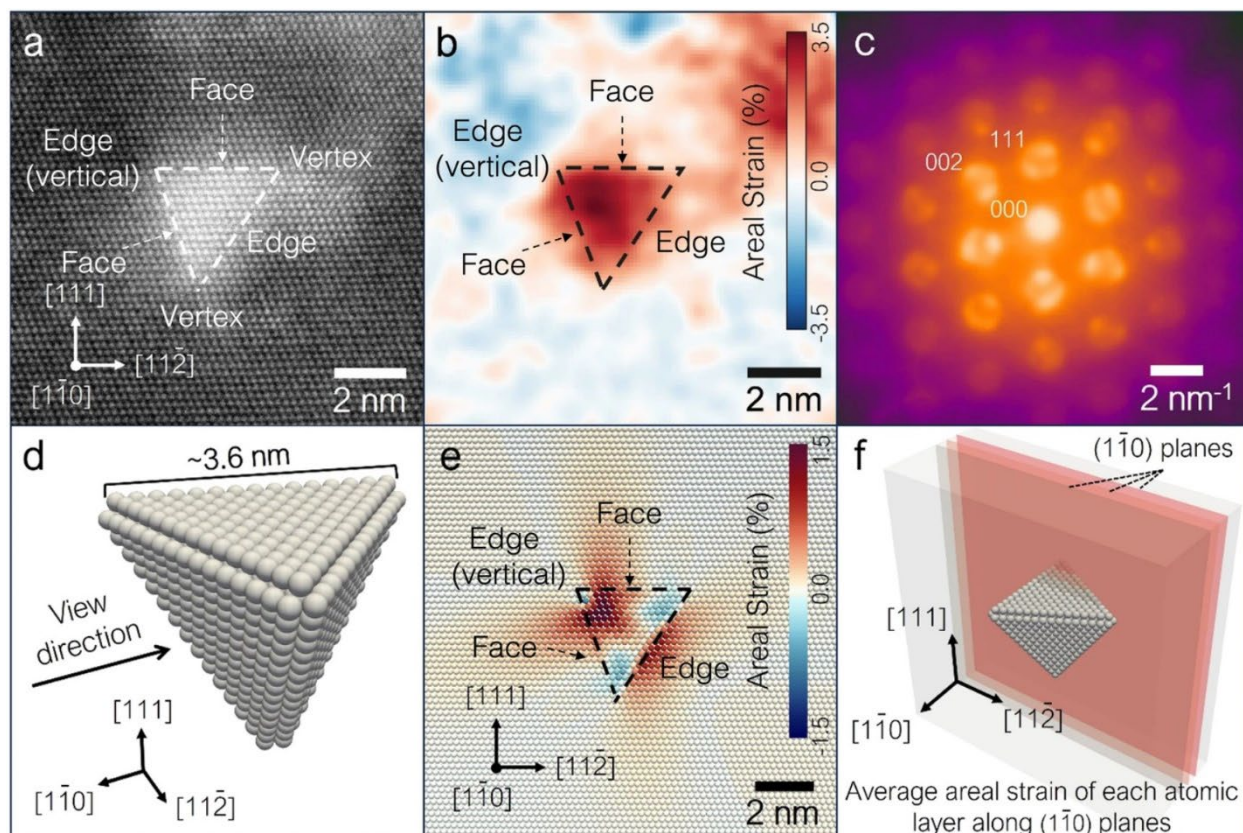


Figure 1. (a) Atomic-resolution Low-angle annular dark-field (LAADF)-STEM image of an SFT in dual-ion-irradiated Cu at 440°C to 30 dpa and 48 appm He. (b) Areal strain perpendicular to the beam direction measured by 4D-STEM exit wave power cepstrum (EWPC) method. (c) Average convergent-beam electron diffraction (CBED) pattern in the region of the SFT. (d) Crystal structure of the SFT used for simulation calculation. (e) Areal strain averaged over the SFT strain field in the $[1\bar{1}0]$ direction. The f Schematic diagram of the areal strain averaging method used for the simulated results. Faces, edges, and vertices of the SFT are labeled in (a), (b), and (e) for comparison with Figure 1. Notice that the Edge (vertical) refers to an edge that is vertical to the view plane, and the labels for vertices in (b) and (e) are hidden for a clearer view.

Results

Additional work using the same method is planned to study other irradiation induced defects in different materials.

9. MODELING AND COMPUTATIONAL STUDIES

9.1 MECHANISMS OF MOBILITY OF GRAIN BOUNDARIES IN TUNGSTEN—R. Moore (Lehigh University), T. Frolov, R. Rudd (Lawrence Livermore National Laboratory)

OBJECTIVE

The objective of this study is to assess the mechanical robustness of tungsten in first-wall applications for tokamaks. These applications unavoidably involve the challenges of high temperature and radiation damage. Here we report progress on determining the mechanisms governing the mobility of tungsten grain boundaries at high temperature, a key property in the process of recrystallization. The determination of mechanisms enables predictive analytic models of grain boundary response to driving forces like the energy stored in the damaged metal lattice that is released as a grain boundary sweeps through it. In prior work we studied tungsten grain boundary properties such as the energies of boundaries with various orientations and misorientations, including energies of grain boundaries whose high-temperature structure differs from the structure at ambient conditions. We have calculated properties associated with the grain boundary mobility including the response of grain boundaries to applied shear stress. We have also developed methods for direct calculation of the motion of curved grain boundaries at high temperature using molecular dynamics. Here we again utilize molecular dynamics simulation of grain boundary motion and go further to analyze how the defect content in a grain boundary evolves as the boundary moves under the action of a driving force.

SUMMARY

Magnetic fusion energy first-wall applications need materials that can withstand high thermal and radiation fluxes including the accumulation of hydrogen isotopes and helium and the microstructural changes they induce. Generally, the desired materials have a high melting temperature, mechanical strength at elevated temperatures, fracture toughness and acceptable activation levels even under exposure to radiation, high thermal conductivity, and resistance to surface sputtering [1]. Tungsten is a refractory metal that possesses many of these qualities, but it is prone to undesirable recrystallization and embrittlement that can cause first-wall failure. Recrystallization involves changes to the grain microstructure in which stress-free grains nucleate through the motion of grain boundaries, a motion driven by the reduction of associated free energies as lattice defects are swept up by the grain boundary. Grain boundary structure affects how the boundary responds to those driving forces, as described by the mobility. In addition to vacancies and interstitials inducing local defects in a grain boundary, boundaries can reconstruct more globally due to grain boundary phase transitions [2]. The phase affects various grain boundary properties.

PROGRESS AND STATUS

The conventional theory of grain boundary structure assumes that the energy of the boundary is uniquely determined by its misorientation (relative orientation of the two abutting grains) and orientation (angle at which the boundary cuts through the grain), up to some defect content which could raise its energy. Computational work in the past decade or so predicted grain boundary phase transformations where a grain boundary with fixed orientation and misorientation changes structure non-incrementally in a first order transformation [2], a prediction confirmed in recent experiments using high-resolution transmission electron microscopy [3].

Computational techniques to predict grain boundary phases have been developed for face-centered cubic (fcc) metals [4, 5] and body-centered cubic (bcc) metals including tungsten [6-9]. Grain boundary phase transformations involve nucleation and growth of the daughter phase [9] and may result in composite or mosaic grain boundary structures [10]. Initial studies of the physical consequences of these phase transformations focused on properties like grain boundary diffusion [2]. The phase transformations can affect the way grain boundaries respond to forces, as well. A recent initial study of the grain boundary mobility showed that the effect could be significant, changing the shear-coupled mobility by a factor of 3 and even changing its sign in some cases. A different technique has been developed to determine the

mobility of a curved boundary [11], but the analysis of mechanisms is more readily undertaken for planar or nearly planar grain boundaries.

Accordingly, the approach we have taken here starts with a large ensemble of planar grain boundaries created with the GRIP advanced search code [12]. For a specific grain boundary misorientation (relative grain orientations) and orientation (angle at which the boundary cuts through the grain), the ensemble includes boundaries with various levels of atomic filling at the boundary (n). One grain boundary in the ensemble has the lowest energy, corresponding to the stable grain boundary structure at low temperature. Other boundaries may have the lowest energy at a fixed n . Metastable boundaries with higher energies maybe stabilized at higher temperatures or under other conditions [6]. Machine learning techniques can be used to group related grain boundaries into phases [4].

Starting with an ensemble of grain boundaries where low-energy structures and phases have been identified, we determined the mobility of representative grain boundaries using molecular dynamics (MD). In this approach, the crystal lattice basis vectors for each grain comprising the bicrystal are provided, and a lattice orientation parameter χ is computed for each atom. A virtual potential $u(\chi)$ is then added to the energy of each atom in the bicrystal, transitioning smoothly from $u=-0.5u_0$ in the bulk crystal 1 to $u=0.5u_0$ in crystal 2 [13]. An example of the local orientation parameter and virtual potential is displayed in Figure 1. The force on each atom is determined from the interatomic forces plus the negative gradient of the virtual potential. Atoms located far from the grain boundary do not experience a virtual force, only interatomic forces from their neighbors, since their surroundings resemble those of a uniformly oriented single crystal. In contrast, atoms near the grain boundary encounter a nonzero virtual potential gradient and hence an additional virtual force. As the grain boundary moves, atoms cross into the grain with the lower potential, effectively consuming the higher potential grain. During an MD simulation using this virtual driving force, after an initial transient period in which the grain boundary begins to move, it eventually attains steady-state motion with some fluctuations. The energy released as the grain boundary moves down the potential energy gradient is dissipated as thermal energy. The ratio of the steady-state velocity to the (excess) driving force defines the grain boundary mobility.

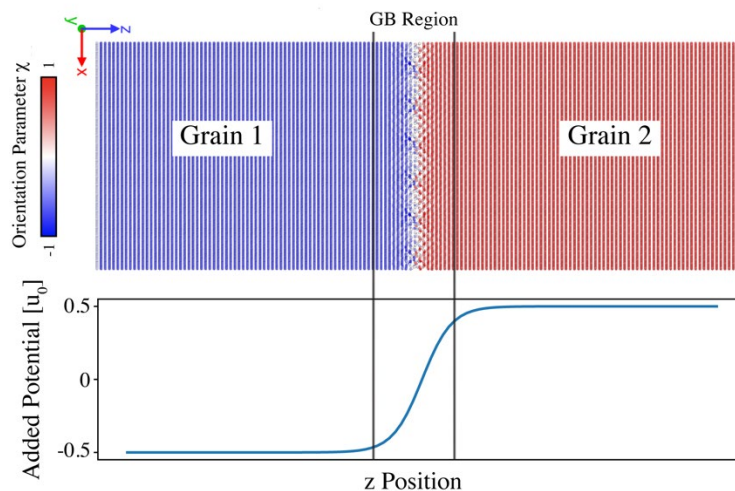


Figure 1. Example bicrystal illustrating the orientation parameter, χ , and added potential, $u_0(z)$.

The MD simulations were carried out using the Large-scale Atomic/Molecular Massively Parallel Simulator (LAMMPS) code [14] with the Zhou potential for tungsten [15]. This potential has been used for MD simulation of tungsten at tokamak conditions previously [6-11]. Thermal equilibrium was imposed using a Langevin thermostat and the equations of motion were integrated using a time step of 2 fs. Similar to our prior mobility work, an initial configuration with a specific grain boundary and grain boundary phase is selected from the GRIP-generated ensemble. In these bicrystal configurations, two grains with different orientations meet at the boundary. A virtual potential is added to the energy of each atom according to the

local crystal orientation that favors one grain over the other [13]. As the simulation advances, the atoms move according to $F=ma$ including the contribution of the virtual potential to the force. The grain boundary is tracked using OVITO, and its dislocation content is determined using DXA.

Here we focus on a twist boundary, one at which two grains meet with a relative rotation about the [001] axis. For a given twist angle, varying the number of atoms in the grain boundary plane can result in different grain boundary phases. Specifically, we focus on a $\Sigma 41$ twist boundary, with phases corresponding to filling fractions of $n=0.09 - 0.61$. As a first example, consider the properties of the $\Sigma 41$ twist boundary with $n = 0.61$ presented in Figure 2. Figure 2a depicts atoms in the grain boundary as spheres colored either blue or white for a local structure that is bcc or some unidentified complex structure, respectively, according to a common neighbor analysis. Superimposed on the atoms are curves indicating dislocation cores identified by DXA: pink $\langle 100 \rangle$ screw dislocations and green $\langle 111 \rangle$ mixed character dislocations. The weave of screw dislocations imparts the twist of this twist boundary. As time advances in the simulation, the boundary moves in the direction of the grain with the higher potential, due to the virtual driving force. The velocity it attains reflects the mobility of that boundary and grain boundary phase. Figure 2b shows the velocity as a function of the applied virtual potential. The three curves correspond to different temperatures: 300K (blue), 150K (red) and 77K (black). The higher velocity at the higher temperatures reflects a temperature-dependent mobility, one that increases with temperature. Each curve shows some non-linearity. The mobility is taken to be the best-fit slope at higher potential values where the curves are more linear.

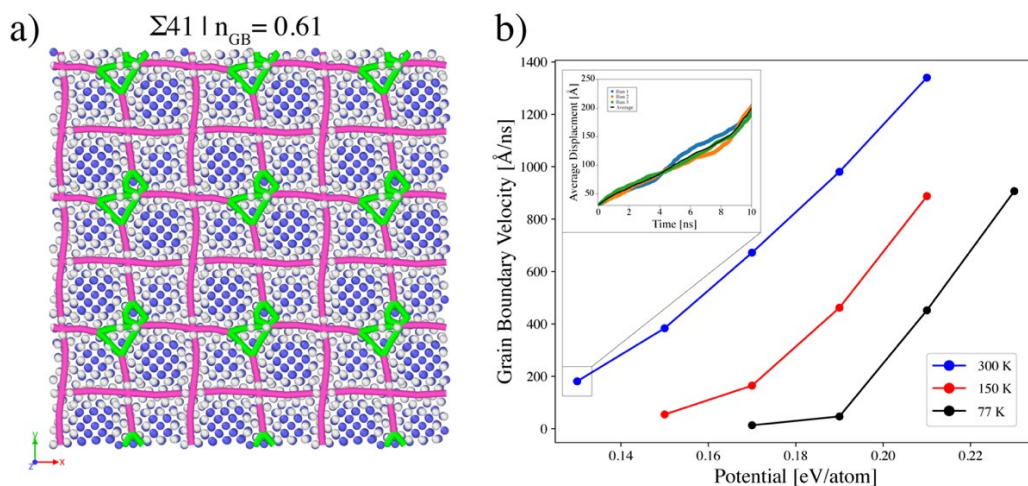


Figure 2. At a twist angle of 12.68° about the [001] axis, multiple grain boundary phases can form, each characterized by its distinct dislocation structure. In panel (a), the minimum-energy configuration produced by GRIP is shown, highlighting the dislocation structure with pink $\langle 100 \rangle$ screw dislocations and green $\langle 111 \rangle$ mixed character dislocations. The grain boundary atoms are colored according to Common Neighbor Analysis (CNA): blue indicates local bcc structure, while white indicates a structure type of other (i.e., not a common crystal structure). In panel (b), the grain boundary velocity is plotted against the bias potential used to apply a synthetic driving force to the boundary. Three curves are shown, each representing a different temperature: blue for 300K, red for 150K, and black for 77K. For each point on the curves, three simulations were conducted, as shown in the inset figure. The results were averaged, and the slope was taken to determine the grain boundary velocity at that driving potential.

The DXA can also be used to characterize how the dislocation network comprising the grain boundary changes as the boundary moves. Comparing the evolution for different phases, we have observed that the mechanism of mobility depends on the grain boundary phase. An example is given in Figure 3, which shows the evolution for two $\Sigma 41$ twist boundary phases differing in filling fraction: $n = 0.09$ (Figure 3a) and $n = 0.50$ (Figure 3b). In Figure 3a the $\Sigma 41|n=0.09$ begins as a pure $\langle 100 \rangle$ screw dislocation network at the

bottom of the sequence. All the dislocations are the pink $\langle 100 \rangle$ screw dislocations. As the boundary moves, $\langle 111 \rangle$ mixed dislocations are nucleated, and the boundary is a combination of the two dislocation types. The $\langle 111 \rangle$ dislocations are observed to advance more quickly, and thus play an important role in the mobility of this grain boundary in this phase. In Figure 3b the dual boundary, the $\Sigma 41 | n = 0.50$ begins comprised purely of $\langle 111 \rangle$ mixed dislocations, as shown at the bottom of the sequence. All the dislocations in the boundary are green. Again, as the boundary moves, the other dislocation type nucleates: the $\langle 100 \rangle$ screw dislocations in this case. In this case, too, the faster $\langle 111 \rangle$ mixed dislocations lead the advance of the grain boundary. We attribute the lower $\langle 100 \rangle$ grain boundary dislocation mobility to the necessity for these screw dislocations to nucleate out-of-plane $\langle 111 \rangle$ dislocations to initiate migration, a step not needed for $\langle 111 \rangle$ mixed dislocations.

The effect of the differences in the grain boundary dislocation mobility are more evident in larger simulation cells. The grain boundary morphology is less constrained by the periodic boundary conditions when the simulation box is larger. A larger simulation of the motion of the $\Sigma 41 | n = 0.61$ twist boundary is shown in Figure 4. In this case, the two boundary types segregate to a large extent. As evident in the Figure 4a top-down view, the $\Sigma 41 | n = 0.61$ grain boundary phase is observed to form a $\langle 111 \rangle$ mixed character dislocation network with a high $\langle 100 \rangle$ screw content inclusion, which is expected since the $n = 0.61$ phase is closer to the $n = 0.50$ phase (forming the matrix) than the $n = 0.09$ phase (similar to the inclusion). As the grain boundary moves in response to the virtual driving force, the matrix-inclusion character persists (Figures 4b and 4c). The grain boundary does not remain flat, however. Here the differences in the mobilities of the $\langle 111 \rangle$ mixed character and $\langle 100 \rangle$ screw dislocations are manifested in the boundary bulging backward (Figure 4c) as the less mobile inclusion is dragged by the faster $\langle 111 \rangle$ mixed character matrix.

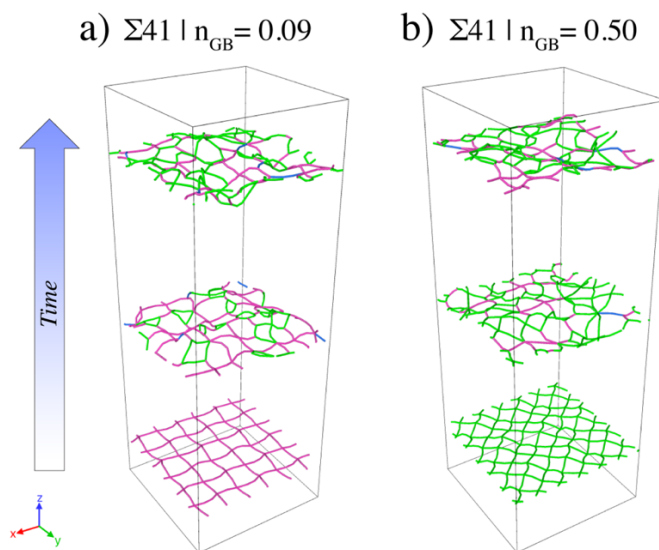


Figure 3. Different grain boundary phases exhibit different mobilities and structural transitions during migration, as shown in panels (a) and (b). Each panel presents a grain boundary moving upward at three different time steps, with the dislocation network evolving under an applied synthetic driving force. In panel (a), the initial structure consists of a $\langle 100 \rangle$ screw dislocation network (pink), while in panel (b), the grain boundary starts with $\langle 111 \rangle$ mixed character dislocations (green). In both cases the network evolves to a combination of the two dislocation types along with some $\langle 111 \rangle$ screw dislocations (blue). It is observed that grain boundaries with $\langle 111 \rangle$ mixed character dislocations tend to have the highest migration rate. The slower $\langle 100 \rangle$ mobility is attributed to the need for these screw dislocations first to nucleate out-of-plane $\langle 111 \rangle$ dislocations to initiate migration, a step not needed for $\langle 111 \rangle$ dislocations.

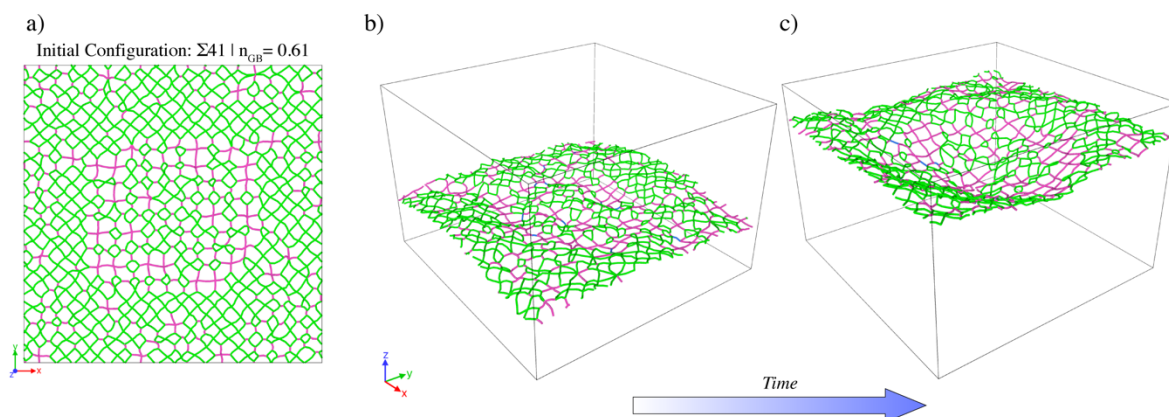


Figure 4. Using ground state structures predicted by GRIP with intermediate- n grain boundary and annealing them at finite temperature, phase separation is observed, resulting in two distinct dislocation network topologies that remain stable at high temperature. This heterogeneous structure is represented in panel (a), where a top-down view showcases the coexistence of two phases: a matrix of $\langle 111 \rangle$ dislocations (green) and a precipitate containing a mix of $\langle 100 \rangle$ and $\langle 111 \rangle$ dislocations (pink and green). By applying a synthetic driving force, we investigate the migration behavior of these phases. Panel (b) shows an early snapshot of the upward moving boundary, where it is evident that the matrix of $\langle 111 \rangle$ mixed character dislocations migrates faster than the screw dislocations at early times. Ultimately, the grain boundary must respond as one. In panel (c), the grain boundary is pinned due to the slower migration of the $\langle 100 \rangle$ screw dislocations, highlighting the different mobilities of the two phases.

Results

This analysis may provide the basis for a mechanistic, analytic model of the grain boundary mobility accounting for different phases. The development of the mechanistic model is to be undertaken in the future. We also are motivated to extend this analysis and associated modeling to include the effect of impurities on the boundary mobility, e.g., the mobilities of hydrogenated tungsten grain boundaries. The mobilities are provided to improve the parameterization of the thermomechanical model being developed by the Marian group at the University of California Los Angeles, providing new guidance on tungsten behavior in first-wall applications.

Acknowledgments

This work was performed under the auspices of the U.S. Department of Energy (US DOE) by Lawrence Livermore National Laboratory (LLNL) under Contract DE-AC52-07NA27344. This material is based upon work supported by the US DOE, Office of Science, Office of Fusion Energy Sciences. R. Moore's work was done as part of the Computational Chemistry and Materials Science Summer Institute at LLNL.

References

- [1] M.R. Gilbert, K. Arakawa, Z. Bergstrom, M.J. Caturla, S.L. Dudarev, F. Gao, A.M. Goryaeva, S.Y. Hu, X. Hu, R.J. Kurtz, A. Litnovsky, J. Marian, M.C. Marinica, E. Martinez, E.A. Marquis, D.R. Mason, B.N. Nguyen, P. Olsson, Y. Osetskiy, D. Senior, W. Setyawan, M.P. Short, T. Suzudo, J.R. Trelewicz, T. Tsuru, G.S. Was, B.D. Wirth, L. Yang, Y. Zhang, S.J. Zinkle, *Journal of Nuclear Materials* 554 (2021) 153113.
- [2] T. Frolov, D.L. Olmsted, M. Asta, Y. Mishin, *Nature Communications* 4 (2013) 1899.
- [3] T. Meiners, T. Frolov, R.E. Rudd, G. Dehm, C.H. Liebscher, *Nature* 579 (2020) 375-378.
- [4] Q. Zhu, A. Samanta, B. Li, R.E. Rudd, T. Frolov, *Nature Communications* 9 (2018) 467.
- [5] R. Freitas, R.E. Rudd, M. Asta, T. Frolov, *Physical Review Materials* 2 (2018) 093603.

- [6] T. Frolov, W. Setyawan, R.J. Kurtz, J. Marian, A.R. Oganov, R.E. Rudd, Q. Zhu, *Nanoscale* 10 (2018) 8253-8268.
- [7] T. Frolov, Q. Zhu, T. Ooppelstrup, J. Marian, R.E. Rudd, *Acta Materialia* 159 (2018) 123-134.
- [8] I.S. Winter, T. Ooppelstrup, T. Frolov, R.E. Rudd, *Acta Materialia* 237 (2022) 118067.
- [9] I.S. Winter, R.E. Rudd, T. Ooppelstrup, T. Frolov, *Physical Review Letters* 128 (2022) A69.
- [10] I.S. Winter, T. Frolov, *Physical Review Letters* 132 (2024) 186204.
- [11] A.F. Qiu, T.; Rudd, R. E., High-Temperature Mobility of Tungsten Grain Boundaries, *Fusion Materials Semiannual Progress Report, 2023*, pp. 134-137.
- [12] E. Chen, T.W. Heo, B.C. Wood, M. Asta, T. Frolov, *Nature Communications* 15 (2024) 7049.
- [13] F. Ulomek, C.J. O'Brien, S.M. Foiles, V. Mohles, *Modelling and Simulation in Materials Science and Engineering* 23 (2015) 025007.
- [14] A.P. Thompson, H.M. Aktulga, R. Berger, D.S. Bolintineanu, W.M. Brown, P.S. Crozier, P.J. in 't Veld, A. Kohlmeyer, S.G. Moore, T.D. Nguyen, R. Shan, M.J. Stevens, J. Tranchida, C. Trott, S.J. Plimpton, *Computer Physics Communications* 271 (2022) 108171.
- [15] X.W. Zhou, H.N.G. Wadley, R.A. Johnson, D.J. Larson, N. Tabat, A. Cerezo, A.K. Petford-Long, G.D.W. Smith, P.H. Clifton, R.L. Martens, T.F. Kelly, *Acta Materialia* 49 (2001) 4005-4015.

9.2 PROGRESS IN PREDICTIVE MODELING OF HE BUBBLE ACCUMULATION IN NANOSTRUCTURED FERRITIC ALLOYS—K. Pitike, J. Spencer, W. Setyawan (Pacific Northwest National Laboratory)

OBJECTIVE

The overall objective of this work is to develop a predictive model of helium bubble accumulation and distribution in irradiated nanostructured ferritic alloys under relevant fusion environments. As a first step, we have developed an accurate Fe-He machine learning potential (version MLP1) based of deep neural network that is intended to study defect binding in He clusters and small He_nV bubbles in pure BCC-Fe.

SUMMARY

This work was recently published in Journal of Nuclear Materials.¹ We have extended MLP1 to describe larger bubbles, by training MLP2 on configurations with bubbles containing 1-9 vacancies and He gas interacting with various BCC-Fe surface terminations. In this reporting period, (1) we employ MLP2 to estimate the He bubble equation of state (EOS) in BCC-Fe using molecular dynamics (MD) simulations. We compare the EOS obtained from MLP2 with existing semi-empirical potential. (2) we develop a Fe-H MLP that accurately predicts the H binding energies with monovacancy bubbles.

PROGRESS AND STATUS

Introduction

Developing equation of state from machine learning potential

Here we use molecular dynamics (MD) simulations to calculate the pressure of He bubbles in BCC-Fe, employing MLP2, and compare with semi-empirical potential reported in Caro et al.² The Caro potential is based on Fe potential by Ackland et al.,³ He potential by Beck et al.,⁴ and Fe-He cross potential by Juslin and Nordlund.⁵ The pressure, P , inside the bubble is calculated using the virial theorem:

$$P = \frac{1}{3V} \sum_i \left(m_i v_i^2 + \frac{1}{2} \sum_j \mathbf{r}_{ij} \cdot \mathbf{F}_{ij} \right) \quad (1)$$

i is the index of the He atom in the bubble and j is the index of the Fe and He atoms neighboring atom i . m_i and v_i are the atomic mass and speed of atom i , respectively. \mathbf{F}_{ij} is the force on atom i due to its interactions with atom j and \mathbf{r}_{ij} is the position vector of atom i measured from neighbor j , and V is the bubble volume. The bubble volume is computed based on Voronoi tessellation.

Experimental Procedure

Step 1: Calculating equation of state for He free gas

The MD simulations within the NVT ensemble employing a cubic simulation box with $a_0 = 22.64 \text{ \AA}$ was used to parametrize the He free gas equation of state. Several gas densities, ρ , were simulated by varying the number of He atoms between 580 and 2031, leading to the gas densities between ~ 0.05 and $\sim 0.17 \text{ He/\AA}^3$. Each gas density was simulated at three different temperatures, $T = 300, 500, \text{ and } 700 \text{ K}$. For each (T, ρ) , simulations ran for 300 ps, in which the pressure reached equilibrium within 200 ps, so the final pressure was taken as the average of the remaining 100 ps.

Figure 1 presents the P versus ρ plots for a free He gas using MLP2 and Caro potential. At low gas densities, the pressures predicted by both potentials agree with each other. However, at large gas densities,

MLP2 underpredicts the pressure at 700 K. We fit the P vs ρ data from Figure 1, to the free gas EOS derived by Setyawan et al.⁶

$$P = \rho k T (1 + B \rho_r + C \rho_r^2 + D \rho_r^3) \quad (2a)$$

$$B = b_0 + \frac{b_1}{T_r} + \frac{b_2}{T_r^2} \quad (2b)$$

$$C = c_0 + \frac{c_1}{T_r} + \frac{c_2}{T_r^2} \quad (2c)$$

$$D = d_0 + \frac{d_1}{T_r} + \frac{d_2}{T_r^2} \quad (2d)$$

$$\rho_r = \frac{\rho}{\rho_c} \quad (2e)$$

$$T_r = \frac{T}{T_c} \quad (2f)$$

P is the gas pressure, k is Boltzmann constant, ρ is the free gas density, T is temperature, ρ_c is the free gas density at the critical point of He ($0.010419 \text{ \AA}^{-3}$), and T_c is the critical point temperature of He (5.195 K).⁷ b_i , c_i , and d_i are model parameters, whose values are fitted to data in Figure 1. The fitted parameters obtained from simulations using MLP2, and Caro potential are shown in Table 1, and Table 2, respectively.

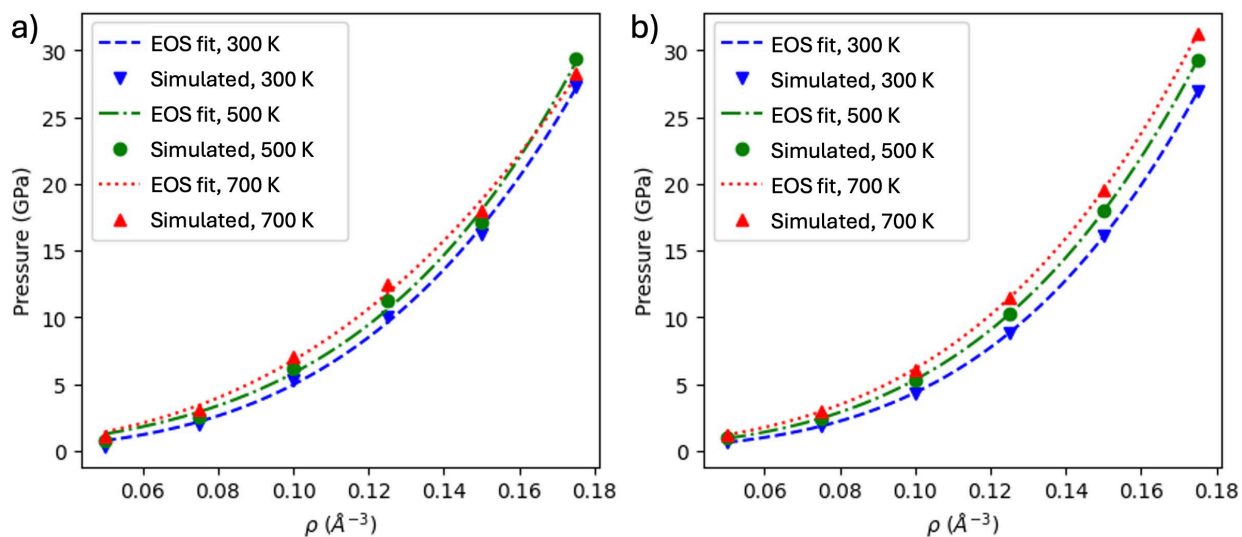


Figure 1. Pressure, P , vs He gas density, ρ , of He free gas at various temperatures, calculated using a) MLP2 and b) Caro potential. Lines represent the EOS model fit.

Table 1. the EOS parameters obtained by fitting data from free gas MLP2 simulations to Equation 2

MLP2 free gas EOS			
i	b_i	c_i	d_i
0	-1.859×10^0	4.112×10^{-1}	-1.958×10^{-2}
1	3.922×10^2	-7.084×10^1	3.593×10^0
2	-1.638×10^4	3.055×10^3	-1.368×10^2

Table 2. The EOS parameters obtained by fitting data from free gas Caro potential simulations to Equation 2

Caro potential free gas EOS			
i	b_i	c_i	d_i
0	-2.716×10^{-1}	7.562×10^{-2}	-3.057×10^{-3}
1	8.661×10^1	-1.085×10^1	7.897×10^{-1}
2	-5.738×10^3	8.852×10^2	-3.491×10^1

Step 2: Calculating equation of state for He gas bubbles in BCC-Fe

Figures 2(a,b) presents the pressure of He gas bubbles vs number of He/V ratio calculated for bubbles with 78 vacancies, using MLP2 and Caro potentials, respectively. The same relationship for bubbles containing 152 vacancies is shown in Figures 2(c,d). We find that MLP2 exhibits unexpected non-monotonic pressure relationship with He/V ratio between 0.5 and 1.5 ratio. However, Caro potential predicts smooth monotonic increase in pressure with He/V ratio up to 2.5. For He/V > 2.5 we find that both MLP2 and Caro potential predicts trap-mutation of bubble, thereby relieving the pressure. Due to this non-monotonic pressure relation, we believe that MLP2 is not suitable for calculating bubble pressure. Next we parametrize a He-bubble EOS in BCC-Fe, following the theory presented in Setyawan et al.⁶

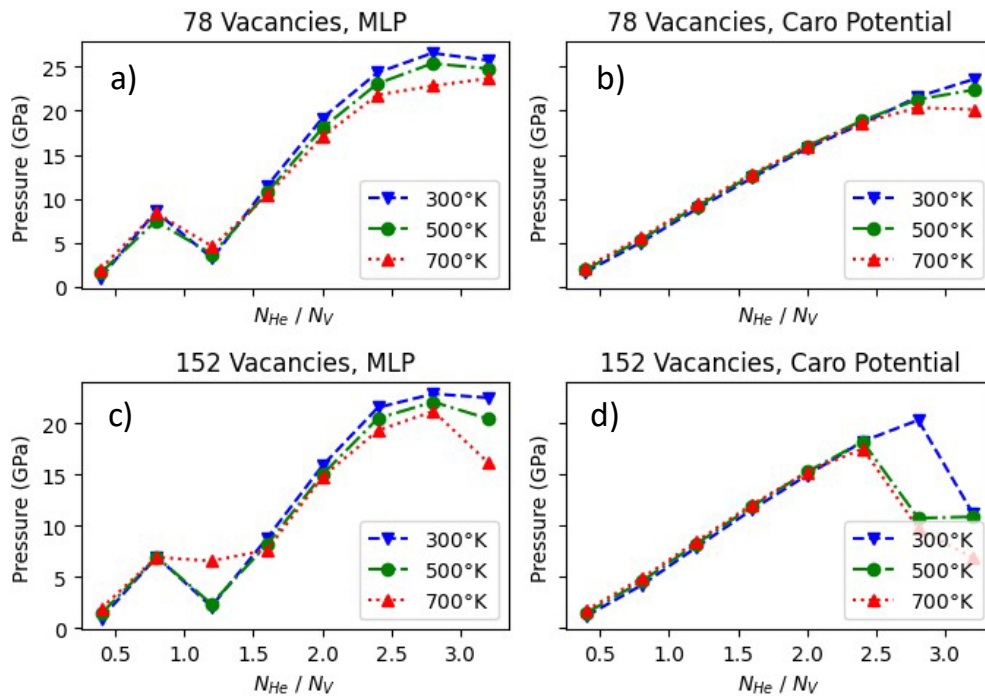


Figure 2. He gas bubble pressure vs number of He/V ratio.

The He bubble EOS in BCC-Fe can be accurately described by correcting the gas density to account for the Fe-He repulsion in Eq (2) as follows:

$$\rho = \rho_B \left(\frac{R}{R + \Delta R} \right) \tag{3a}$$

$$\Delta R = (f_0 + f_1 T_r) \rho_{Br} + (f_2 + f_3 T_r) \rho_{Br}^2 \tag{3b}$$

$$\rho_{Br} = \frac{\rho_B}{\rho_c} \tag{3c}$$

ρ is the corrected density of He gas [refer to Equation (2)], ρ_B is the uncorrected gas density of the bubble, R is radius of the He bubble, calculated from the bubble volume by assuming a spherical bubble. f_i , are the model parameters to be fitted to MD simulation data.

Figure 3 presents the pressure of the He bubble, P , vs He bubble pressure, ρ_B , using (a, c) MLP2 and (b, d) Caro potential. The fitted parameters of equations 3(a-c) are provided in Table 3. The EOS derived from the Caro potential accurately predicts simulation data, consistent with helium bubble behavior in tungsten.⁶ In contrast, the MLP2-based EOS fails to fit the data due to non-physical pressure behavior.

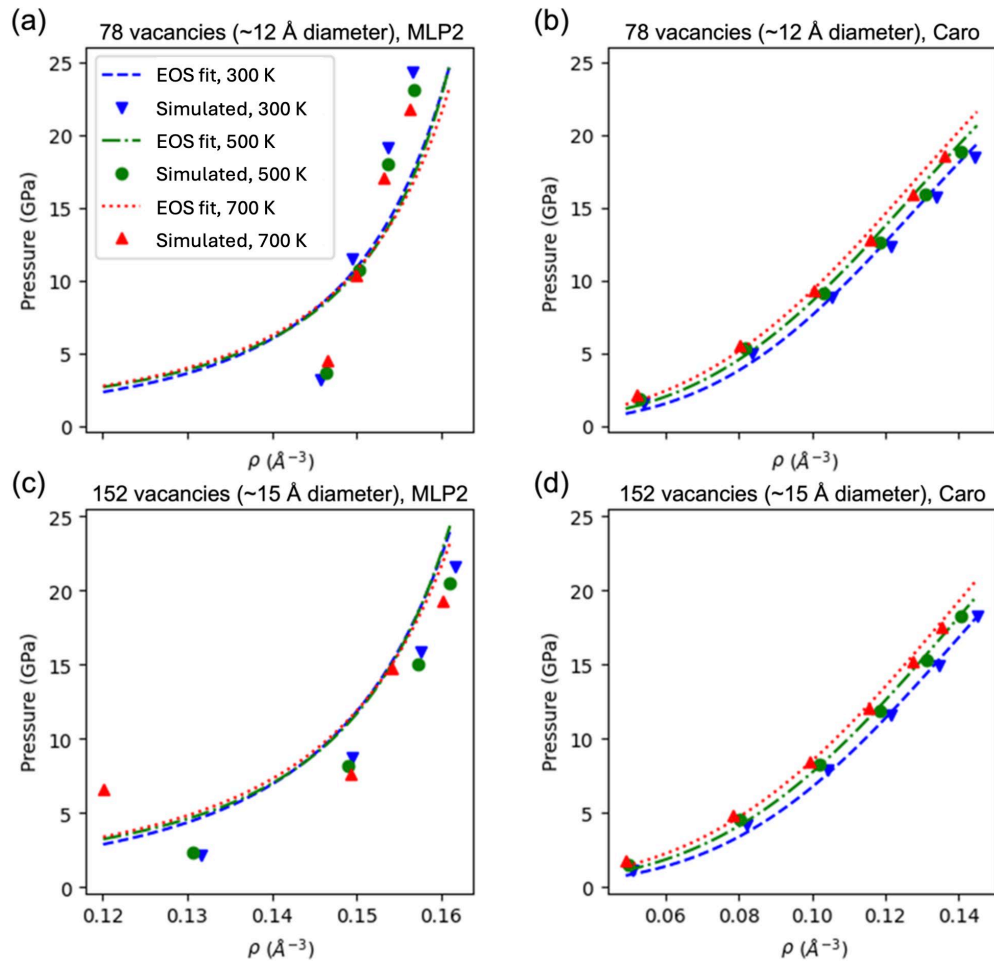


Figure 3. He bubble pressure vs corrected density calculated using (a, c) MLP2 and (b, d) Caro potential. Lines represent the EOS model fit predictions from Equations (2, 3).

Table 3. The EOS parameters obtained by fitting data He gas bubble pressures to Equation 4, obtained using MLP2 and Caro potential

	MLP2	Caro Potential
f_0	9.279×10^{-1}	-2.528×10^{-1}
f_1	4.709×10^{-3}	2.399×10^{-4}
f_2	-6.212×10^{-2}	1.511×10^{-2}
f_3	-2.915×10^{-4}	-9.276×10^{-6}

Development of Fe-H MLP to accurately predict binding energies

We develop a Fe-H MLP, based on atomic configurations sampled using DFT. The neural network architecture used to develop Fe-H MLP is the same as the one used for Fe-He MLP1 and MLP2. Here we present the comparison of formation energies (E_f) of point defects such as vacancy (V), interstitial (H_{tet} , H_{oct}) and substitutional hydrogen (H_{sub}) using MLP and DFT. Furthermore, the migration of interstitial hydrogen between two tetrahedral positions and binding energies of interstitial hydrogen with monovacancy hydrogen bubbles, $H_{n-1}V$, are also presented.

Figure 4 presents the comparison of binding energies of hydrogen with $H_{n-1}V$ bubble, calculated using MLP and DFT. The binding energies are calculated using: Binding Energy = $E[H_{n-1}V] + E[H_{tet}] - E[H_nV] - E[\text{pristine}]$. $E[H_{n-1}V]$ and $E[H_nV]$ are the total energies of $H_{n-1}V$ and H_nV monovacancy bubbles containing $n - 1$ and n number of hydrogen atoms, respectively. $E[H_{tet}]$ and $E[\text{pristine}]$ are the total energies of H in a tetrahedral position (which is the ground state of H in BCC-Fe) and pristine supercell of BCC-Fe, respectively. Here we find that DFT predicts positive binding energies for $n = 1$ to 5 and negative binding energy for $n = 7$. This data is in agreement with binding energies from literature, calculated using DFT and interatomic potentials.⁸ For $n = 6$, DFT calculations in our work predict a small but positive binding energy, 4 meV – indicating thermodynamic stability at 0 K – which is 23 meV greater than DFT value from Ramasubramaniam et al.⁸ (-19 meV) a negative value. This discrepancy can be explained by the smaller 3x3x3 supercell used by Ramasubramaniam et al.⁸ The binding energies calculated using MLP are in good agreement with DFT values, with maximum error of 66 meV (25%), at $n = 4$.

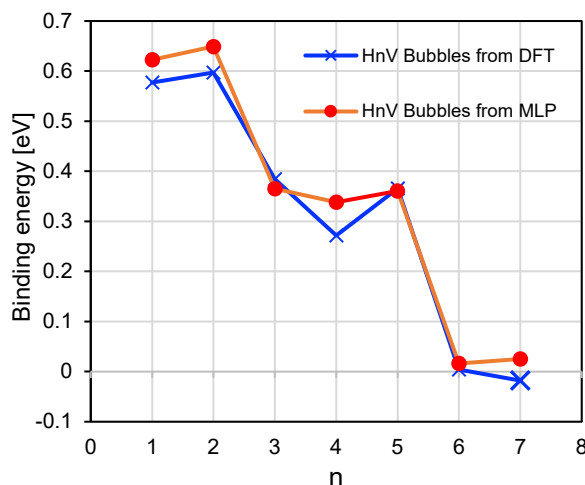
**Figure 4.** Binding energies of interstitial H with $H_{n-1}V$ bubble to form H_nV bubble, calculated using DFT and MLP.

Figure 5 presents the comparison between the migration barrier of interstitial hydrogen between two adjacent tetrahedral positions, calculated using DFT and MLP. Nudged elastic band (NEB) method is used

to calculate the migration barriers. We find that the migration barrier calculated by MLP is in good agreement between DFT, with error=1 meV (1.4%).

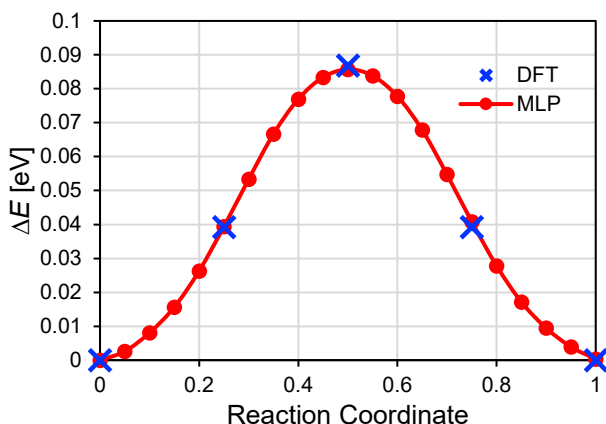


Figure 5. The migration energy of H between adjacent tetrahedral positions in BCC-Fe calculated DFT and MLP.

Table 4. Formation energy of a vacancy or H defect in bcc Fe, migration energy of H, and binding energy of H with a VH_{n-1} bubble

	MLP [eV]	DFT [eV]	Error [eV]
$E_f[V]$	2.504	2.150	0.354
$E_f[H_{tet}]$	0.441	0.223	0.218
$E_f[H_{oct}]$	0.565	0.352	0.213
$E_f[H_{sub}]$	-0.507	-0.354	-0.154
$E_m[H_{tet}]$	0.086	0.087	0.001
$E_b[n = 1]$	0.623	0.577	0.046
$E_b[n = 2]$	0.649	0.597	0.052
$E_b[n = 3]$	0.365	0.384	-0.019
$E_b[n = 4]$	0.338	0.272	0.067
$E_b[n = 5]$	0.361	0.366	-0.005
$E_b[n = 6]$	0.016	0.004	0.012
$E_b[n = 7]$	0.025	-0.018	0.043

Table 4 presents the comparison formation energies of vacancy, $E_f[V]$, tetrahedral hydrogen, $E_f[H_{tet}]$, octahedral hydrogen, $E_f[H_{oct}]$, substitutional hydrogen, $E_f[H_{sub}]$, migration barrier between two adjacent tetrahedral positions, $E_m[H_{oct}]$, and binding energies of H with $H_{n-1}V$ bubbles for $n = 1$ to $n = 7$, calculated using DFT and MLP. Even though the formation energies are predicted with large errors (>200 meV) compared to DFT, the binding energies of H with monovacancy bubbles are calculated with excellent accuracy (error < 66 meV). Furthermore, the migration barrier of interstitial H migration between two adjacent tetrahedral positions is also predicted accurately by MLP with error = 1 meV.

Results

Future research will continue the MD simulations using the Caro potential to obtain additional data points of bubble pressures (data at 900 K and for 2-3 additional bubble sizes) to complete the EOS. Results will be submitted for publication.

Acknowledgements

This research was supported by the U.S. Department of Energy (US DOE), Office of Science, Office of Fusion Energy Sciences, through Contract No. AT2030110-13784 and was performed at the Pacific Northwest National Laboratory, which is operated by Battelle for the US DOE under Contract No. DE-AC05-76RL0-1830.

References

- [1.] C. K. Pitike, W. Setyawan, Accurate Fe–He Machine Learning Potential for Studying He Effects in BCC-Fe, *Journal of Nuclear Materials* 574 (2023) 154183.
- [2.] A. Caro, J. Hetherly, A. Stukowski, et al., Properties of Helium Bubbles in Fe and FeCr Alloys, *Journal of Nuclear Materials* 418 (2011) 261.
- [3.] G. J. Ackland, M. I. Mendelev, D. J. Srolovitz, et al., Development of an Interatomic Potential for Phosphorus Impurities in Iron, *Philosophical Magazine* 16 (2004) S2629.
- [4.] D. E. Beck, A New Interatomic Potential Function for Helium, *Molecular Physics* 14 (1968) 311.
- [5.] N. Juslin, K. Nordlund, Pair Potential for Fe–He, *Journal of Nuclear Materials* 382 (2008) 143.
- [6.] W. Setyawan, D. Dasgupta, S. Blondel, et al., Equation of State for He Bubbles in W and Model of He Bubble Growth and Bursting near W{100} Surfaces Derived from Molecular Dynamics Simulations, *Scientific Reports* 13 (2023) 9601.
- [7.] A. Y. Cengel, M. A. Boles, M. Kanoğlu, *Thermodynamics: An Engineering Approach*; McGraw-hill New York, 2011; Vol. 5.
- [8.] A. Ramasubramaniam, M. Itakura, A. E. Carter, Erratum: Interatomic Potentials for Hydrogen in α -Iron Based on Density Functional Theory, *Physical Review B* 81 (2010) 099902.

9.3 FIRST PRINCIPLES STUDY OF RADIATION INDUCED DEFECTS IN TiB₂—Y. Osetskiy, G. Samolyuk (Oak Ridge National Laboratory)

OBJECTIVE

The objective of this task is to obtain an understanding of the bulk and radiation-induced properties of TiB₂ and mechanisms operating at atomic-scale in TiB₂ under neutron irradiation.

SUMMARY

The following defects and effects are under consideration: a) point defects and small clusters, their interactions, and mobility, b) extended defects such as dislocations and dislocation loops, stacking faults, and grain boundaries (GB), and c) microstructure evolution mechanisms under irradiation and its effects on the material mechanical and physical properties. Main techniques applied are density functional theory (DFT) for modeling defect properties, classical and DFT molecular dynamics (MD) for modeling defect dynamics, machine learning approach for developing classical interatomic force fields, elasticity theory for estimating defect-defect interactions, and kinetic Monte Carlo modeling for modeling large scale defect dynamics and microstructure evolution.

PROGRESS AND STATUS

Ultra-high temperature ceramics (UHTC), and particularly TiB₂, are considered as promising materials for plasma-facing components. Having exceptional high temperature properties, these materials, however, are not thoroughly tested for specific plasma facing phenomena and the mechanisms of radiation effects in them are mostly unknown. An experiment program on radiation effects in UHTC, including TiB₂, developed at Oak Ridge National Laboratory (ORNL) a few years ago reported fundamental effects such as formation of dislocation loops in the bulk and cavities at GB [1, 2]. Intensive segregation was observed in [3] and a tentative explanation of Ti enrichment and B depletion at GB was explained by vacancy migration mechanism. Not much is known on the structure of radiation defects. Dislocation loops in basal (c-type) and prism (a-type) planes are reported in [1, 2] after neutron irradiation and possibly, defected Frank loops were observed after irradiation in electron microscope with 200keV electrons producing only B-atoms displacements. However, the detailed structure of radiation induced defects, as well as the mechanisms of their formation, growth and interactions are not known yet. This, in large extend, delays the developing models for predicting behavior of TiB₂ under fusion environment conditions. A new research line within the ORNL Fusion Materials program was initiated with the main aim of understanding mechanisms of radiation damage phenomena in TiB₂ and developing predictive modeling capabilities. In the first stage, we are interested in understanding properties of point defects and their clusters, and the early stage of radiation damage microstructure evolution. This includes defects formation, interactions and growth. The objects under the current interest are clusters of vacancies and interstitial atoms, their transformation into dislocation loops, stacking faults and behavior He and H gas atoms.

We utilize a first principle-based approach to study basic properties of TiB₂, including bulk physical properties, radiation induced defects, and their interactions. Electronic structures and energies have been calculated within the density-functional theory [5] using the generalized gradient approximation (GGA) and the Perdew-Burke-Ernzerhof (PBE) [6] parametrization of the electronic exchange-correlation functional. Total energies and electronic structure were calculated using the plane-wave basis projector augmented-wave approach [7] as implemented in the Vienna Ab-initio Simulation Package (VASP) [8]. The high accuracy of modeling results was provided by the high inner energy cut-off, 520 eV, and low ionic energy convergency criterion, 10⁻⁶ eV. Supercells of different sizes, up to ~700 atoms, were used to investigate cell size effects on defects' energy and structure. First calculations have confirmed that basic properties of point defects, vacancy, and interstitial atoms in both sublattices, are well converged in supercell with less than ~400 atoms. This can be seen in Figure 1, where size dependences of vacancy formation energy in Ti and Be sublattices are presented.

Analysis of experimental results suggests that dislocation loops in TiB₂ consist of B-interstitials. At least at early stage of their growth, these are not prismatic dislocation loops but more like faulted Frank loops in fcc materials as mentioned in [3]. Further growth should lead to upfaulting towards prismatic loops [1]. Interstitial atoms modelled here in both subsystems demonstrated a large difference in formation energy: $E_{Ti}^i = 10.55$ eV vs $E_B^i = 5.14$ eV. Note, that each configuration was tested for stability following the three-step procedure i.e. 1) relaxation of initial configuration at T=0K, 2) heating up to T=1200K and annealing by molecular dynamics (MD) over 10,000 integration steps (10ps of physical time), and 3) relaxation towards minimum energy at 0K. Different B-di-interstitials were modelled for understanding loop nucleation. The most stable configurations are presented in Figure 1. They have binding energy $E_{2B}^b = 0.88$ eV (0.93 after MD) (Figure 1a) and $E_{2B}^b = 0.24$ eV (0.28 after MD) (Figure 1b). Two other metastable configurations are: a) aligned along z-axis with two B atoms with $E_{2B}^b = -0.04$ eV, and b) in plane configuration with $E_{2B}^b = -0.98$ eV. Configuration b) was found to be thermally unstable and during MD step was transformed into the most stable configuration shown on Figure 1a. These di-interstitial configurations can be assumed as nuclei of dislocation loops in prism planes observed experimentally.

Larger clusters are currently modeling to clarify the nucleation and growth mechanisms in both hexagonal and prism planes. For example, the binding energy for third B interstitial added to the configuration shown in Figure 1a for found to be 1.5 eV. This configuration, shown in Figure 2, being very stable can serve as a nucleus of dislocation loop in the prism plane. Modeling of larger clusters in prism and basal planes is the progress currently. Small clusters may create stacking faults, and their relative stability should depend on the stacking fault energy.

Due to a high binding energy, vacancies are natural sinks for gas atoms such as D(H) and He. Vacancy-gas binding energy also depends on the vacancy type: it is higher for D in B-vacancy $E_{B-D}^b = 1.63$ eV compared to D in Ti-vacancy $E_{Ti-D}^b = 1.13$ eV. Larger D and He clusters are currently studying to obtain mechanisms and parameters for modeling D retention and desorption to be compared with experimental results on the thermally activated desorption.

Results

For understanding dislocation loops evolution and degradation of mechanical stability under irradiation we plan to:

- Model loop growing in different planes for understanding their evolution.
- Model mobility and diffusion of B- and T- interstitial atoms. We expect that anisotropy in their diffusion can explain anisotropic radiation growth of TiB₂ under neutron irradiation.
- Develop model for predicting degradation of mechanical stability of multigame materials based on the radiation induced anisotropic growth of TiB₂.

For predicting H (D) and He retention and desorption needs, we plan to:

- Model vacancy clusters and their interactions with D(H) and He atoms accumulating binding energy for V_n-D_m (-He_m) vacancies-gas atoms combinations.
- Apply *ab initio* MD for modeling D(H) and He diffusion in the TiB₂ bulk.
- Develop a kinetic Monte Carlo model describing vacancy-gas clusters evolution during both growing and desorption processes. The former will model microstructure evolution, the later will be used for modeling desorption experiments.

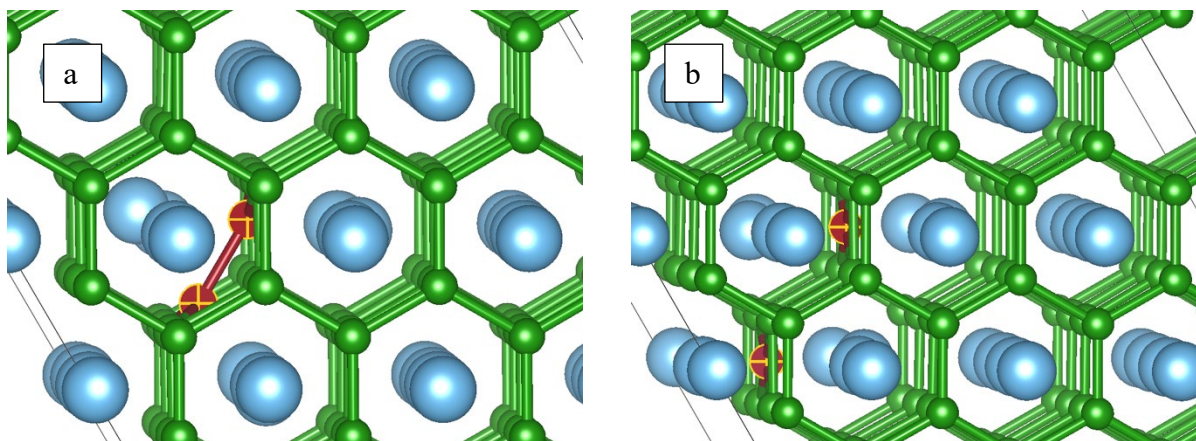


Figure 1. The most stable configurations of boron di-interstitials in TiB_2 bulk. Boron interstitial atoms are presented by red-crossed spheres. A cross-platform program, VESTA, has been used to visualize the structure [9].

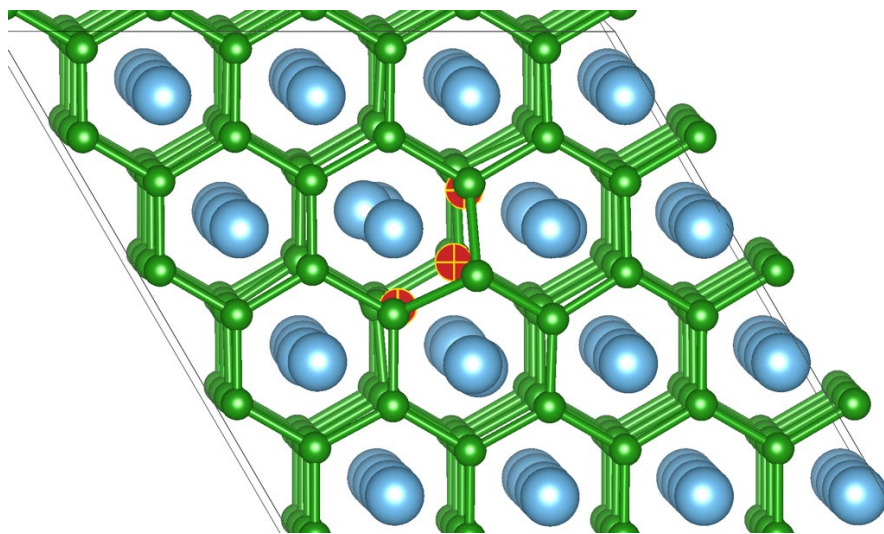


Figure 2. Configuration of the most stable clusters containing three B-interstitial atoms.

References

- [1] T. Koyanagi T, Katoh Y, Ang C, King D, Hilmas GE, Fahrenholtz WG. Response of isotopically tailored titanium diboride to neutron irradiation. *J Am Ceram Soc.* 2019;102:85–89. <https://doi.org/10.1111/jace.16036>
- [2] A. Bhattacharya, C.M. Parish, T. Koyanagi, C.M. Petrie, D. King, G. Hilmas, W.G. Fahrenholtz, S.J. Zinkle, Y. Katoh, Nano-scale microstructure damage by neutron irradiations in a novel Boron-11 enriched TiB_2 ultra-high temperature ceramic, *Acta Mater.*, 165 (2019) 26-39.
- [3] M. Carrard, D. Emin, L. Zuppiroli, Defect clustering and self-healing of electron-irradiated boron-rich solids, *Phys. Rev. B* 51 (1995) 11270.
- [4] S. Wei, M.W. Qureshi, J. Xi, J.Y. Kim, X. Wang, J. Wei, R. Su, L. Liu, W.O. Nachlas, J.H. Perepezko, H. Zhang, I. Szuflarska, Radiation induced segregation in titanium diboride, *Acta Mater.*, 267 (2024) 119739.

- [5] W. Kohn and L. J. Sham, Self-Consistent Equations Including Exchange and Correlation Effects, *Phys. Rev.* 140, 1133 (1965).
- [6] J.P. Perdew, K. Burke, and M. Ernzerhof, Generalized Gradient Approximation Made Simple, *Phys. Rev. Lett.* 77, 3865 (1996).
- [7] P. E. Blöchl, Projector augmented-wave method, *Phys. Rev. B* 50, 17953 (1994).
- [8] Vienna Ab initio Simulation Package, <http://cms.mpi.univie.ac.at/vasp/>.
- [9] K. Momma and F. Izumi, “VESTA 3 for three-dimensional visualization of crystal, volumetric and morphology data,” *J. Appl. Crystallogr.*, 44, 1272-1276 (2011).

9.4 PROGRESS IN PREDICTIVE MODELING OF HE BUBBLE ACCUMULATION IN NANOSTRUCTURED FERRITIC ALLOYS—K. Pitike, J. Spencer, W. Setyawan (Pacific Northwest National Laboratory)

OBJECTIVE

The overall objective of this work is to develop a predictive model of helium bubble accumulation and distribution in irradiated nanostructured ferritic alloys under relevant fusion environments.

SUMMARY

As a first step, we have developed an accurate Fe-He machine learning potential (version MLP1) based of deep neural network that is intended to study defect binding in He clusters and small He_nV bubbles in pure BCC-Fe. This work was recently published in Journal of Nuclear Materials.¹ We have extended MLP1 to describe larger bubbles, by training MLP2 on configurations with bubbles containing 1-9 vacancies and He gas interacting with various BCC-Fe surface terminations. In this reporting period, (1) We employ MLP2 to estimate the He bubble equation of state (EOS) in BCC-Fe using molecular dynamics (MD) simulations. We compare the EOS obtained from MLP2 with existing semi-empirical potential. (2) We develop a Fe-H MLP that accurately predicts the H binding energies with monovacancy bubbles.

PROGRESS AND STATUS

Introduction

Developing equation of state from machine learning potential

Here we use MD simulations to calculate the pressure of He bubbles in BCC-Fe, employing MLP2, and compare with semi-empirical potential reported in Caro et al.² The Caro potential is based on Fe potential by Ackland et al.,³ He potential by Beck et al.,⁴ and Fe-He cross potential by Juslin and Nordlund.⁵ The pressure, P , inside the bubble is calculated using the virial theorem:

$$P = \frac{1}{3V} \sum_i \left(m_i v_i^2 + \frac{1}{2} \sum_j \mathbf{r}_{ij} \cdot \mathbf{F}_{ij} \right) \quad (1)$$

i is the index of the He atom in the bubble and j is the index of the Fe and He atoms neighboring atom i . m_i and v_i are the atomic mass and speed of atom i , respectively. \mathbf{F}_{ij} is the force on atom i due to its interactions with atom j and \mathbf{r}_{ij} is the position vector of atom i measured from neighbor j , and V is the bubble volume. The bubble volume is computed based on Voronoi tessellation.

Step 1: Calculating equation of state for He free gas

The MD simulations within the NVT ensemble employing a cubic simulation box with $a_0 = 22.64 \text{ \AA}$ was used to parametrize the He free gas equation of state. Several gas densities, ρ , were simulated by varying the number of He atoms between 580 and 2031, leading to the gas densities between ~ 0.05 and $\sim 0.17 \text{ He/\AA}^3$. Each gas density was simulated at three different temperatures, $T = 300, 500, \text{ and } 700 \text{ K}$. For each (T, ρ) , simulations ran for 300 ps, in which the pressure reached equilibrium within 200 ps, so the final pressure was taken as the average of the remaining 100 ps.

Figure 1 presents the P versus ρ plots for a free He gas using MLP2 and Caro potential. At low gas densities, the pressures predicted by both potentials agree with each other. However, at large gas densities, MLP2 underpredicts the pressure at 700 K. We fit the P vs ρ data from Figure 1, to the free gas EOS derived by Setyawan et al.⁶

$$P = \rho k T (1 + B \rho_r + C \rho_r^2 + D \rho_r^3) \quad (2a)$$

$$B = b_0 + \frac{b_1}{T_r} + \frac{b_2}{T_r^2} \quad (2b)$$

$$C = c_0 + \frac{c_1}{T_r} + \frac{c_2}{T_r^2} \quad (2c)$$

$$D = d_0 + \frac{d_1}{T_r} + \frac{d_2}{T_r^2} \quad (2d)$$

$$\rho_r = \frac{\rho}{\rho_c} \quad (2e)$$

$$T_r = \frac{T}{T_c} \quad (2f)$$

P is the gas pressure, k is Boltzmann constant, ρ is the free gas density, T is temperature, ρ_c is the free gas density at the critical point of He ($0.010419 \text{ \AA}^{-3}$), and T_c is the critical point temperature of He (5.195 K).⁷ b_i , c_i , and d_i are model parameters, whose values are fitted to data in Figure 1. The fitted parameters obtained from simulations using MLP2, and Caro potential are shown in Table 1, and Table 2, respectively.

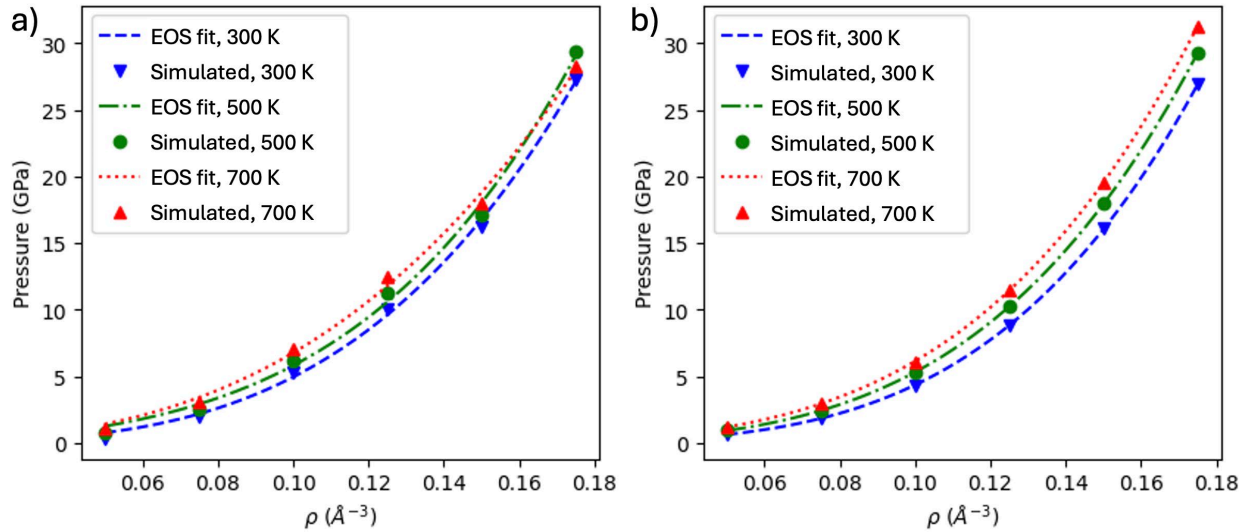


Figure 1. Pressure, P , vs He gas density, ρ , of He free gas at various temperatures, calculated using a) MLP2 and b) Caro potential. Lines represent the EOS model fit.

Table 1. The EOS parameters obtained by fitting data from free gas MLP2 simulations to Equation 2

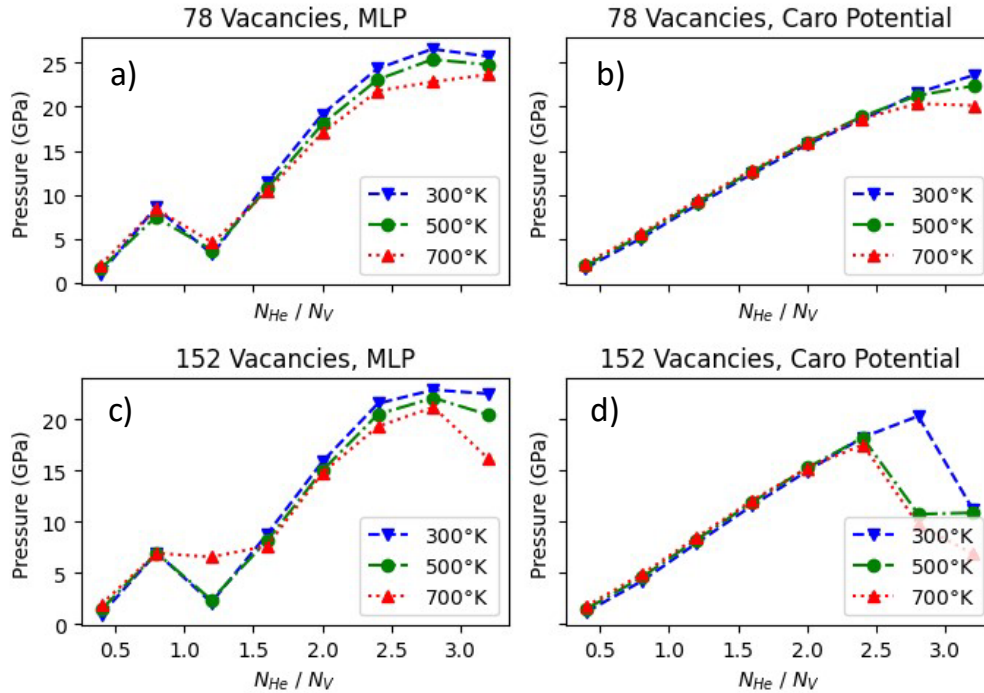
MLP2 free gas EOS			
i	b_i	c_i	d_i
0	-1.859×10^0	4.112×10^{-1}	-1.958×10^{-2}
1	3.922×10^2	-7.084×10^1	3.593×10^0
2	-1.638×10^4	3.055×10^3	-1.368×10^2

Table 2. The EOS parameters obtained by fitting data from free gas Caro potential simulations to Equation 2

Caro potential free gas EOS			
i	b_i	c_i	d_i
0	-2.716×10^{-1}	7.562×10^{-2}	-3.057×10^{-3}
1	8.661×10^1	-1.085×10^1	7.897×10^{-1}
2	-5.738×10^3	8.852×10^2	-3.491×10^1

Step 2: Calculating equation of state for He gas bubbles in BCC-Fe

Figures 2(a,b) presents the pressure of He gas bubbles vs number of He/V ratio calculated for bubbles with 78 vacancies, using MLP2 and Caro potentials, respectively. The same relationship for bubbles containing 152 vacancies is shown in Figures 2(c,d). We find that MLP2 exhibits unexpected non-monotonic pressure relationship with He/V ratio between 0.5 and 1.5 ratio. However, Caro potential predicts smooth monotonic increase in pressure with He/V ratio up to 2.5. For He/V > 2.5 we find that both MLP2 and Caro potential predicts trap-mutation of bubble, thereby relieving the pressure. Due to this non-monotonic pressure relation, we believe that MLP2 is not suitable for calculating bubble pressure. Next we parametrize a He-bubble EOS in BCC-Fe, following the theory presented in Setyawan et al.⁶

**Figure 2.** He gas bubble pressure vs number of He/V ratio.

The He bubble EOS in BCC-Fe can be accurately described by correcting the gas density to account for the Fe-He repulsion in Eq (2) as follows:

$$\rho = \rho_B \left(\frac{R}{R + \Delta R} \right) \quad (3a)$$

$$\Delta R = (f_0 + f_1 T_r) \rho_{Br} + (f_2 + f_3 T_r) \rho_{Br}^2 \quad (3b)$$

$$\rho_{Br} = \frac{\rho_B}{\rho_c} \quad (3c)$$

ρ is the corrected density of He gas [refer to Equation (2)], ρ_B is the uncorrected gas density of the bubble, R is radius of the He bubble, calculated from the bubble volume by assuming a spherical bubble. f_i are the model parameters to be fitted to MD simulation data.

Figure 3 presents the pressure of the He bubble, P , vs He bubble pressure, ρ_B , using (a, c) MLP2 and (b, d) Caro potential. The fitted parameters of equations 3(a-c) are provided in Table 3. The EOS derived from the Caro potential accurately predicts simulation data, consistent with helium bubble behavior in tungsten.⁶ In contrast, the MLP2-based EOS fails to fit the data due to non-physical pressure behavior.

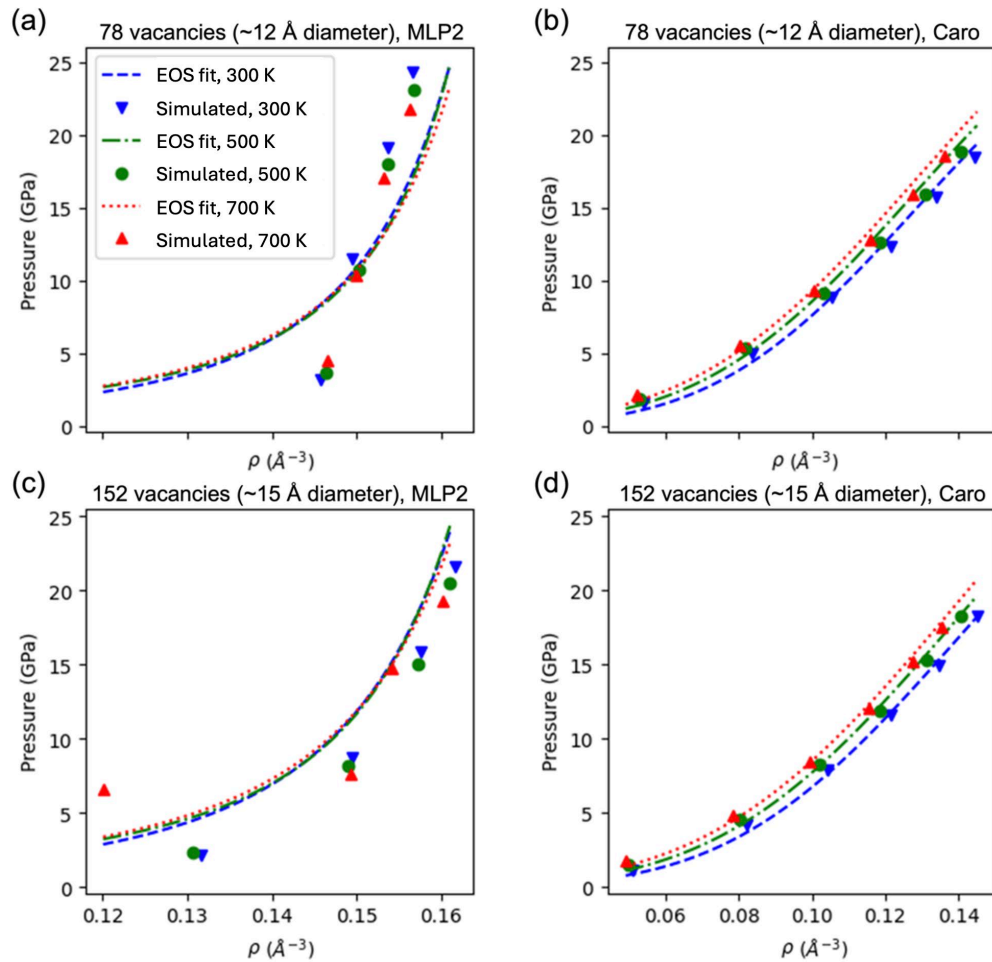


Figure 3. The He bubble pressure vs corrected density calculated using (a, c) MLP2 and (b, d) Caro potential. Lines represent the EOS model fit predictions from Equations (2, 3).

Table 3. The EOS parameters obtained by fitting data He gas bubble pressures to Equation 4, obtained using MLP2 and Caro potential

	MLP2	Caro Potential
f_0	9.279×10^{-1}	-2.528×10^{-1}
f_1	4.709×10^{-3}	2.399×10^{-4}
f_2	-6.212×10^{-2}	1.511×10^{-2}
f_3	-2.915×10^{-4}	-9.276×10^{-6}

Development of Fe-H MLP to accurately predict binding energies

We develop a Fe-H MLP, based on atomic configurations sampled using DFT. The neural network architecture used to develop Fe-H MLP is the same as the one used for Fe-He MLP1 and MLP2. Here we present the comparison of formation energies (E_f) of point defects such as vacancy (V), interstitial (H_{tet} , H_{oct}) and substitutional hydrogen (H_{sub}) using MLP and DFT. Furthermore, the migration of interstitial hydrogen between two tetrahedral positions and binding energies of interstitial hydrogen with monovacancy hydrogen bubbles, $H_{n-1}V$, are also presented.

Figure 4 presents the comparison of binding energies of hydrogen with $H_{n-1}V$ bubble, calculated using MLP and DFT. The binding energies are calculated using: Binding Energy = $E[H_{n-1}V] + E[H_{tet}] - E[H_nV] - E[\text{pristine}]$. $E[H_{n-1}V]$ and $E[H_nV]$ are the total energies of $H_{n-1}V$ and H_nV monovacancy bubbles containing $n - 1$ and n number of hydrogen atoms, respectively. $E[H_{tet}]$ and $E[\text{pristine}]$ are the total energies of H in a tetrahedral position (which is the ground state of H in BCC-Fe) and pristine supercell of BCC-Fe, respectively. Here we find that DFT predicts positive binding energies for $n = 1$ to 5 and negative binding energy for $n = 7$. This data is in agreement with binding energies from literature, calculated using DFT and interatomic potentials.⁸ For $n = 6$, DFT calculations in our work predict a small but positive binding energy, 4 meV – indicating thermodynamic stability at 0 K – which is 23 meV greater than DFT value from Ramasubramaniam et al.⁸ (-19 meV) a negative value. This discrepancy can be explained by the smaller 3x3x3 supercell used by Ramasubramaniam et al.⁸ The binding energies calculated using MLP are in good agreement with DFT values, with maximum error of 66 meV (25%), at $n = 4$.

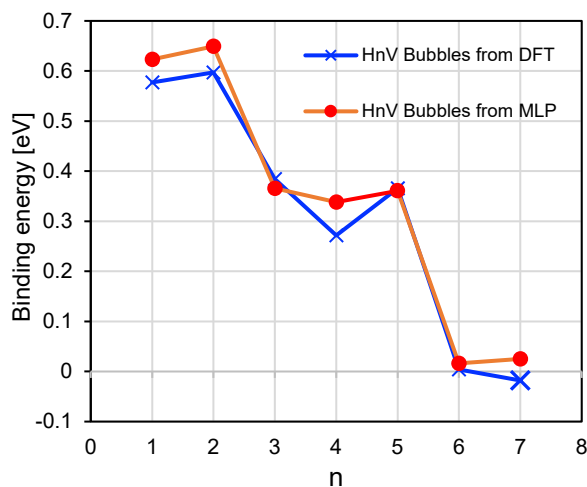
**Figure 4.** Binding energies of interstitial H with $H_{n-1}V$ bubble to form H_nV bubble, calculated using DFT and MLP.

Figure 5 presents the comparison between the migration barrier of interstitial hydrogen between two adjacent tetrahedral positions, calculated using DFT and MLP. Nudged elastic band (NEB) method is used

to calculate the migration barriers. We find that the migration barrier calculated by MLP is in good agreement between DFT, with error=1 meV (1.4%).

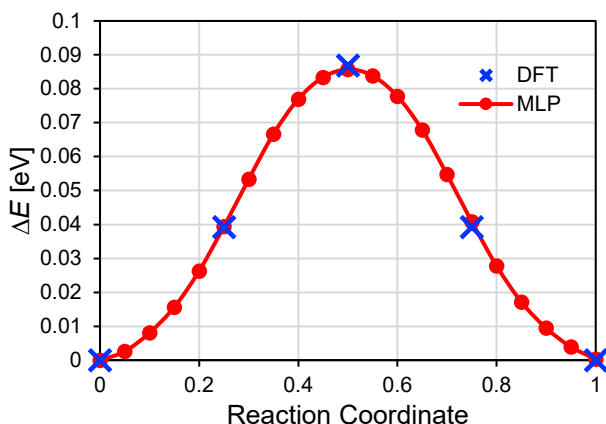


Figure 5. The migration energy of H between adjacent tetrahedral positions in BCC-Fe calculated DFT and MLP.

Table 4. Formation energy of a vacancy or H defect in bcc Fe, migration energy of H, and binding energy of H with a VH_{n-1} bubble

	MLP [eV]	DFT [eV]	Error [eV]
$E_f[V]$	2.504	2.150	0.354
$E_f[H_{tet}]$	0.441	0.223	0.218
$E_f[H_{oct}]$	0.565	0.352	0.213
$E_f[H_{sub}]$	-0.507	-0.354	-0.154
$E_m[H_{tet}]$	0.086	0.087	0.001
$E_b[n = 1]$	0.623	0.577	0.046
$E_b[n = 2]$	0.649	0.597	0.052
$E_b[n = 3]$	0.365	0.384	-0.019
$E_b[n = 4]$	0.338	0.272	0.067
$E_b[n = 5]$	0.361	0.366	-0.005
$E_b[n = 6]$	0.016	0.004	0.012
$E_b[n = 7]$	0.025	-0.018	0.043

Table 4 presents the comparison formation energies of vacancy, $E_f[V]$, tetrahedral hydrogen, $E_f[H_{tet}]$, octahedral hydrogen, $E_f[H_{oct}]$, substitutional hydrogen, $E_f[H_{sub}]$, migration barrier between two adjacent tetrahedral positions, $E_m[H_{oct}]$, and binding energies of H with $H_{n-1}V$ bubbles for $n = 1$ to $n = 7$, calculated using DFT and MLP. Even though the formation energies are predicted with large errors (>200 meV) compared to DFT, the binding energies of H with monovacancy bubbles are calculated with excellent accuracy (error < 66 meV). Furthermore, the migration barrier of interstitial H migration between two adjacent tetrahedral positions is also predicted accurately by MLP with error = 1 meV.

Results

Future research will continue the MD simulations using the Caro potential to obtain additional data points of bubble pressures (data at 900 K and for 2-3 additional bubble sizes) to complete the EOS. Results will be submitted for publication.

Acknowledgements

This research was supported by the U.S. Department of Energy (US DOE), Office of Science, Office of Fusion Energy Sciences, through Contract No. AT2030110-13784 and was performed at the Pacific Northwest National Laboratory, which is operated by Battelle for the US DOE under Contract No. DE-AC05-76RL0-1830.

References

- [1.] C. K. Pitike, W. Setyawan, Accurate Fe–He Machine Learning Potential for Studying He Effects in BCC-Fe, *Journal of Nuclear Materials* 574 (2023) 154183.
- [2.] A. Caro, J. Hetherly, A. Stukowski, et al., Properties of Helium Bubbles in Fe and FeCr Alloys, *Journal of Nuclear Materials* 418 (2011) 261.
- [3.] G. J. Ackland, M. I. Mendeleev, D. J. Srolovitz, et al., Development of an Interatomic Potential for Phosphorus Impurities in Iron, *Philosophical Magazine* 16 (2004) S2629.
- [4.] D. E. Beck, A New Interatomic Potential Function for Helium, *Molecular Physics* 14 (1968) 311.
- [5.] N. Juslin, K. Nordlund, Pair Potential for Fe–He, *Journal of Nuclear Materials* 382 (2008) 143.
- [6.] W. Setyawan, D. Dasgupta, S. Blondel, et al., Equation of State for He Bubbles in W and Model of He Bubble Growth and Bursting near W{100} Surfaces Derived from Molecular Dynamics Simulations, *Scientific Reports* 13 (2023) 9601.
- [7.] A. Y. Cengel, M. A. Boles, M. Kanoğlu, *Thermodynamics: An Engineering Approach*; McGraw-hill New York, 2011; Vol. 5.
- [8.] A. Ramasubramaniam, M. Itakura, A. E. Carter, Erratum: Interatomic Potentials for Hydrogen in α -Iron Based on Density Functional Theory, *Physical Review B* 81 (2010) 099902.

10. FUSION SYSTEM DESIGN

No contributions this reporting period.

11. IRRADIATION & TESTING METHODS, EXPERIMENTS AND SCHEDULES

11.1 SPECIMEN SIZE AND GEOMETRY EFFECTS ON THE MASTER CURVE FRACTURE TOUGHNESS MEASUREMENT OF EUROFER97 AND F82H STEELS—X. Chen, M. Sokolov, Y. Katoh (Oak Ridge National Laboratory), John Echols (U.S. Department of Energy)

OBJECTIVE

Under the International Atomic Energy Agency (IAEA) Coordinated Research Projects (CRP) framework, this work aims for evaluating specimen size and geometry effects on Master Curve fracture toughness measurement of fusion structural materials. The ultimate goal is to establish a Master Curve testing and analysis guideline based on interlaboratory round-robin results and best practices.

SUMMARY

Under the auspices of IAEA, a CRP entitled “Towards the Standardization of Small Specimen Test Techniques for Fusion Applications - Phase II” started in 2022. This CRP builds upon the work initiated in the previous CRP F1.30.17, titled “Towards the Standardization of Small Specimen Test Techniques for Fusion Applications.” In this second phase, the focus will shift to evaluating the applicability of the guidelines and methodologies developed so far under high-temperature conditions and within hot cell environments. Additionally, this phase aims to address remaining gaps in the output of CRP F1.30.17. The overall objective of the project is to provide the bases for the standardization of Small Specimen Test Techniques (SSTT) specimens making them available for their use in fusion material irradiation facilities. Fusion structural materials, i.e., reduced activation ferritic/martensitic (RAFM) steels such as EUROFER97 and F82H, were used for testing. In addition, the project would generate additional mechanical property data of RAFM steels tested by SSTT.

PROJECT AND STATUS

For the fracture toughness task of the CRP, three testing methods—including Master Curve, local approach, and ductile approach—were evaluated. This study focused on the Master Curve method based on the ASTM standard E1921-21a “Standard Test Method for Determination of Reference Temperature, T_0 , for Ferritic Steels in the Transition Range” [1] and commonly agreed best practices from researchers at Oak Ridge National Laboratory (ORNL), the Center for Energy, Environmental and Technological Research (CIEMAT), and United Kingdom Atomic Energy Authority (UKAEA) [2].

Detailed descriptions of the test materials, testing matrix, specimen types and geometries, experimental setup, and earlier results have been reported in the previous Fusion Semiannual reports [3, 4]. This report summarizes the latest findings from UKAEA on their miniCT-DONES specimens (4.6mm thickness miniCT). As shown in Figure 1, the UKAEA miniCT-DONES results are compared with the ORNL 4mm miniCT results due to their similarity in size and geometry. For both EUROFER97 batch-3 and F82H-BA12, two specimen types exhibited similar Master Curve results and the difference in the Master Curve index temperature, T_0 , was only 4°C and zero for EUROFER97 and F82H, respectively. For both specimen types, the ASTM E1921 Master Curve and its tolerance bounds show an excellent representation of transition fracture toughness for EUROFER97 batch-3 and F82H-BA12. Specifically, the Master Curve predicts the median fracture toughness of both materials at the test temperature, and most valid tests are bound by 2% and 98% tolerance bounds.

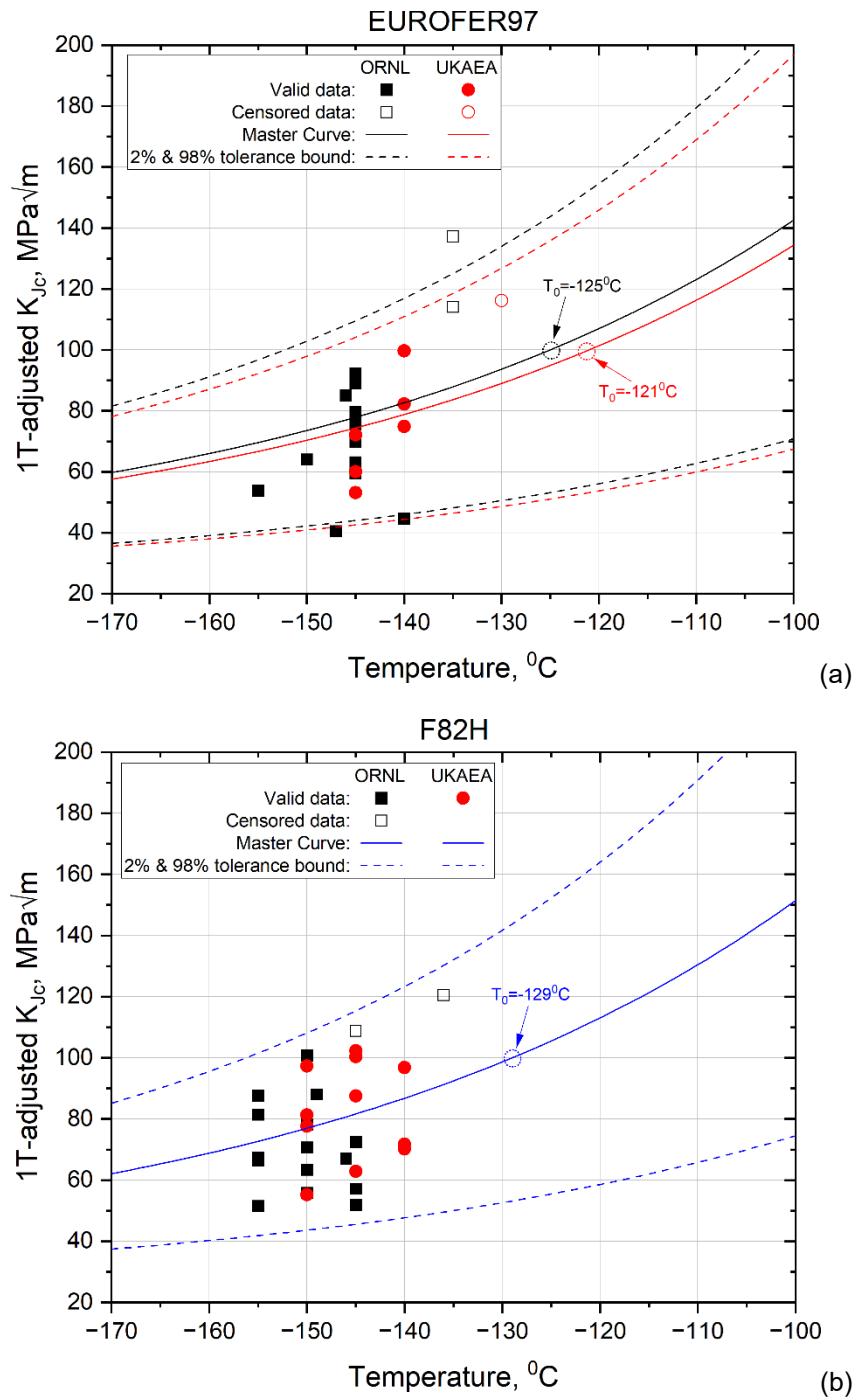


Figure 1. Comparison of Master Curve results between ORNL 4mm miniCT and UKAEA miniCT-DONES for (a) EUROFER97 batch-3 and (b) F82H-BA12.

Figure 2 compares the Master Curve index temperature, T_0 , obtained from different types of specimens for EUROFER9 and F82H. Using the ORNL 0.5T CT results as a baseline, except for the 1.65 mm bend bar specimens, T_0 from all other specimen types were within two standard deviations from T_0 obtained from the ORNL 0.5T CT indicating no apparent size effect of those specimens for T_0 determination. However, T_0 from 1.65 mm bend bar specimens was much higher than that from 0.5T CT demonstrating an apparent

size effect. More study is needed to understand the size effect of 1.65 mm bend bar specimens. Figure 2 also shows that the differences in T_0 between the ORNL 0.5T CT and the CIEMAT counterpart and ORNL 4 mm miniCT and UKAEA miniCT-DONES were within two standard deviations, meaning statistically insignificant difference between those laboratories. Therefore, results from three independent laboratories were comparable to each other. In addition, for the same type of specimens tested, EUROFER97 batch-3 and F82H-BA12 exhibited a similar trend in T_0 , i.e., slightly lower T_0 in F82H than EUROFER97.

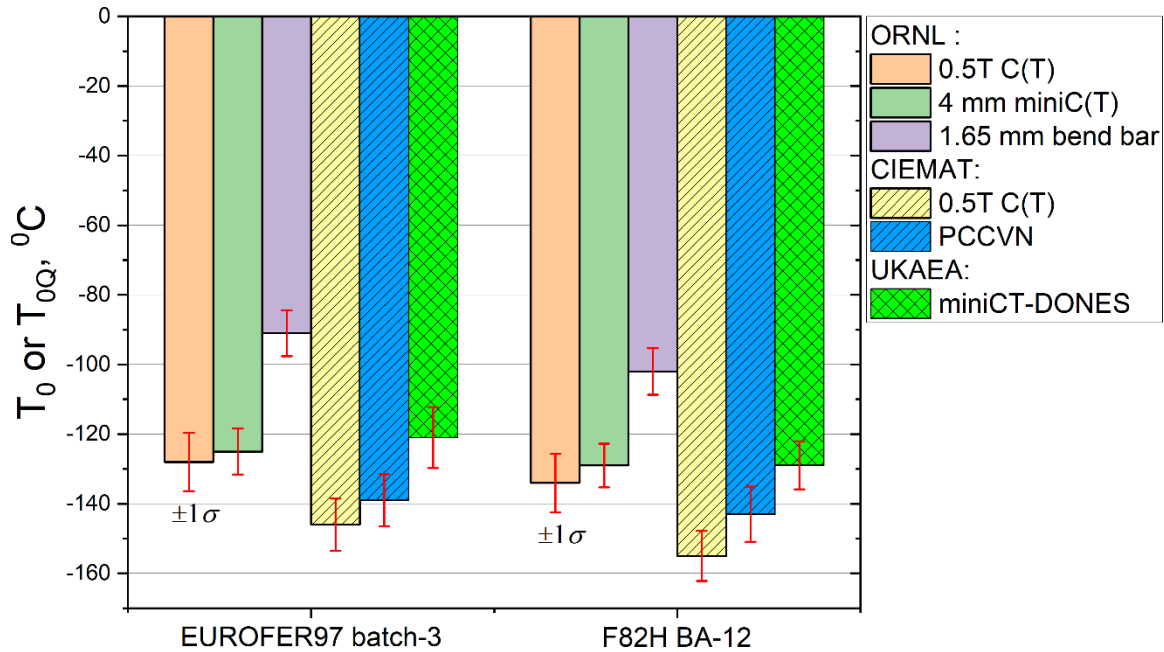


Figure 2. Comparison of the Master Curve index temperature, T_0 , obtained from different types of specimens for EUROFER97 batch-3 and F82H-BA12. The error bars correspond to one standard deviation.

References

- [1] ASTM E1921-21a, Standard Test Method for Determination of Reference Temperature, T_0 , for Ferritic Steels in the Transition Range, ASTM International, West Conshohocken, PA, 2021, www.astm.org.
- [2] X. Chen et al., "Guidelines for IAEA Small Specimen Test Techniques Master Curve Fracture Toughness Testing", ORNL/LTR-2020/27, July.
- [3] X. Chen, J. Reed, E. Manneschildt, M. Sokolov, "IAEA SMALL SPECIMEN TEST TECHNIQUE DEVELOPMENT: MASTER CURVE FRACTURE TOUGHNESS TESTING UPDATE AT ORNL," Fusion Materials Semiannual Report 6/30/2021 DOE/ER-313/70 (2017) 200.
- [4] X. Chen, M. A. Sokolov, Y. Katoh, M. Serrano, R. Hernández, S. Gonzalez De Vicente, "SPECIMEN SIZE AND GEOMETRY EFFECTS ON THE MASTER CURVE FRACTURE TOUGHNESS MEASUREMENT OF EUROFER97 AND F82H STEELS," Fusion Materials Semiannual Report 6/30/2023 DOE/ER-313/73 (2023) 1.

11.2 IRRADIATION OF JK2LB ALLOYS FOR ADDITIVE MANUFACTURING OF FUSION COMPONENTS FOR THE INFUSE PROJECT WITH TYPE ONE ENERGY—N. Russell, X. Chen, W. Zhong, Y. Yang (Oak Ridge National Laboratory), B. Goh (Type One Energy), L. Chen (University of Wisconsin, Madison)

OBJECTIVE

The objective of this task is characterization of AM JK2LB alloys for fusion applications by performing neutron irradiation in the High Flux Isotope Reactor (HFIR) and mechanical testing in the Irradiated Material Examination and Testing (IMET) Facility. The JK2LB is a Japanese high manganese austenitic stainless steel designed for fusion components. Specimens were fabricated using different AM techniques for irradiation in two different HFIR irradiation capsules. Additionally, Oak Ridge National Laboratory (ORNL) is including an advanced ferritic-martensitic steel (CNA-HT7) into the capsules. The first capsule uses the well-established GENTEN design with an irradiation target temperature of 300°C. The second capsule uses a perforated Al housing to allow the HFIR primary coolant to contact directly with the specimen, cooling the specimens to an estimated 80°C. Dose accumulation for the specimens is expected at about 1.5 dpa after one HFIR cycle.

SUMMARY

The 54 total specimens will be allocated with mostly the JK2LB materials (45) and CNA-HT7 (9) among the two capsules. The total allocations are described in Table 1.

Table 1. Specimen allocations

Temperature Class of SS-J3 Specimens	Total Specimens Available	ORNL CNA Specimens	Type One Energy AM JK2LB Specimens
80 Celsius	30	3	27
300 Celsius	24	6	18
TOTAL	54	9	45

Of the JK2LB material there are several AM processes being compared: Laser Powder Bed Fusion (LPBF), Laser Directed Energy Deposition (LDED), Arc Directed Energy Deposition (ARC DED). Of those AM processes, there are alternating cases containing 3.3 wt% Y₂O₃. The specimens included in the capsules are further described in Table 2.

Table 2. Specimen materials and identifiers

Specimen Material / AM Process	Perforated Capsule (80°C)	Sealed Capsule (300°C)
ORNL CNA	CR7a-c (3)	CR7d, CR7f-h, CR7j-k (6)
JK2LB	JCT1, JCT2, JCT4-6 (5)	JCT3, JCT7, JCT8 (3)
JK2LB AM LPBF	JCP1-JCP5 (5)	JCP6-JCP8 (3)
JK2LB – Y ₂ O ₃ AM LPBF	JYP1-JYP5 (5)	JYP6-JYP8 (3)
JK2LB AM LDED	JCL1-JCL5 (5)	JCL6-JCL8 (3)
JK2LB – Y ₂ O ₃ AM LDED	JYL2-JYL5, JYL9 (5)	JYL1, JYL6-JYL8 (4)
JK2LB AM ARC DED	JCA1 (1)	JCA2 (1)
JK2LB – Y ₂ O ₃ AM ARC DED	JYA1 (1)	JYA2 (1)

For the 300°C capsule, identified as T1E-1, the temperature within the capsule is controlled by optimizing the specimen holder outer diameter (OD), holder material, and fill gas to create an insulating gas gap between the hot inner holder assembly and the cold capsule housing in direct contact with HFIR coolant.

Much care and consideration were taken to apply the existing GENTEN design. This design developed a surface response model that allows the user to quickly and accurately determine a combination of holder OD, holder material, and fill gas to achieve an average specimen goal temperature. The capsule design can be seen below in Figure 1. From the surface response for the T1E-1 capsules, Al holders with nominally 9.26 mm OD were determined. The capsule was also to be filled with He gas and irradiated in axial position 4 of the HFIR flux trap facility.

However, the thermal conductivity of JK2LB is known to be about a third of FM steels (11 W/m-K vs. ~33 W/m-K). Using the conduction equation, the GENTEN surface response can be adjusted to account for the thermal conductivity change. It was determined that 9.30 mm OD holders should be used with the JK2LB specimens. The T1E-1 capsule parts are shown in Figure 2 with the final capsule prior to HFIR insertion shown in Figure 3.

The perforated capsule housing consists of 72 holes allowing the primary coolant from HFIR to directly cool the experiment. A set of spacers were added within the capsule to give structure to the specimen stacks but to also allow the HFIR coolant to partially redistribute between the specimen stacks. The capsule design can be seen below in Figure 4. The T1E-2 capsule parts are shown in Figure 5 with the final capsule prior to HFIR insertion shown in Figure 6.

PROGRESS AND STATUS

The 300°C capsule, T1E-1, was irradiated in HFIR position F7-4 for cycle 508. Immediately following irradiation, the capsule was moved to storage and replaced with the perforated capsule, T1E-2, for irradiation in cycle 509. Cycle 508 operated from July 23 to August 17, 2024. Cycle 509 is scheduled to operate from September 3 to September 27, 2024. After the completion for cycle 509, the two capsules will be shipped to the IMET facility to begin disassembly.

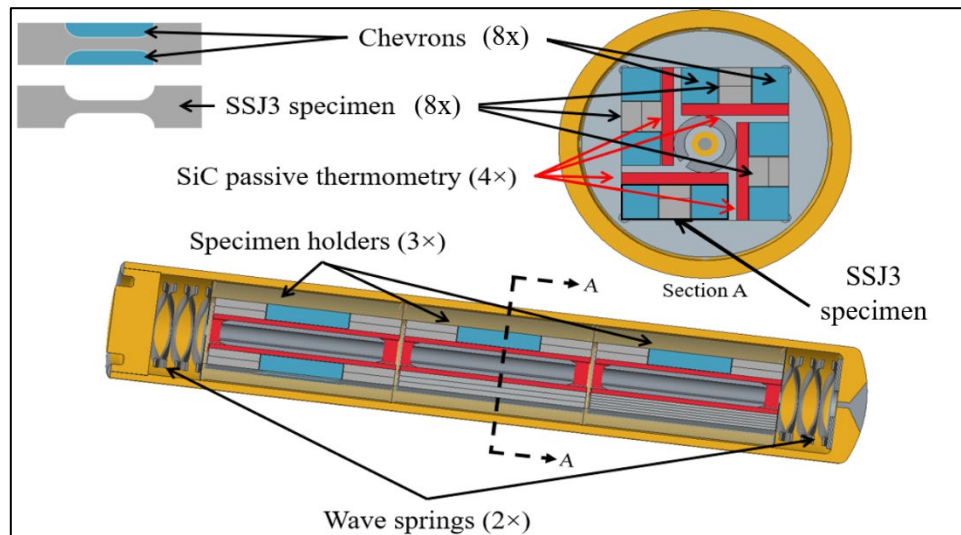


Figure 1. The GENTEN irradiation capsule design.



Figure 2. The T1E-1 parts laid on lint free towel prior to assembly.



Figure 3. Final T1E-1 capsule prior to HFIR insertion.

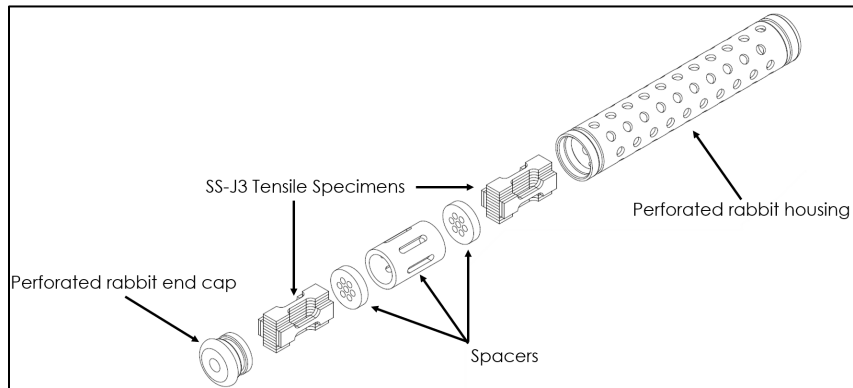


Figure 4. Perforated capsule design.



Figure 5. The T1E-2 parts laid on lint free towel prior to assembly.



Figure 6. Final T1E-2 capsule prior to HFIR insertion.